

ISSN 2189-6909

October 2017

# LASTI Annual Report

Laboratory of Advanced Science and Technology for Industry  
University of Hyogo

Vol.18 (2016)



## PREFACE

This annual report reviews the research activities of the Laboratory of Advanced Science and Technology for Industry (LASTI) in the academic year of 2016 which is from April 2016 to March 2017) including research activities using NewSUBARU light source at the site of SPring-8 and other research activities of the micro and nanoscale are carried out energetically in the building of Center for Advanced Science and Technology (CAST) II.

The annual report describes that topics of the NewSUBARU research activities of this year including 1) the research and development of gamma ray application at BL2 beamline, 2) the next generation lithography by extreme ultraviolet (EUV) lithography at BL3, BL9B, BL9C, and BL10 beamlines, 3) Lithographie, Galvanoformung, and Abformung (LIGA) process technology at BL2 and BL11 beamlines, 4) the chemical analysis using soft X-ray absorption fine structure at (BL5, BL9A, and BL7 beamlines and soft X-ray emission spectroscopy at BL5 and BL9A beamlines at soft x-ray energy region, and 5) the nanoimprint lithographic technology at CAST.

Most of our research activities are being conducted in collaboration research works with industries, government research institutes, and other universities.

We will continue to respond to the community's demand by offering new science and technology.



Takeo Watanabe

A handwritten signature in black ink that reads "Takeo Watanabe". The signature is written in a cursive style with a long, sweeping underline.

Director of Laboratory of  
Advanced Science and  
Technology for Industry,  
University of Hyogo



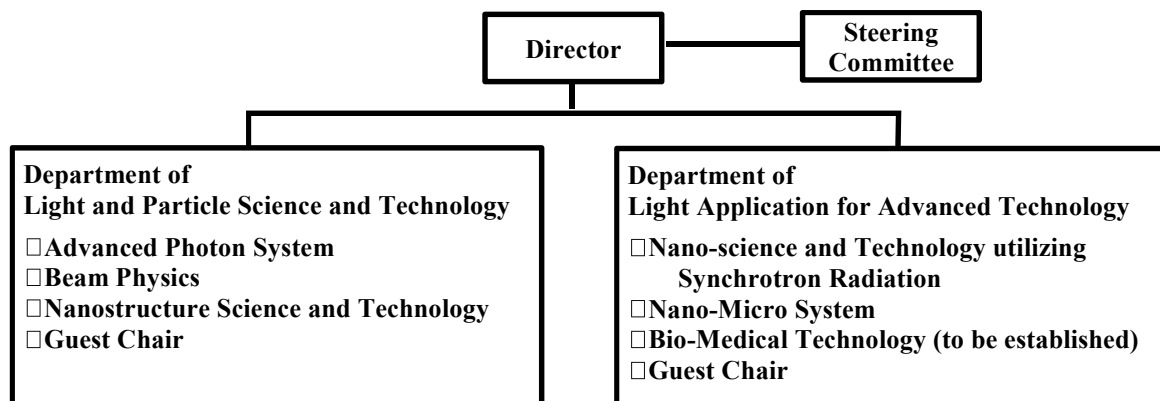


Staff of LASTI  
(In front of Advanced Research Building)



# The Organization of Laboratory of Advanced Science and Technology for Industry University of Hyogo

## The organization



## Staff (FY 2015)

### Research and faculty staff

WATANABE Takeo, Professor , Director  
 MIYAMOTO Shuji, Professor  
 KANDA Kazuhiro, Professor  
 UTSUMI Yuichi, Professor  
 NIIBE Masahito, Associate Professor  
 SHOJI Yoshihiko, Associate Professor  
 HARUYAMA Yuichi, Associate Professor  
 YAMAGUCHI Akinobu, Associate Professor  
 AMANO Sho, Research Associate  
 HASHIMOTO Satoshi, Research Associate  
 HARADA Tetsuo, Research Associate  
 OKADA Makoto, Research Associate

### Specially appointed staff

MOCHIZUKI Takayasu, Professor  
 KINOSHITA Hiroo, Professor  
 MATSUI Shinji, Professor  
 KUDOU Hiroto, Professor  
 TERANISHI Nobukazu, Professor  
 NAGATA Yutaka, Assistant Professor

### Administrative staff

HAMAGAMI Akiyuki, General Manager  
 KOBORI Kazuyuki, Manager  
 KURODA Takashi, Chief  
 KAMIYA Miki, CAST  
 KANATANI Naoko, NewSUBARU  
 YAMAMOTO Keiko, CAST  
 YOKOYAMA Yuka, CAST  
 YANO Ayumi, CAST  
 FUJIMAKI Hisae, CAST  
 YAMADA Miki, CAST  
 KUSUMOTO Kumi, CAST  
 MORIGUCHI Miyuki, Harima Forum of  
 Science and Technology for 21st Century

### Coordinator

FUKADA Noboru, NewSUBARU  
 ISHIKAWA Kazuko, NewSUBARU  
 FUKUOKA Takao, CAST

### Guest staff

OHKUMA Haruo, Professor  
 ASANO Yoshihiro, Professor  
 FUKUSHIMA Sei, Professor  
 HORIBE Hideo, Professor  
 BAN Hiroshi, Professor

## Contact address

### Advanced Research Building

3-1-2 Kouto, Kamigori-cho, Ako-gun, Hyogo, 678-1205 JAPAN.  
 T:+81-791-58-0249 F:+81-791-58-0242

### NewSUBARU Synchrotron Radiation Facility

1-1-2 Kouto, Kamigori-cho, Ako-gun, Hyogo, 678-1205 JAPAN.  
 T:+81-791-58-2503 F:+81-791-58-2504

**Web URL** <http://www.lasti.u-hyogo.ac.jp/>, <http://www.lasti.u-hyogo.ac.jp/NS/>

**e-Mail** [lasti@lasti.u-hyogo.ac.jp](mailto:lasti@lasti.u-hyogo.ac.jp)

**Access** <http://www.lasti.u-hyogo.ac.jp/NS-en/access/>

# CONTENTS

## PREFACE

## ORGANIZATION of LASTI

### Part 1. Current Status of NewSUBARU and Other Light Source

<b>NewSUBARU Storage Ring</b> .....	01
Shuji Miyamoto ( <i>LASTI/University of Hyogo</i> )	
<b>NewSUBARU Beamlines</b> .....	04
Masahito Niibe ( <i>LASTI/University of Hyogo</i> )	
<b>Laser Compton scattering gamma ray generated using Yb fiber laser and Er fiber laser in NewSUBARU BL01</b> .....	11
Kento Sugita, Yuusuke Morimoto, Satoshi Hashimoto, Sho Amano, Shuji Miyamoto ( <i>LASTI, University of Hyogo</i> )	
<b>Development of fast positron measurement apparatus for defects study in bulk materials</b> .....	13
F. Hori <sup>1</sup> , Y. Ueno <sup>1</sup> , Y. Sumikura <sup>1</sup> , A. Iwase <sup>1</sup> , K. Sugita <sup>2</sup> , Y. Takemoto <sup>2</sup> , S. Miyamoto <sup>2</sup> , M. Terasawa <sup>2</sup> ( <sup>1</sup> Graduate School of Eng., Osaka Pref. Univ., <sup>2</sup> <i>LASTI, University of Hyogo</i> )	
<b>Mechanical stability of the main axis of the double multilayer monochromator in BL07A</b> .....	15
Masato Okui <sup>1,2</sup> , Naoki Yato <sup>1</sup> , Ren Konno <sup>1</sup> , Akinobu Watanabe <sup>1</sup> , Osamu Shiga <sup>1</sup> , Norio Murayama <sup>1</sup> , Sei Fukushima <sup>2, 3</sup> and Kazuhiro Kanda <sup>2, 3</sup> , ( <sup>1</sup> <i>Kohzu Precision Co., Ltd.</i> , <sup>2</sup> <i>LASTI, University of Hyogo</i> , <sup>3</sup> <i>Kobe Material Testing Laboratory Co., Ltd.</i> )	
<b>Energy Calibration and Spike Noise Reduction for Ultra-soft X-ray Fluorescence Spectrum on BL07A</b> .....	17
Sei Fukushima <sup>1,2</sup> , Hiroki Takamatsu <sup>1</sup> , Shotaro Tanaka <sup>1</sup> , Kazuhiro Kanda <sup>1</sup> ( <sup>1</sup> <i>LASTI, University of Hyogo</i> , <sup>2</sup> <i>National Institute for Materials Science</i> )	
<b>Development of a transfer vessel system for XAS analysis of anaerobic samples in BL10</b> .....	20
Yasuji Muramatsu, Keigo Yoshida ( <i>Graduate School of Engineering, University of Hyogo</i> )	
<b>Large area patterning using a new deep x-ray lithography system (BL11)</b> .....	22
Masaya Takeuchi, Akinobu Yamaguchi, Yuichi Utsumi ( <i>LAST, University of Hyogo</i> )	
<b>Part 2. Research Activities</b>	
<b>Upgrade plan toward the higher-brightness radiation source, NewSUBARU-2.0</b> .....	27
Satoshi Hashimoto ( <i>LAST, University of Hyogo</i> )	
<b>Possibility of High-power EUV light by PEHG scheme at NewSUBARU-2.0</b> .....	31

<b>Test of a gamma-ray diamond detector</b> .....	33
A. Martens <sup>1</sup> , T. Williams <sup>1</sup> , S. Amano <sup>3</sup> , K. Cassou <sup>1</sup> , K. Dupraz <sup>1</sup> , E. Griesmayer <sup>2</sup> , S. Hashimoto <sup>3</sup> , P. Kavargin <sup>2</sup> , S. Miyamoto <sup>3</sup> , C. Ndiaye, A. Takemoto <sup>3</sup> , M. Yamaguchi <sup>3</sup> , F. Zomer <sup>1</sup> ( <sup>1</sup> <i>LAL, Univ.</i> , <sup>2</sup> <i>Vienna University of Technology</i> , <sup>3</sup> <i>LASTI/ Univ. Hyogo</i> )	
<b>Test of Gamma-ray detector (LaBr<sub>3</sub>)</b> .....	35
F. Camera <sup>1,2</sup> , G. Gosta <sup>1,2</sup> , N. Blasi <sup>2</sup> , B. Million <sup>2</sup> , A. Giaz <sup>2</sup> , O. Wieland <sup>2</sup> , F. M. Rossi <sup>1</sup> , H. Utsunomiya <sup>3</sup> , T. Ari-izumi <sup>3</sup> , D. Takenaka <sup>3</sup> , D. Filipescu <sup>4</sup> , I. Gheorghe <sup>4,5</sup> ( <sup>1</sup> <i>Univ. Milano</i> , <sup>2</sup> <i>INFN Section of Milano</i> , <sup>3</sup> <i>Konan Univ.</i> <sup>4</sup> <i>IFIN-HH</i> , <sup>5</sup> <i>Univ. Bucharest</i> )	
<b>Improvement of Performance for XAFS Measurements in BL05A</b> .....	37
T. Hasegawa <sup>1,2,3</sup> , S. Fukushima <sup>2,3</sup> and K. Kanda <sup>3</sup> ( <sup>1</sup> <i>Synchrotron Analysis L.L.C.</i> , <sup>2</sup> <i>Kobe Material Testing Laboratory Co., Ltd.</i> , <sup>3</sup> <i>LASTI/Univ. Hyogo</i> )	
<b>Erosion Process of Fluorinated Diamond-like Carbon Films by Exposure to Soft X-rays</b> .....	39
Kazuhiro Kanda <sup>1</sup> , Hiroki Takamatsu <sup>1</sup> , Eri Miura-Fujiwara <sup>2</sup> , Hiroki Akasaka <sup>3</sup> , Akihiro Saiga <sup>4</sup> , Koji Tamada <sup>4</sup> ( <sup>1</sup> <i>LASTI/Univ. Hyogo</i> , <sup>2</sup> <i>Eng./Univ. Hyogo</i> , <sup>3</sup> <i>Tokyo Institute of Technology</i> , <sup>4</sup> <i>National Institute of Technology</i> )	
<b>Surface Modifications in Silica-Based Films by Undulator Radiation with a Multilayer Spectrometer</b> .....	43
K. Moriwaki <sup>1</sup> , T.Miyamoto <sup>1</sup> , and K.Kanda <sup>2</sup> ( <sup>1</sup> <i>Kobe Univ.</i> , <sup>2</sup> <i>LASTI/Univ. Hyogo</i> )	
<b>Molecular Orientation of Imprinted Photoreactive Liquid Crystalline Polymer Measured by Near-edge X-ray Absorption Fine Structure</b> .....	46
Y. Haruyama <sup>1</sup> , M. Okada <sup>1</sup> , E. Nishioka <sup>2</sup> , M. Kondo <sup>2</sup> , N. Kawatsuki <sup>2</sup> , and S. Matsui <sup>1</sup> ( <sup>1</sup> <i>LASTI/Univ. Hyogo</i> , <sup>2</sup> <i>Eng./Univ. Hyogo</i> )	
<b>Development of Fine-grained 316L Steel with 1.0-2.0 Mass% TiC for Nuclear Reactor Materials</b> .....	48
Mititaka Terasawa <sup>1</sup> , Hiroaki Kurishita <sup>2</sup> , Tatsuaki Sakamoto <sup>3</sup> , Masahito Niibe <sup>1</sup> , Heishichiro Takahashi <sup>4</sup> , Satoru Nishikawa <sup>5</sup> , Atsusi Yamamoto <sup>6</sup> , Michiru Yamashita <sup>7</sup> , Tohru Mitamura <sup>1</sup> , Tohru Yamasaki <sup>6</sup> and Masayoshi Kawai <sup>8</sup> ( <sup>1</sup> <i>LASTI/Univ. Hyogo</i> , <sup>2</sup> <i>Tohoku Univ.</i> , <sup>3</sup> <i>Ehime Univ.</i> , <sup>4</sup> <i>Hokkaido Univ.</i> , <sup>5</sup> <i>Japan Power Engineering and Inspecion Corporation</i> , <sup>6</sup> <i>Eng./Univ. Hyogo</i> , <sup>7</sup> <i>Hyogo Prefectural Institute of Technology</i> , <sup>8</sup> <i>High Energy Accelerator Research Organization</i> )	
<b>Surface Structure Analysis of AlGaN Thin Films Damaged by Oxygen and Nitrogen Plasmas</b> .....	50
Ryo Tanaka <sup>1</sup> , Masahito Niibe <sup>1</sup> , Retsuo Kawakami <sup>2</sup> , Yoshitaka Nakano <sup>3</sup> , Takashi Mukai <sup>4</sup> ( <sup>1</sup> <i>LASTI/Univ. Hyogo</i> , <sup>2</sup> <i>Tokushima Univ.</i> , <sup>3</sup> <i>Chubu Univ.</i> , <sup>4</sup> <i>Nichia Corporation</i> )	
<b>Development of the Transmittance Measurement for EUV Resist by Direct-Resist Coating on a</b>	

<b>Photodiode</b> .....	53
Daiki Mamezaki, Masanori Watanabe, Tetsuo Harada, and Takeo Watanabe ( <i>LASTI/Univ. Hyogo</i> )	
<b>EUVL Research Activity at Center for EUV Lithography</b> .....	58
Takeo Watanabe and Tetsuo Harada ( <i>LASTI/Univ. Hyogo</i> )	
<b>Oxidation of Mechanically Ground h-BN</b> .....	66
Yoshida Keigo and Yasuji Muramatsu ( <i>Eng./Univ. Hyogo</i> )	
<b>XANES of Fullerenes (C60, C70) Simulated by CASTEP</b> .....	69
Yuma Hirai and Yasuji Muramatsu ( <i>Eng./Univ. Hyogo</i> )	
<b>Soft X-ray Analyses of Detonation Nanodiamonds to Investigate Surface sp<sup>2</sup> Carbon for the Dispersibility Improvement</b> .....	72
Masahiro Nishikawa <sup>1</sup> , Ming Liu <sup>1</sup> , and Yasuji Muramatsu <sup>2</sup> ( <sup>1</sup> <i>Daicel Corporation</i> , <sup>2</sup> <i>Eng./Univ. Hyogo</i> )	
<b>Deterioration and Depth-Profile Analyses of Organic Thin Film</b> .....	74
Shogo Suehiro <sup>1</sup> , Eiji Takahashi <sup>1</sup> , Yousuke Azuma <sup>1</sup> , Yasuko Mitsushita <sup>1</sup> , Yasuji Muramatsu <sup>2</sup> , and Yoshiyuki Suzuri <sup>3</sup> ( <sup>1</sup> <i>Sumika Chemical Analysis Service, Ltd.</i> , <sup>2</sup> <i>Eng./Univ. Hyogo</i> , <sup>3</sup> <i>Yamagata Univ.</i> )	
<b>Analysis of Adsorbed Monolayer Molecules Formed by Oil Additives on Frictional Surfaces by NEXAFS</b> .....	76
Naoko Takahashi <sup>1</sup> , Masaru Okuyama <sup>1</sup> , Noritake Isomura <sup>1</sup> , Mamoru Tohyama <sup>1</sup> , Yasuji Kimoto <sup>1</sup> , Toshihide Ohmori <sup>1</sup> , Yasuji Muramatsu <sup>2</sup> , Keita Nanbu <sup>2</sup> , Takahito Ouchi <sup>2</sup> ( <sup>1</sup> <i>Toyota Central R&amp;D Labs., Inc.</i> , <sup>2</sup> <i>Eng./Univ. Hyogo</i> )	
<b>Miniature Micro-Powder Feeder Driven by Surface Acoustic Wave</b> .....	78
Tsunemasa Saiki <sup>1,2</sup> , Akinobu Yamaguchi <sup>2</sup> , Michitaka Suzuki <sup>2</sup> , and Yuichi Utsumi <sup>2</sup> ( <sup>1</sup> <i>Hyogo Prefectural Institute of Technology</i> , <sup>2</sup> <i>University of Hyogo</i> )	
<b>C-, N-, O-XANES Analyses of Complex Suites of Organic Compounds Produced by Laboratory Simulations of Extraterrestrial Environments</b> .....	81
Yoko Kebukawa <sup>1</sup> , Shusuke Misawa <sup>1</sup> , Hitomi Abe <sup>1</sup> , Shingo Enomoto <sup>1</sup> , Yasuji Muramatsu <sup>2</sup> , Takahito Ouchi <sup>2</sup> , Sohta Hamanaka <sup>2</sup> , Hitoshi Fukuda <sup>3</sup> , Yoshiyuki Oguri <sup>3</sup> , Satoshi Yoshida <sup>4</sup> , Isao Yoda <sup>4</sup> , and Kensei Kobayashi <sup>1</sup> ( <sup>1</sup> <i>Yokohama National Univ.</i> , <sup>2</sup> <i>Eng./Univ. Hyogo</i> , <sup>3</sup> <i>Tokyo Institute of Technology</i> , <sup>4</sup> <i>National Institute for Quantum and Radiological Sciences and Technology</i> )	

## List of publications

<b>(1) Papers</b> .....	87
<b>(2) International meetings</b> .....	88
<b>(3) Academic degrees</b> .....	89



# **Part 1. Current Status of NewSUBARU and Other Light Source**



Staff of NewSUBARU

(In front of NewSUBARU Facility)



# NewSUBARU Storage Ring

Shuji Miyamoto, Satoshi Hashimoto, Yoshihiko Shoji  
LASTI, University of Hyogo

## Storage Ring Parameters

The machine parameters of the NewSUBARU storage ring are listed in Table I. The machine condition remains the same with last year during the beginning half of the fiscal year 2016. In the late half of FY2016, the NewSUBARU operated without the 1.5 GeV high energy mode, because of a failure of auxiliary power supply for the inverse bending magnet. The failed power supply was completed update by the end of FY2016, NewSUBARU has returned back to the normal operation from the beginning of the FY 2017.

Table I Main parameters of the NewSUBARU storage ring.

Circumference	118.73 m		
Lattice	DBA+Inv. bending		
Number of bending mag.	12		
Radius of curvature	3.217m		
RF frequency	499.955 MHz		
Betatron tunes	H: 6.30, V:2.23		
Bunch length (sigma)	33ps (normal operation)		
Harmonic number	198		
Radiation loss per turn	33.4 keV (@1GeV)		
Electron energy	1.0GeV	1.5GeV	
	Mode	TopUp	Decay
Natural energy spread	0.047%	0.072%	
Natural emittance	50 nm	112 nm	
Storage current	300 mA	350mA	

## Operation Status

The ring has two user-time operation modes, 1.0 GeV top-up operation mode and 1.5 GeV current decay operation mode. The basic operation time is 9:00 - 21:00 of weekdays. Monday is used for machine R&D, Tuesday is for 1.5 GeV user time, Wednesday and Thursday are for 1.0 GeV top-up

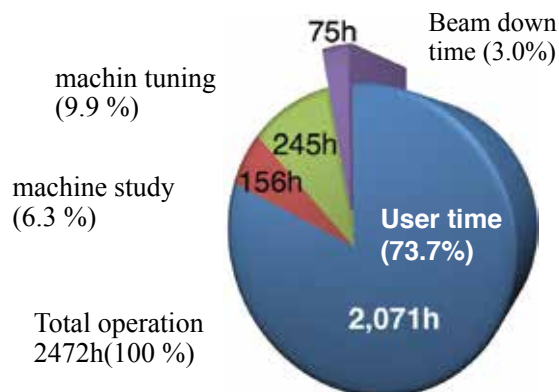


Fig.1 Operating time breakdown of NewSUBARU storage ring in FY2016.

user time, Friday is for 1.0 GeV or 1.5 GeV user time. Night period or weekend is used for machine study and user time with the special mode, such as a single bunch operation and a changing the electron energy, if necessary. As mentioned above, in the late half of FY2016, the NewSUBARU operated without the 1.5 GeV mode.

The total machine time in FY2016 was 2472 hrs, 121% of that of FY2015, excluding the beam down time. Figure 1 shows the breakdown. The beam down time includes not only the down by a failure, but also off-beam periods by a beam abort or others due to the machine trouble. The down time due to the machine trouble was 3.0 % of the total operation time. Main cause of this is the failure of auxiliary power supply for the inverse bending magnet.

## Machine Trouble

The machine troubles in FY2015 are listed in Table II. The rate of hardware troubles were increasing due to the aging.

Figure 2 shows overview of the NewSUBARU electron storage ring. The ring is consisted with 6 DBA cells with an inverse bending magnet at each cells. There are 6 straight sections between each

Table II Machine troubles in FY2016.

Group	Failure / trouble	down time (hr)
Safety interlock	Beam line, L4BT monitor, Emergency earthquake	5.93
Control	GUI, VME, Operator console	3.50
Magnet	Power supply failure, interlock	62.12
Other	Vacuum, Instability, UPS	3.10
		<b>74.65</b>

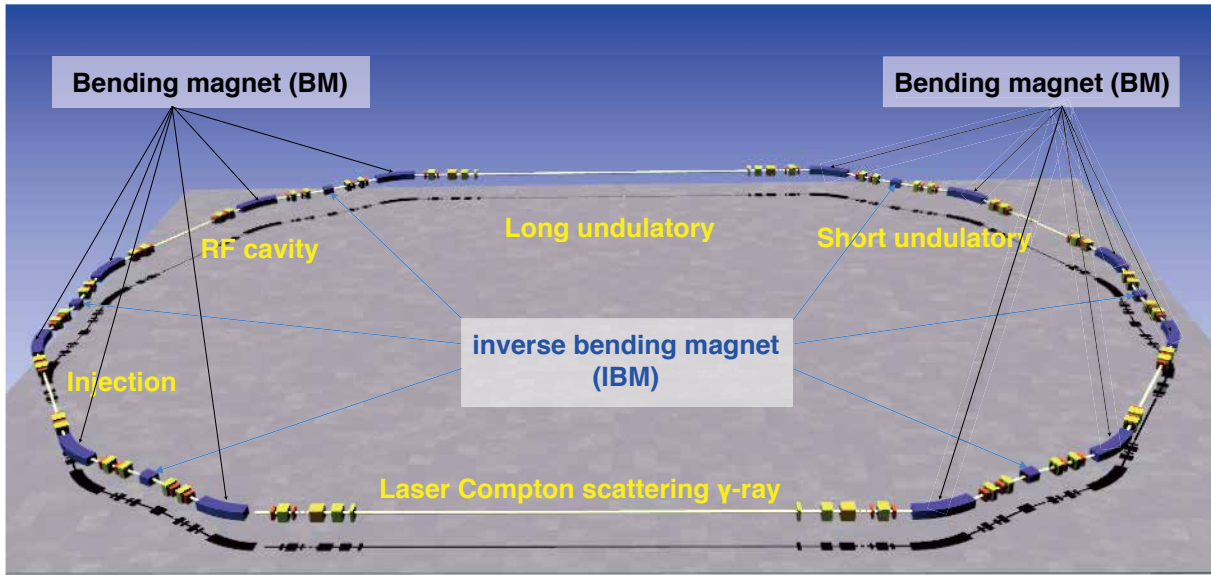


Fig.2. Layout of NewSUBARU electron storage ring. The ring consists of 12 bending magnet, 6 inverse bending magnet, multipole magnets and steering magnets.

cells, and they are used for an injection septum, an acceleration RF cavity, two undulators and a laser Compton scattering gamma ray source. A new beam line is possible to install at the last straight section.

#### Machine Study and Special User Time

Table III shows the list of machine studies in FY 2016. One of the new study issues is new filling test of electron storage ring. The usual filling pattern for user time is full fill 198 bunch plus two high current 70 bunch. The ratio between high current and low current bunches are 3:1 with total storage

Table III List of machine studies and special user mode in FY2016.  
(unit is an operation shift = 12 hrs)

R & D theme and special user mode	responsible person	operation shifts
New filling test for TOF	S.Miyamoto	5
Special filling & ion trapping	Y.Shoji	4
Tuning of 1.5 GeV acceleration	S.Hashimoto & M Niibe	6
SR monitor (SR-2) tuning	Y.Shoji	2
Deceleration sequence	S.Miyamoto	1

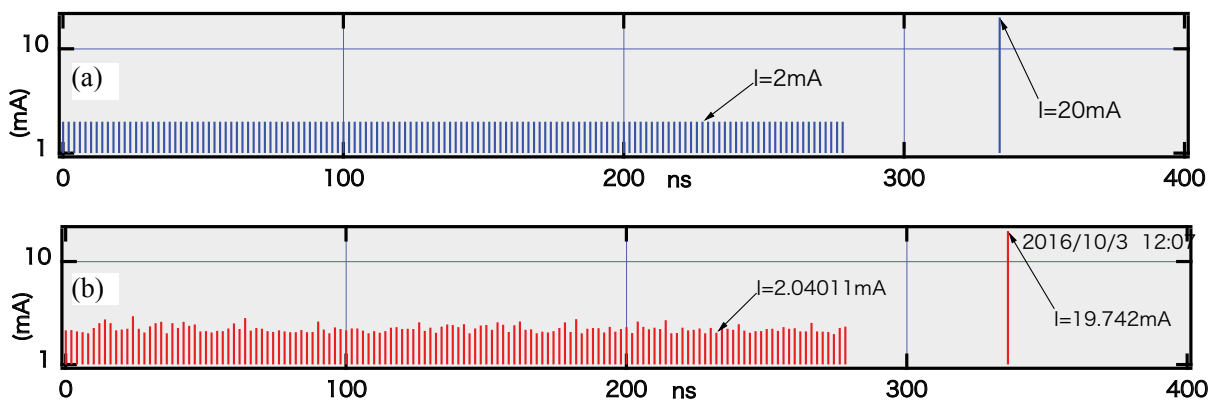


Fig.3. Filling pattern of the electron bunch in the storage ring. Horizontal axis shows a lap time of electron circulation. (a) Model of filling pattern model of quasi single bunch operation. (b) Example of a measured filling pattern of quasi single bunch operation. Total storage current is 300mA.

current of 300mA. We call this filling as “70+70+full fill 3:1”. The users, who want to applicate the time resolved study by synchrotron light, used single bunch electron mode where only one electron bunch of RMS pulse width of about 30ps is stored. Single bunch operation mode is not compatible with other synchrotron light users who uses “70+70+full fill 3:1” filling. Because of the current limit of 30mA for single bunch operation.

Figure 3 shows new filling pattern of the electron bunch in the storage ring. (a) is a filling model for quasi single bunch operation and (b) is an example of measured filling pattern. There are regions without an electron bunch of about 30 ns each before and after the high-current bunch. The user can use this high current bunch like a single bunch and can operate the total current of 300 mA. This operation mode is compatible with other synchrotron radiation users. It is possible to use single bunch beams during normal daytime with this filling.

### Auxiliary Power Supply Update

Figure 4 shows schematic circuit diagram of the bending and inverse bending magnets and power supplies are shown. The auxiliary power supply add a lack current at high field strength region. This current lack is due to different saturation performance of magnetic field of inverse bending magnet compare to the large bending magnet. This correction is only required for high magnetic field operation such as acceleration up to 1.5GeV electron energy.

Original auxiliary power supply was consisted of two 50A/50V dropper power supplies. One of these power supplies was failed. Updated auxiliary power supply is a 50A/100V switching power supply as shown in Fig.4. In the late half of FY2016, the operation cycles #5, #6, #7, NewSUBARU operated only low energy mode of the electron energy lower than 1GeV. The failed power supply was completed update by the end of FY2016.

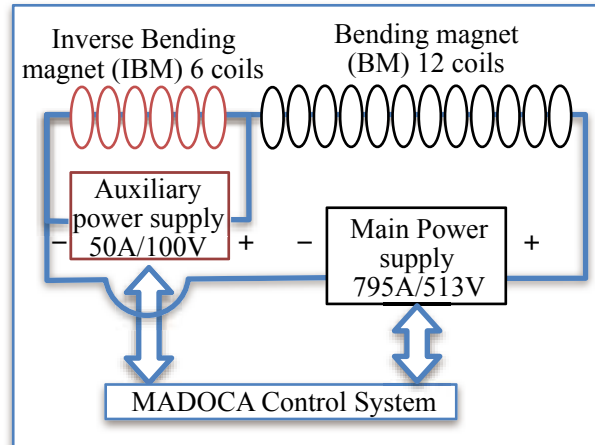


Fig.4. Schematic circuit diagram of the bending and inverse bending magnets and power supplies are shown. Updated auxiliary power supplies adding a lack current on the inverse bending magnets.

## Beamlines

Masahito Niibe  
LASTI, University of Hyogo

The arrangement of the beamlines in the NewSUBARU synchrotron radiation facility is shown in Fig.1. Total nine beamlines are operating in the NewSUBARU synchrotron radiation facility. Four beamlines of BL01, 03, 06 and 11 were constructed until 1999. Three beamlines of BL07, 09 and 10 were started the operation from 2000.

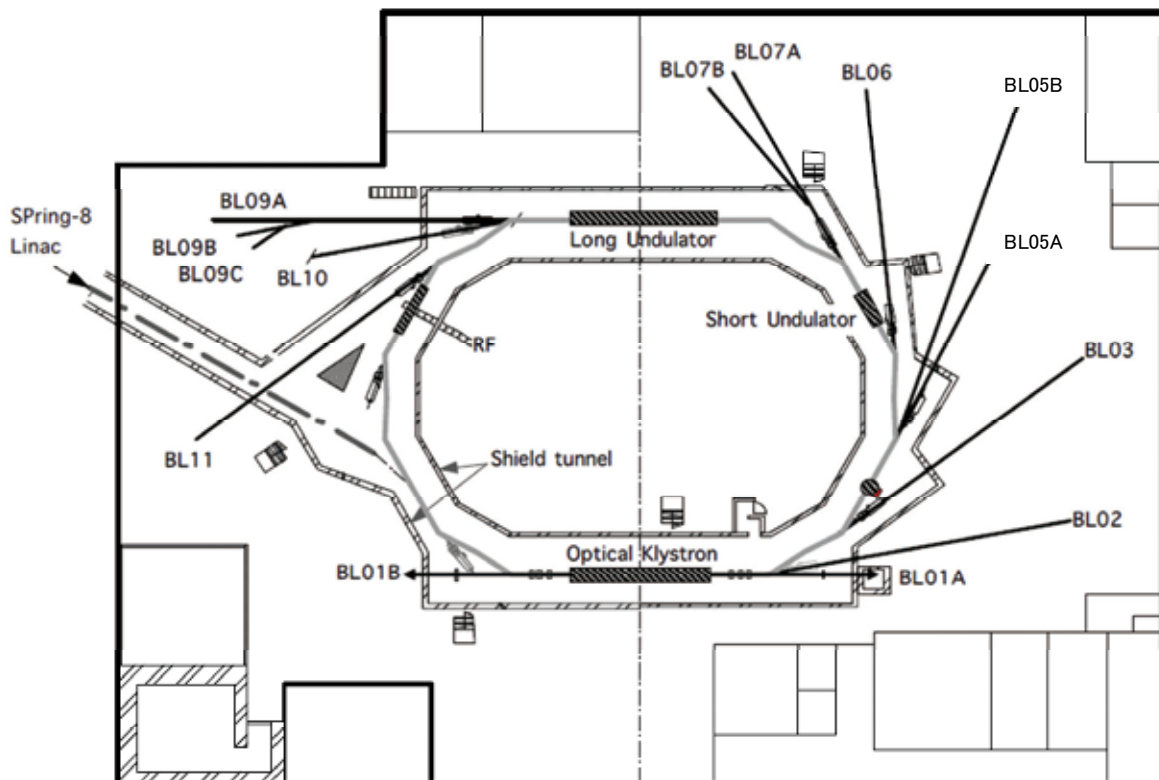
BL02 beamline was constructed for the usage of LIGA in 2003.

BL03B beamline branched from the BL03 beamline propose for the usage of the EUVL (extreme ultraviolet

lithography) microscope for the EUVL finished mask inspection.

BL05 beamline was constructed in response to a demand in the industrial world in 2008, which is the enhancement of the analysis ability in the soft X-ray region with the development of nanotechnology.

BL09B beamline branched from BL09 beamline for the usage of the usage of the EUV interference lithography to evaluate. And BL09C beamline branched from BL09B beamline for the usage of the thickness measurement of the carbon contamination originated to the resist outgassing during the EUV exposure.



## I. BL01

BL01 is a beamline for research and developing new light sources. This beamline is one of two long straight section on NewSUBARU. Optical klystron was installed at this straight section. Upstream side of this beamline (BL01B) is intended to be used for visible and infrared light generated from free electron laser (FEL) or synchrotron radiation (SR). Downstream side of this beamline (BL01A) is used for laser Compton scattering gamma-rays source. Gamma-ray beamline hutch just outside of the storage ring tunnel was constructed in

**Table 1.** Specification of BL01 gamma beam

CO <sub>2</sub> laser 10.52 μm 5W	Gamma energy : 1.7 - 4 MeV Gamma flux* : 9 x10 <sup>6</sup> γ/s : 6 x10 <sup>5</sup> γ/s (1.5-1.7 MeV) (with 3mmφ collimator)
Nd laser 1.064 μm 0.532 μm 5 W	Gamma energy : 17 - 40 MeV Gamma flux* : 7.5 x10 <sup>6</sup> γ/s : 3 x10 <sup>5</sup> γ/s (15-17 MeV) (with 3mmφ collimator)

\*Electron beam energy : 1-1.5 GeV

\*Electron beam current : 250 mA

## II. BL02

The LIGA (abbreviated name of Lithographic, Galvanoformung and Abformung) process which consists from deep x-ray lithography, electroforming, and molding process is one of the promising candidates for such 3D microfabrication. More than hundreds aspect ratio for microstructure can be attained by the usage of the higher energy x-rays (4-15 keV) from synchrotron radiation (SR) with deeper penetration depth to the photosensitive resist. In this system we have succeeded to enlarge the exposure area up to A4 size and the fabrication dimension from submicron to millimeter by varying the energy of the x-ray source in accordance with the size of desired microparts. Microstructure with high aspect ratio over several hundred will be achieved using the x-rays over 10 keV since high energy x-ray has deep penetration depth to the photo-sensitive resist materials. Whereas, in the case of lithography for low energy x-rays from 1 keV to 2 keV, submicron structures with high aspect ratio will be achieved using the x-rays mask with precise line-width and thinner absorber, since low energy x-rays has low penetration depth. Based on this principle, the beamline for x-ray exposure have constructed with continuous selectivity of x-rays from 100 eV to 15 keV by using the x-ray mirrors (plane and

\*Gamma-ray beam divergence : 0.5 mrad

2004 for gamma-ray irradiation experiments. Specification of this gamma-ray sources are listed in Table 1. New gamma-ray irradiation hutch "GACKO" was installed at BL01A, collaborating with Konan University. Table 2 shows the specification of "GACKO".

**Table 2.** Specification of "GACKO"

Maximum gamma-ray power	0.33 mW
Maximum gamma-ray energy	1.7 MeV - 73 MeV
CO <sub>2</sub> laser, wavelength/power	10.59 μm / 10W
1-1.7MeV gamma-ray flux	2×10 <sup>7</sup> γ/sec@10W/300mA
Nd:YVO <sub>4</sub> laser, wavelength/power	1.064 μm/ 30W, 0.532 μm/20W
10-17 MeV gamma-ray flux	5×10 <sup>7</sup> γ/sec@30W/300mA

cylindrical mirror) and Be film filters. The horizontal angle of the outgoing SR could be obtained up to 12.5 mrad, which corresponds to the horizontal size of 220 mm (A4 horizontal size) at the exposure position. The second characteristic performance of the beamline is the high efficiency differential pumping system. This was necessary for maintain the vacuum difference between the storage ring (<10<sup>-9</sup> Pa) and the end-station (<10<sup>-9</sup> Pa) at which gasses for substrate cooling will be introduced in the exposure apparatus.

The flexibility for the shapes and functions of microstructure will be enlarged by achieving 3D microfabrication process using multi step exposure at various configuration between x-ray mask and substrates. The relative positions between x-ray mask and substrates, tilt and rotation angle to the SR incident direction can be moved simultaneously during SR exposure using 5 axis stages. The movement of each axis is controlled by the PC in terms of the scanning speeds, scanning length, and repetition number. In order to decrease the heat load of sample substrate suffered during SR irradiation helium introduction and substrate cooling mechanism were also equipped. Specification of spectrometer is listed in Table 3.

**Table 3.** Specification of the LIGA exposure system

Optics	Plane and cylindrical mirror, Be filters
Exposure energy	100 - 2 keV, and 4 – 15 keV
Exposure method	Proximity and multi-step exposure
Wafer size	A4 or 8 inch
Exposure area	230 mm(H) × 300 mm(V)
Exposure environment	< 1 atm (He-gas)

### III. BL03

BL03 is a beamline for the developing the next generation lithographic technology so called extreme ultraviolet lithography (EUVL). The exposure tool is installed at the end station. Using this exposure tool, the research and development of the next generation lithography such as the less than 70 nm node is going on process. The exposure wavelength is 13.5 nm.

The semiconductor industry plays a very important role in the information technology (IT). In 2006, 256 Gbit DRAM with a gate length of 70 nm will be demanded in the IT industry. The extreme ultraviolet lithography (EUVL) is a promise technology for fabricating a fine pattern less than 70 nm. To meet this

schedule, this technology has to be developed in the pilot line until 2004. As for the practical use, it is very important that both to achieve large exposure area and to fabricate fine patterns. Therefore, at Himeji Institute of Technology, large exposure field EUV camera consists of three aspherical mirrors was developed. First in the world, we fabricated 60 nm line and space pattern in the large exposure area of 10 mm×10 mm on a wafer. Furthermore, BL03B beamline branches from the BL03 beamline propose for the usage of the EUVL microscope for the EUVL finished mask inspection. Table 4 shows the specification of ETS-1.

**Table 4.** Specification of the exposure tool (ETS-1)

Imaging optics	Three aspherical mirrors
Exposure wavelength	13.5 nm
Numerical aperture	0.1
Demagnification	1/5
Resolution	60 nm
Depth of focus	0.9 μm
Exposure area (static)	30 mm × 1 mm
Exposure area (scanning)	30 mm × 28 mm
Mask size	4 inch, 8 inch, and ULE 6025
Wafer size	8 inch
Exposure environment	In vacuum

### IV. BL05

BL05 was constructed in response to a demand in the industrial world, which is enhancement of the analysis ability in the soft x-ray region with the development of nanotechnology. BL05 consists of two branch lines for use in the wide range from 50 eV to 4000 eV. BL05A and BL05B are designed to cover the energy range of 1300-4000 eV and 50-1300 eV, respectively. The incident beam from the bending magnet is provided for two branch lines through different windows of a mask. Therefore, these two branch lines can be employed simultaneously. At the end stations of each branch, the transfer vessel systems were mounted for the measurements of sample without

exposure to air. In addition, globe box was placed for the preparation of samples into transfer vessel.

1) The double crystal monochromator was installed at the BL05A. InSb, Ge, Si, SiO<sub>2</sub>, Beryl and KTP crystals are prepared for a double-crystal monochromator. Toroidal mirrors are used as a pre-mirror and a focusing mirror of BL05A. XAFS measurement in the total electron yield mode and fluorescence XAFS measurement using SSD (SII Vortex) can be performed. The fluorescence XAFS spectra can be measured for samples at the end station filled with He gas. Table 5 shows the specification of monochromater.

**Table 5.** Monochromator specification

Monochromator	Double crystal monochromator
Monochromator crystals	SiO <sub>2</sub> ( 1010 ) , InSb ( 111 ) , Ge ( 111 ) , Beryl ( 1010 ) , KTP ( 110 ) , Si ( 111 )
Energy range	1300-4000 eV
Resolution	$E/\Delta E=3000$

2) The constant-deviation monochromator consisting of a demagnifying spherical mirror and a varied-line-spacing plane grating (VLSPG), which can provide high resolution, simple wavelength scanning with fixed slits, was mounted on BL05B. The optical system consists of a first mirror (M0), a second mirror (M1), an entrance slit (S1), a pre-mirror (M2), and three kinds of plane grating (G), an exit slit (S2) and a focusing mirror (M3). The including angle of the monochromator is 175°. Two measurement chambers

are prepared at the end station of BL05B. The XAFS spectra in the total electron yield mode and fluorescence XAFS spectra using SDD (Ourstex) can be measured in a high vacuum chamber. In addition, the photoelectron spectrum can be measured using spherical electron analyzer (VG Sienta, R3000) in an ultrahigh-vacuum chamber. The chambers can be replaced by each other within 1 hour. Table 6 shows the specification of the monochromator.

**Table 6.** Monochromator specification

Monochromator	Varied-line-spacing plane grating monochromator
Grating	100 l/mm, 300 l/mm, 800 mm/l
Energy range	50-1300 eV
Resolution	$E/\Delta E=3000$

#### V. BL06

BL06 has been mainly developed for irradiation experiments such as photochemical reaction, SR-CVD, photo-etching, surface modification. The white radiation beam from bending magnet is introduced to the sample stage using a pair of mirror, whose incident angle was 3°. The SR at BL06 sample stage had a continuous spectrum from IR to soft x-ray, which was lower than 1 keV. A differential pumping system can be

utilized for experiments in a gas atmosphere, which is difficult in the soft x-ray region. A sample holder can install four pieces of samples at a time. By using heater set in the sample holder, the sample can be heated from room temperature to 220°C. The temperature of sample is monitored using a Cr-Al thermocouple mounted on the sample holder.

#### VI. BL07A and BL07B

This beamline was designed for the development of new materials by SR technology. This beamline consists of two branch lines, which are provided with an incident beam from a 3-m-long undulator by switching the first mirror. One of them is a high photon-flux beamline with a multilayered-mirror monochromator for the study of SR-process (BL07A) and another is a high-resolution beamline with a varied line spacing grating monochromator for the evaluation of nano-structure characteristics by SR-spectroscopy (BL07B). The useful range of emitted photons from 50 to 800 eV is covered at both beamlines. The light source of BL07 is a 3-m length planar undulator, which consists of 29 sets of permanent magnets, a period length of which is 76 mm. The incident beam from the undulator is provided for two branch lines by translational switching of first mirror.

##### 1) BL07A

The multilayered-mirror (MLM) monochromator, which has high reflectivity in the soft X-ray region, was installed at the BL07A. It consists of a switching mirror chamber, a slit chamber, a MLM monochromator, a filter chamber and a reaction chamber. To obtain a large photon flux, we decided to use only first mirror (switching mirror), M0, for focusing. The MLM monochromator is designed to cover an energy range of up to about 800 eV by combination of three kinds of mirror pairs with 4 kinds of filter. The flux deliver by this design is estimated to be between a maximum of  $10^{17}$  photons/s at 95 eV and a minimum  $2 \times 10^{14}$  photons/s at 300 eV for a 500 mA ring current. Table 7 shows the summary of BL07A. In addition, X-ray fluorescence (XRF) apparatus using spherical varied line spacing grating was mounted at the downstream of irradiation chamber. The poly capillary was used to enhance beam-condensing efficiency. Measurement energy range was from 30 eV to 450 eV. This XRF

apparatus was expected to utilize the chemical analysis and N. on the light metals, Li and Be, and light elements, B, C

**Table 7. Summary of BL07A.**

Energy range (eV)	Multilayer mirror					Filter	
	Material	spacing	Thickness Ratio	number of layers	$\Delta E/E$	material	Thickness
50-60	Mo/Si	20 nm	0.8	20	6.2 %	Al	100 nm
60-95						None	—
90-140	Mo/B <sub>4</sub> C	11 nm	0.5	25	3.3 %	Ag	100 nm
140-194						Cr	500 nm
190-400	Ni/C	5 nm	0.5	60	2.5 %	Ni	500 nm
400-560							
550-800							

## 2) BL07B

The constant-deviation monochromator consisting of a demagnifying spherical mirror and varied line spacing plane grating (VLSPG), which can provide to high resolution, simple wavelength scanning with fixed slits, was mounted on BL07B. The optical system consists of a first mirror (M0), an entrance slit (S1), a premirror (M1), and three kinds of plane grating (G), an exit slit (S2) and a focusing mirror (M2). The

monochromator is designed to cover the energy range 50-800 eV with three gratings, of which including angle are 168°. The VLSPG has been well known to obtain high resolution in extreme ultraviolet region by diminishing various kinds of aberration. The total resolving power about 3000 can be realized in the whole energy region. Table 8 shows the specification of the monochromator.

**Table 8. Monochromator specification**

Mount type	Hettrick-Underwood type
Grating G1, G2, G3	Plane VLS (600 l/mm, 1200 l/mm, 2400 l/mm)
Energy range	50-150 eV, 150 – 300 eV, 300-800 eV
Resolving power (E/ $\Delta E$ )	~3000

## VII. BL09

A purpose of this beamline is studies on a soft x-ray interferometry or a holographic exposure experiment with making use of highly brilliant and coherent photon beams radiated from 11 m long undulator in NewSUBARU.

BL09 consists of M0 mirror, M1 mirror, G grating and M2 and M3 mirror. M0 and M3 mirrors are used for horizontal deflection and beam convergence, M1 is used for vertical beam convergence at the exit slit, and M2 is used for vertical deflection and beam convergence. A monochromator is constructed by M1 and a plane grating. The maximum acceptance of the undulator beam is 0.64 mrad in horizontal and 0.27 mrad in vertical. The acceptance can be restricted by 4-jaw slits equipped at upstream of the M0 mirror.

BL09A beamline is used for material analysis: X-ray absorption spectroscopy (XAS) and X-ray photoelectron spectroscopy (XPS). In 2013, X-ray emission spectrometer (XES) was introduced at the endstation of the BL-09A. The energy range and resolving power of the XES system was designed to be about 50-600 eV and 1500, respectively.

BL09B beamline branched from BL09 beamline for the usage of the EUV interference lithography for the evaluation of the exposure characteristics of EUV resist. Coherence length of 1 mm at the resist exposure position was achieved using BL09B beamline. And BL09C beamline branched from BL09B beamline for the usage of the thickness measurement of the carbon contamination originated to the resist outgassing during

the EUV exposure. Table 9 shows the specification of the monochromator.

**Table 9.** Monochromator specification

Mount type	Monk-Gillieson type
Grating	Plane VLS (300, 900, 1200 l/mm)
Energy range	50 – 750 eV
Resolving power ( $E/\Delta E$ )	~3000

### VIII. BL10

BL10 is for the global use in the Himeji Institute of Technology. M0 mirror is used for horizontal deflection and beam convergence, M1 is used for vertical beam convergence at the exit slit, and M2 is used for vertical deflection and beam convergence. A monochromator is constructed by M1 and a plane grating. At the beginning, the multiplayers reflectivity measurement was carried out at this beamline. The characteristics of this beamline and the result of the Mo/Si multiplayers measurement are carried out for the development of the EUV- mask technology.

BL10 utilizes a monochromator of the varied line spacing plane grating monochromator (VLS-PGM). The line density of the monochromator in central region of the gratings were 600, 1800 and 2,400 lines/mm. The reflectometer is a two axis vacuum goniometer using two Huber goniometers. One axis carries the sample, which may for example be a mirror at the center of the reflectometer vacuum tank ( $\theta$ -motion). The other ( $\phi$ -motion) carries the detector on a rotating arm. In

addition there are through-vacuum linear motions to translate the sample in two orthogonal directions (x,y). All motors are controlled by computer. The sample itself is mounted on a kinematic holder. The control stage monochromator rotation, and data analysis were program using LABVIEW software. The reflectivity result obtained at BL10 has a good agreement with that at LBNL. Table 10 shows the specification the monochromator.

The micro-CSM tool was adapted at the most downstream of the BL10 beamline for the EUV mask defect inspection. This too is very effective for the inspection of the actinic patterned mask.

A large reflectometer was installed in a branch line for large EUV optical component including EUV collector mirrors. The reflectometer has a sample stage with y, z,  $\theta$ ,  $\phi$ , and Tilt axis, which can hold large optical elements with a maximum weight of 50 kg, a diameter of up to 800 mm, and a thickness of 250 mm. The entire sample surface is able to be measured.

**Table 10.** Monochromator specification

Mount type	Hettrick-Underwood type
Grating	Plane VLS (600, 1800, 2400 l/mm)
Energy range	50 – 1,000 eV
Resolving power ( $E/\Delta E$ )	~1000

### IX. BL11

A beam line BL11 is constructed for exposure Hard X-ray Lithography (DXL) in the LIGA (German acronym for Lithographie Galvanoformung and Abformung) process. LIGA process, that utilizes a useful industrial application of SR, is one of the promising technologies for fabrication of extremely tall three-dimensional (3D) microstructures with a large aspect ratio. This process was invented at the Institut Fur Mikrostrukturtechnik (IMT) of the Karlsruhe Nuclear Center (KfK) in 1980. Microstructures with height of over a few hundreds  $\mu\text{m}$  have been widely applied to various fields such as micro-mechanics, micro-optics, sensor and actuator technology, chemical, medical and biological engineering, and so on. This beam line was designed by the criteria ; photon energy range from 2 keV to 8

keV, and a density of total irradiated photons  $\geq 10^{11}$  photons/cm<sup>2</sup>. The BL11 can provide the most suitable photon energy for microfabrication in X-ray lithography, while the BL2 is equipped for fabricating fine pattern submicron-scale structure and microstructure with high aspect ratio by selectivity of X-rays using movable mirror system. That is, LIGA process in NewSUBARU can provide the best 3D microfabrication because the BL11 and BL2 are complementary. The beamline BL11 is consisting of an absorber chamber, a first-mirror chamber (M1), a 4-way slit chamber, a Be and polyimide window chamber, and an exposure chamber. The horizontal angle of the outgoing SR could be obtained up to 17.8 mrad, providing a beam spot size on the exposure stage  $\geq 80 \times 10 \text{ mm}^2$ . The micron-scale structure with

high aspect ratio will be achieved using the toroidal typed mirror M1 which can produce a parallel collimated beam of X-rays. In addition, the homogeneity of the beam is excellently controlled by a novel adding system.

Using the precision stage in the exposure chamber, the flexibility for the shaped and functions of microstructure will be enlarged by achieving 3D microfabrication process using multi step exposure at

various configuration between x-ray mask and substrates. The exposure area of 200 mm × 200 mm is brought to fruition. In order to decrease the heat load of sample substrate suffered during SR irradiation, helium introduction and substrate cooling system were also equipped. The specification of the LIGA exposure system is listed in Table 11.

**Table 11.** Specification of the LIGA exposure system

Exposure method	Proximity exposure
Wafer size	8 inch
Exposure area	200 mm(H)×200 mm(V)
Exposure environment	< 1atm (He-gas)

### **Establishment of Research Center for Advanced Synchrotron Radiation Analysis**

In order to respond to diverse analysis needs from industries, it is necessary to advance technological development for analyzing beamlines (BLs) of NewSUBARU synchrotron radiation facility to advance integrated and strategic development of analyzing technology. For this reason, the Research Center for Advanced SR Analysis was launched in

August 2016. As an organization crossing in university courses, this center is consulted and administered by all members of the LASTI related to analysis, and in collaboration with the SR Nanotechnology Center of Hyogo Prefecture, a wide range of energy from hard X-rays to soft X-rays. We aim to respond to various analysis needs of the area on a one-stop basis.

### **Acknowledgement**

We would like to thank all the staff who work at NewSUBARU synchrotron radiation research facility for their help to describe the update details of the beamlines.

# Laser Compton scattering gamma ray generated using Yb fiber laser and Er fiber laser in NewSUBARU BL01

Kento Sugita, Yuusuke Morimoto, Satoshi Hashimoto, Sho Amano, Shuji Miyamoto  
LASTI, University of Hyogo

## Abstract

Laser Compton scattering (LCS) MeV gamma ray beams are produced by head on collision between circling electron in NewSUBARU storage ring and laser photon. Using Yb fiber laser (1064nm) and Er fiber laser (1550nm) LCS-gamma flux is  $1.0 \times 10^3$  photon/mA/W/s and  $2.0 \times 10^2$  photon/mA/W/s, at gamma ray energy of 17MeV and 11MeV, respectively. These gamma rays are collimated two collimators diameter of 6mm. These new pulse laser system are possible to synchronize with the electron beam in the NewSUBARU storage ring. This system will be used for time-of-flight experimental in future.

## Introduction

We developed the high energies gamma ray source using Laser Compton scattering at NewSUBARU BL01 [1-3]. Laser Compton scattering gamma ray (LCS-gamma) is produced by collision between relativistic electron in storage ring and laser photon. LCS-gamma energy  $E_\gamma$  is described as following

$$E_\gamma = \frac{4\gamma^2 E_L}{1 + \gamma^2 \theta^2 + \frac{4\gamma E_L}{m_e c^2}} \quad (1)$$

where

$$\gamma = \frac{E_e}{m_e c^2}$$

$E_L$  is the energy of laser photon,  $\gamma$  is the relativistic coefficient,  $E_e$  is the kinetic energy of circling electron in the storage ring,  $m_e$  is the rest mass of electron,  $c$  is the velocity of light and  $\theta$  is the angle between the direction of the incident electron and the generated  $\gamma$ -ray. The energy of LCS-gamma-ray can be adjustable by changing the laser wavelength or by changing

the electron energy. This paper presents performances of LCS-gamma systems using new lasers for future application experiments using  $\gamma$ -ray.

## Generation and measurement of LCS-gamma

Figure 1 shows the system of LCS-gamma source at BL01. The laser is injected into the storage ring tunnel by passing two mirrors. In the accelerator tunnel, the laser passes through a mirror, a lens and a vacuum window into the vacuum duct. The laser beam axis is aligned to the electron beam axis by adjusting two mirrors at the outside. The scattered laser photon is boosted up to the gamma ray energy. The generated  $\gamma$ -ray passes through the first collimator in tunnel and the second collimator in optical hatch-1, to reach the optical hatch-2 (GACKO).

Gamma ray flux was measured using NaI detector at GACKO. New Yb fiber laser (KEOPSYS, wavelength 1064nm, pulse width 1 ns) and Er fiber laser (KEOPSYS, wavelength 1550nm, pulse width 6ns) was introduced at LCS-gamma system. Energies of  $\gamma$ -ray generated with 1-GeV electron beam using Yb laser and Er laser are calculated using Eq. (1) as

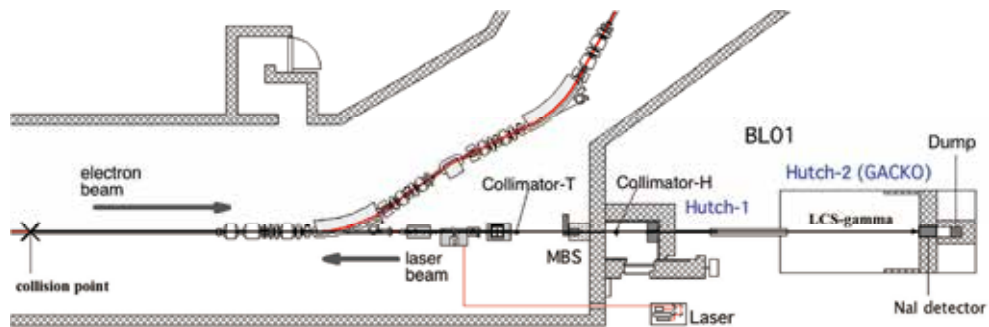
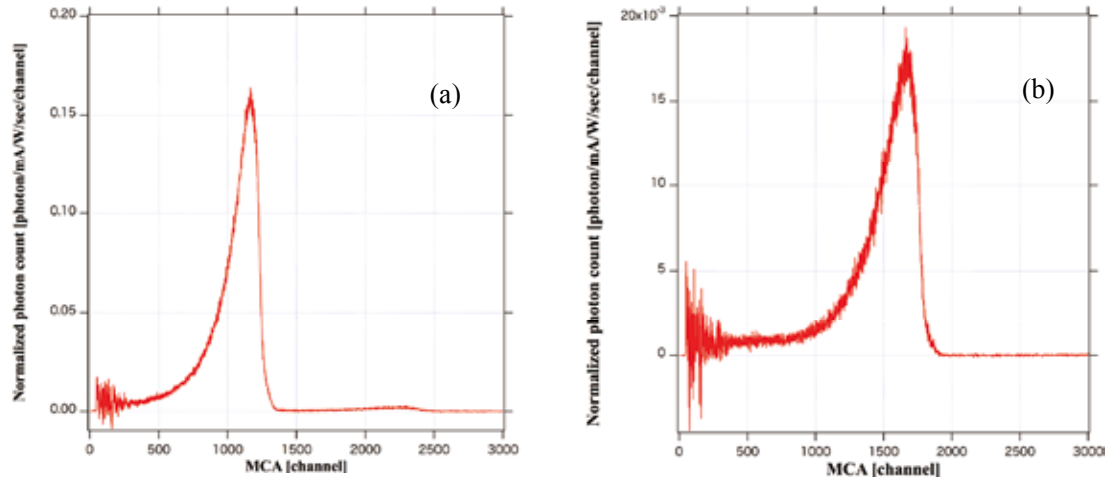


Fig1. LCS-gamma system at NewSUBARU BL01.



**Fig2.** Measured signal of the gamma photon flux as a function of energy using (a) Er-fiber laser and (b) Yb-fiber laser. large NaI detector was used.

17-MeV and 11-MeV, respectively. Collimators of 6mm in diameter are used in tunnel and hutch-1. The normalized fluxes of  $\gamma$ -ray were measured to be  $1.0 \times 10^3$  and  $2.0 \times 10^2$  photons  $\text{mA}^{-1}\text{W}^{-1}\text{sec}^{-1}$  using Er laser and Yb laser, respectively. Figure 2 shows measured LCS-gamma photon signals using a NaI detector (8inch  $\times$  12inch). Signals were recorded by multi channel analyzer (MCA). Vertical axes are the intensity of gamma photon and horizontal axes are the channel number of the MCA. Channel of horizontal axis is equivalent to energy of gamma photon. Approximately 2000 channel correspond to 20-MeV. Figure 3 shows the image of gamma-ray beam taken at hatch-2. In this case, two 6mm  $\phi$  collimators were used, in the tunnel and in the hutch-1. The image was recorded by a single photon counting multi-pixel device MiniPix. The size of imaging area of MiniPix detector is 14mm  $\times$  14mm with 256  $\times$  256 resolution. Shooting time of Figure 3 is 100 seconds in integration. Diameter of LCS-gamma image is about 8mm. This result is reasonable consider the position of collimator and distance from scattering point to the imaging position. This imaging device is useful to align small irradiation targets in the gamma-ray hatch.

#### Future use

We have introduced two new laser system into the LCS-gamma source beamline BL01. These systems are useful for the study of neutron time of flight measurement for photo neutron.

Next step, we are planning to synchronize these laser pulse with the circulating quasi-single bunch electron in the NewSUBARU electron

storage ring.

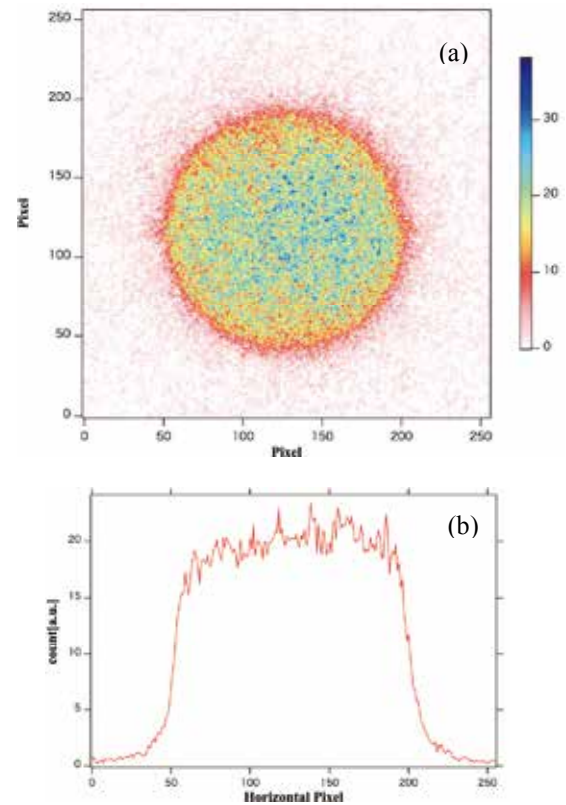


**Fig3.** LCS-gamma image taken by MiniPix. (a) LCS-gamma image (b) line profile of LCS-gamma image.

#### Reference

- [1] S. Miyamoto *et al.*, Radiat. Meas. **41** (2007) S179.
- [2] S. Amano *et al.*, Nucl. Instr. and Meth. A (2009), doi:10.1016/j.nima.2009.01.010
- [3] K. Horikawa *et al.*, Nucl. Instr. and Meth. Physics Research. A **618**(2010) 209-215.

# Development of fast positron measurement apparatus for defects study in bulk materials

F. Hori, Y. Ueno, Y. Sumikura, A. Iwase, Graduate School of Eng., Osaka Pref. Univ.  
K. Sugita, Y. Takemoto, S. Miyamoto, M. Terasawa, LASTI, Univ. of Hyogo

## Abstract

We have been developed a new positron beam apparatus in a synchrotron radiation facility NewSUBARU at LASTI, University of Hyogo, Japan. Highly energetic positrons were created via pair creation in a Pb plate by injection of mono energetic gamma photons generated via laser Compton scattering (LCS) of a high power Nd laser and GeV ordered electron circulating in a storage ring. Generated high energetic positrons are directly injected into target sample placed in a vacuum chamber. By measuring positron annihilation Doppler broadening energy spectra, internal defects and electron density distribution can be detected. We have performed positron annihilation Doppler broadening measurement for bulk amorphous and crystal samples without destruction.

## Introduction

Positron annihilation techniques are useful tool to detect various types of defects and to estimate local electronic state in solids. Recently, there are many positron beam apparatus have been constructed in many research facilities but they are almost all slow positron beam the energy of about 10 keV. Such slow positron beam can be reached and annihilated at only near surface in solid, the maximum range of 10 nm at most. A new positron beam apparatus, which can be generated as mega eV ordered fast positron, has developed at NewSUBARU photon facility. So far, we have successfully detected defects generated in bulk iron samples after fatigue stress applied [1]. By using this apparatus, it is possible to detect defects existing in bulk materials. In our research study, we have tried to detect defects, which are induced by different conditions such as fatigue stress, radiation damage, corrosion induced defects and their annealing behavior in bulk materials without sample destruction. In this report, we have shown the improvement of fast positron

apparatus and one of the positron measurement results as a demonstration.

## Positron system setup

Figure 1 shows that the schematic illustration of positron generation and measurement system. The LCS gamma ray generation and positron annihilation apparatus at the beam-line (BL01A) of the electron storage ring at the NewSUBARU SR facility at LASTI, University of Hyogo. LCS gamma rays an energy of 16.7 MeV have been generated from laser light with a wavelength of 1064 nm from a Nd laser and 1 GeV electron beam circulating in the storage ring. By using LCS gamma rays, positron and electron pair creation has done in Pb target mounted on simple positron apparatus in GACKO space as shown in this figure. The generated positron and electron pairs can be bent to opposite directions according to the magnetic field and are then separated, while the penetrated gamma ray photons are not influenced by the magnetic field. Sample is placed where on the line 8.3 MeV positron passing through in a

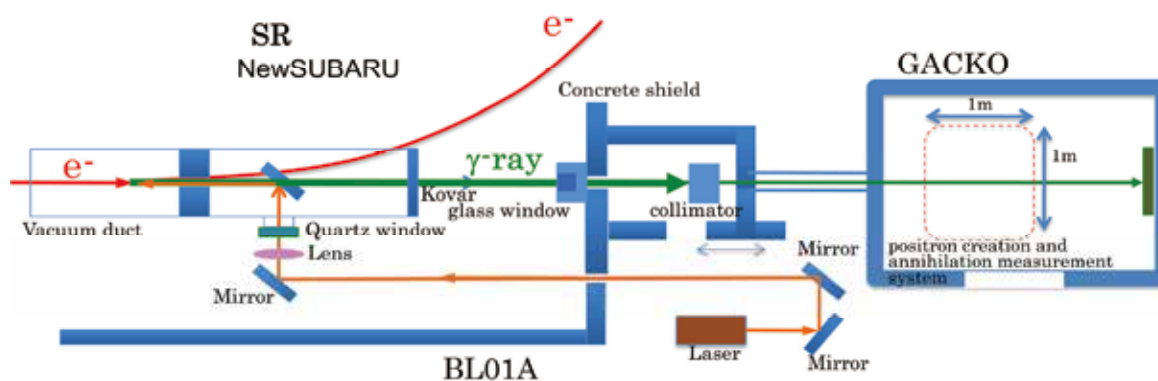


Figure 1 Schematic illustration of positron generation and annihilation measurement system at NewSUBARU.



Figure 2 Fast positron generation and annihilation measurement system.

vacuum chamber, for positron annihilation Doppler broadening measurement. Figure 2 shows the photo of developed fast positron generation and Doppler broadening measurement system at NewSUBARU. Positron annihilation signal of 511 keV gamma photons were emitted from the sample and detected by a HP-Ge detector with cooling device X-COOLER-III. This measurement can be performed in air, vacuum and any gas atmosphere. To reduce the background radiation, the detector was covered by 50 mm thick Pb block and the annihilation gamma rays were restricted by a 30 mm diameter Pb aperture. By using pure iron with the size of 20 x 40 x 5 mm, measured system conditions are listed in Table 1. LCS gamma and generated positrons by pair creation were more than  $10^5 \text{ MeV}^{-1}\text{s}^{-1}$  and  $3600 \text{ s}^{-1}$  respectively [2]. Maximum count rate of the positron annihilation gamma measured by HP-Ge was about 500 cps. This value depends on incident laser power.

### Positron annihilation measurement

The amorphous and crystal states of Zr-based alloy samples with same chemical composition were measured by using this positron measurement system. This alloy can be molded as amorphous state by rapidly quenching method above melting point [3]. The shape of both samples is a cylinder with 30 mm diameters and 40 mm height. Figure 3 shows the result of positron annihilation Doppler broadening measurement for these alloys [4]. This difference of energy distribution originated from the different atomic density. Relative atomic density difference in these samples is about 0.4%. Figure 4 shows the positron annihilation depth profile calculated by PENELOPE code based on the Monte Carlo simulation [5]. As seen in this figure, incident peak appears around 2 mm in this sample. Then, we have successfully measured their different atomic density originated from larger space of open volume quenched in amorphous comparing to inter atomic space of crystal state of same alloy.

Table 1 Positron generation system conditions

SR electron	Laser (Nd)	LCS gamma ray	Positron
1 GeV	1064 nm	16.7 MeV	8.3 MeV
200 mA	4.5 W	$10^5 / \text{MeV}/\text{s}$	100~500 cps

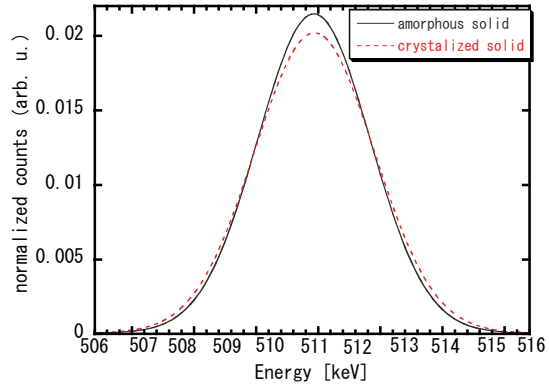


Figure 3 Positron annihilation Doppler profiles in the bulk amorphous and crystal samples.

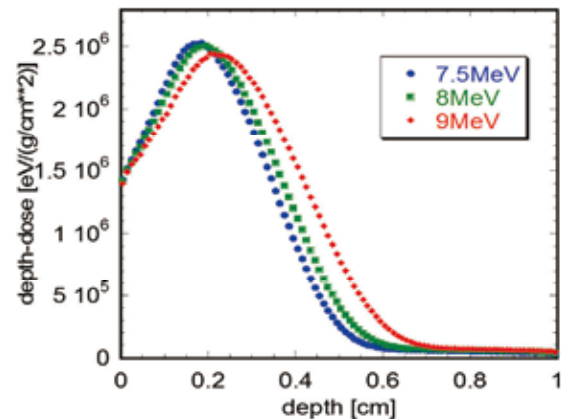


Figure 4 Calculated positron implanted depth in metal by Monte Carlo simulation.

### Acknowledgement

This work was performed using NewSUBARU GACKO (Gamma Collaboration Hutch of Konan University). The authors would like to express our thanks to staff at the NewSUBARU SR facility for their kind help in beam setup. This work was grant supported by the Japan Society for the Promotion of Science (JSPS) Research (Grant-in-Aid for Scientific Research, B, no.26289365) and Metal Technology Co. Ltd.

### References

- [1] F.Hori et al., *Jpn. J. Appl. Phys. conf. proc.* 2 011301 (2014).
- [2] K.Horikawa, S.Miyamoto, S.Amano, and T.Mochizuki: *Nucl. Instrum. Methods A* 618 (2010) 209.
- [3] Y.Yokoyama, A.Inoue, K.Fukaura, *Mater. Trans.* 43 (2002) 2316.
- [4] F.Hori, et al., *J. Phys. conf. Ser.* 674 (2016) 012025.
- [5] PENELOPE: Monte Carlo code developed by Nuclear Energy Agency.

# Mechanical stability of the main axis of the double multilayer monochromator in BL07A

Masato Okui<sup>1)2)</sup>, Naoki Yato<sup>1)</sup>, Ren Konno<sup>1)</sup>, Akinobu Watanabe<sup>1)</sup>, Osamu Shiga<sup>1)</sup>,  
Norio Murayama<sup>1)</sup>, Sei Fukushima<sup>2)3)</sup> and Kazuhiro Kanda<sup>2)3)</sup>

1) Kohzu Precision Co., Ltd., 2) LASTI, University of Hyogo,  
3) Kobe Material Testing Laboratory Co., Ltd.

## Abstract

Mechanical stability of the main axis of a monochromator is basement on machine study to get higher beam stability from monochromator even if the other factors are more influence on the problem. In this study, the mechanical stability of the main axis of MKZ-7NS type double multilayer monochromator installed on BL07A in New SUBARU. Since about 1 hour after the start of measurement when the monochromator would regard to reach thermal equilibrium, the measured relative displacement was shown starting to have been decreased slowly as like linear regression unlike the earlier exponential. The total relative displacement of the main axis theta1 of this monochromator in this experiment is about -1.6 arcsec during 6hours. The displacement would be also stopped at this angle after then.

## Introduction

Recently, necessary beam size for a synchrotron beamline is trend to smaller than it of the decade before since a beamline using micro beam is being increased than the before. Therefore, optical stability of monochromator on a beamline would need to keep higher from point of view of many user experiments using micro beam than before.

There are many factors would have significant influence over the stability of beam position from monochromator during experiment using beamline.

For example, thermal expansion of mechanical parts by Compton scattering or heat transfer from driving motor or vibration by compressor of cooling system so on are considered as the one of troubling factors on beam stability having influence on.

However, it might be rare case that only mechanical stability of an axis of monochromator is examined in beamline in machine study of a monochromator.

The authors have considered the mechanical stability should be basement on machine study to get higher beam stability from monochromator even if the other factors are more influence on the problem.

In this study, we were examined mechanical stability of our MKZ-7NS type double multilayer monochromator installed on BL07A in New SUBARU as test case.

## Experimental

The experiment was in performed on BL07A in New SUBARU where Fig.1 shows the panoramic view of that beamline and the photo of MKZ-7NS type monochromator.

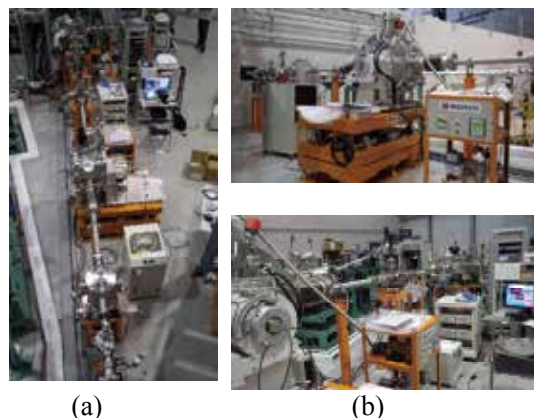


Fig.1. (a) Photograph of panoramic view of BL07A and (b) photograph of MKZ-7NS type monochromator.

The MKZ-7NS type monochromator is controlled by an integrated computing algorithm on the control application installed at personal computer [1]. The specification and the suitable feature for industrial use of this type multilayer monochromator are also showed by Okui *et al.* [1]. Fig.2 shows the schematic system drawing.

Photon energy was 130eV in BL07A line at this experiment, and then the ID gap of the undulator is 48.3mm in the beamline. Ring energy was 1.5 GeV and decay mode.

After beam injection from the linac, the

alignment all axes of monochromator tuned and just immediately started measuring the mechanical stability of main axis  $\theta 1$ .

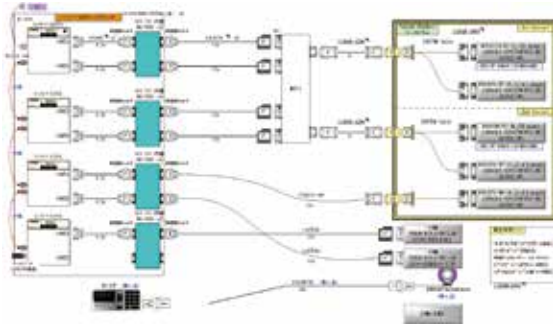


Fig. 2. The schematic system drawings of MKZ-7NS type monochromator

The positional motor pulse of all axes was kept to the initial pulse so that the tuned positions have never moved. The stability of  $\theta 1$  was measured by ring scale encoder (Heidenhain RON886). And motor pulse of the main axis  $\theta 1$  was monitored by the motor controller to confirm to fixing motor pulse of the axis at the initial pulse.

### Result and Discussion

Result of experiment is shown as Fig.3. In the figure, the vertical axis shows relative positional displacement from the initial position of the main axis  $\theta 1$  after the all axes tuned and the horizontal axis shows the elapsed time since starting this experiment.

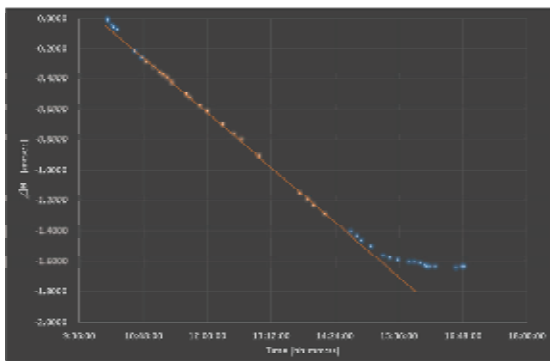


Fig. 3. Mechanical stability of the main axis  $\theta 1$  of MK-7NS type monochromator set on BL07A in New SUBARU.

During the experiment, the count numbers of motor pulse of the main axis  $\theta 1$  was as same numbers as the start count numbers. This fact shows the main axis was not moved by the control system. For this reason, it is just suggested that the displacement of position measured by read the ring encoder shall indicate mainly the mechanical stability of the main axis

of this MKZ-7NS monochromator.

From the result shown as Fig.3, the relative position of the main axis  $\theta 1$  from the initial position have decreased as exponential since the start of experiment till about 1hour after. This exponential decrease would be able to presume to have been influenced by thermal change of several reason as like as Compton scattering or motor and mechanical heating since the curve would be exponential as like as thermal diffusion equation.

Since about 1hour after the start of measurement when the monochromator would regard to reach thermal equilibrium as like the above inference, the measured relative displacement be shown starting to have been decreased slowly as like linear regression unlike the earlier exponential. This decrease continues 6 hours after then.

It can be suggested that this linear decrease would be shown the mechanical stability of the main axis of the monochromator, MKZ-7NS.

The total relative displacement of the main axis  $\theta 1$  of this monochromator in this experiment is about -1.6 arcsec.

The direction of displacement is the decrease of Bragg angle and that the direction is the gravity direction. This direction would be able to just suggest the displacement of the main axis would be caused by gravity.

However, this experiment suggests this movement would be also stopped at a certain smaller angle, -1.6arcsec. Thickness of meshed surface of the gear of  $\theta 1$  would be about  $1 \mu m$  estimated by considering of the diameter of worm wheel. It can be suggested that this linear decrease would show the mechanical stability of main axis  $\theta 1$  of the monochromator, MKZ-7NS.

### Acknowledgement

The authors appreciate for Mr. Shotaro Tanaka University of Hyogo for his support in our beam time.

### References

- [1] Okui *et al.*, AIP Conference Proceedings **1741**, 030033, (2016).

# Energy Calibration and Spike Noise Reduction for Ultra-soft X-ray Fluorescence Spectrum on BL07A

Sei Fukushima<sup>1,2\*</sup>, Hiroki Takamatsu<sup>1</sup>, Shotaro Tanaka<sup>1</sup>, Kazuhiro Kanda<sup>1</sup>

1: LASTI, University of Hyogo, 3-1-2 Koto Kamigori-cho, Ako-gun, Hyogo 678-1205 Japan

2: National Institute for Materials Science, 1-2-1 Sengen, Tsukuba-shi, Ibaraki 305-0047 Japan

## Abstract

On the development and investigation of ultra-soft X-ray fluorescence spectroscopy, the establishment of both energy calibration process and efficient noise reduction process should be so important for realization of the practical use. The results of the investigation about these two processes are presented in this report for the high-performance type spectrometer on BL07A.

## Introduction

For analyzing the chemical state or the electronic structure of valence band, one of the most popular and widely used method is XAFS (X-ray absorption fine structure) measurement. Of course, NewsUBARU has been already executed and obtained many remarkable results in the field of ultra-light elements. However, one of the disadvantage points of XAFS measurement is the necessity of sweep the energy of incident X-rays. As known well, the efficiency of excitation for core level of such ultra-light element is so low, thus highly condensed monochromated X-ray beam with high photon flux should be necessary for measurement.

In contrast, the energy sweep of incident X-rays are not necessary for obtaining any fluorescent (characteristic) X-rays from the samples. Thus, the examination about the possibility of application of fluorescent X-rays of ultra-light elements is important as a practical meaning.

Instead of the X-rays for excitation,

electron beam is also available for obtaining characteristic X-rays, and this manner is already widely used as the EPMA (electron probe micro analyzer) analysis. This manner is also efficient for the ultra-light elements, and, some of the members of this group have already fabricated EPMA system for the chemical state analysis of ultra-light elements [1]. As already shown in the Annual report in 2015FY, the spectrometer for fluorescent X-rays was already confirmed its specification, and has been continue to adjustment at BL07A.

Till the last FY, the adjustment of spectrometer had been finished, and the solution of some problems in beamline had been made. And during this process, calibration manner of spectrometer and removing the spike noise from the measurement data were revealed as the items which should be solved.

In this report, the countermeasures are presented.

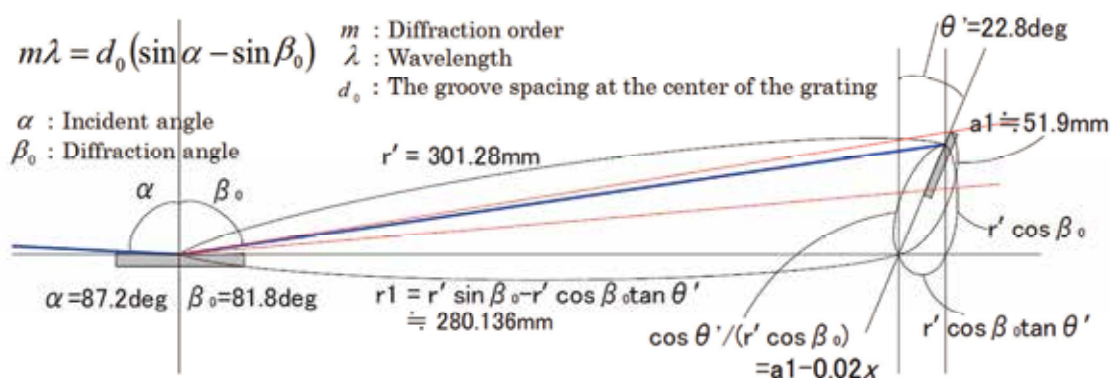


Fig.1 The schematic geometry of the ultra-soft X-ray fluorescence spectrometer

\*) present belonging: Kobe Material Testing Laboratory Co., Ltd.

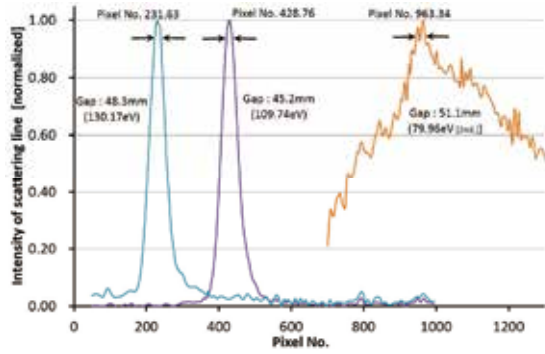


Fig.2 The pixel numbers at three peak positions caused by the scattering of incident SR source X-rays.

### Energy calibration of the spectrometer

As already mention in previous report [1], the detector of the spectrometer for the measurement of fluorescent X-rays is CCD camera. The light receiving surface of CCD camera is just set at the dispersion plane of the grating of spectrometer. The dispersion direction of the grating is made exactly to agree with the direction of pixel lines on the plane of projection. Thus, it is possible to obtain the fluorescent X-ray spectrum by means of taking the total of the signal strength of the line of pixels perpendicular to the dispersion direction. And, the conversion from the pixel line number to energy value is the necessary step of obtaining any spectrum.

In Fig.1, the geometry between the grating and the light receiving plane of CCD camera (camera surface) is shown. The notation and the typical values of necessary variables are also shown in this figure. In this CCD camera, the size of 1 pixel is 0.020mm, and if  $x$  is the pixel line number,  $a1-0.02x$  is the distance between the top of the camera surface (the top of  $a1$  in Fig.1) and the  $x$ th pixel line. Thus, the wavelength  $\lambda$  of X-ray monochromated by this system can be described as follows.

$$m\lambda = d \left[ \sin \alpha - \cos \left\{ \arctan \left( \frac{(a1 - 0.02x) \cos \theta'}{r1 + (a1 - 0.02x) \sin \theta'} \right) \right\} \right]$$

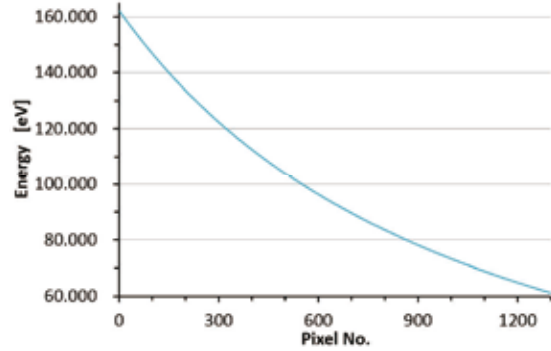
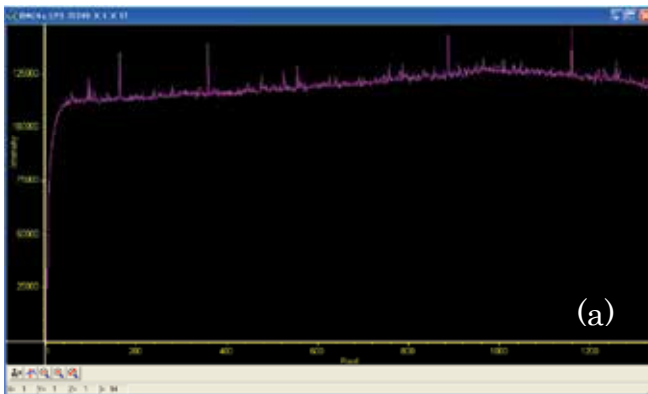


Fig.3 Pixel number – energy calibration curve obtained with Fig.2 and eq.(1).

...(1)

If three or more sets of data which consist with the wave length  $\lambda$  (or the energy value) and the pixel line number  $x$  corresponding with that energy value are obtained, eq.(1) is decided by the fitting procedure with a little adjustment of the values of  $\alpha$ ,  $r'$  (or  $r1$ ) and  $\theta'$ .

Ideally, the set of values of  $(x, \lambda)$  should be obtained from the any fluorescent X-ray lines. However, in the status, no lines were observed. Thus, the peak position originated in the excitation X-ray which was decided by the set-up condition of the undulator and beamline monochromater was used.

In Fig.2, 3 peaks are shown with its energy calculated with the gap value of the undulator and the each value of  $x$ . And, the obtained calibration curvature is shown in Fig.3.

### Spike noise cut filter

Fig.4 shows that the CCD image and a spectrum fabricated from this image which were obtained without any X-rays. A lot of

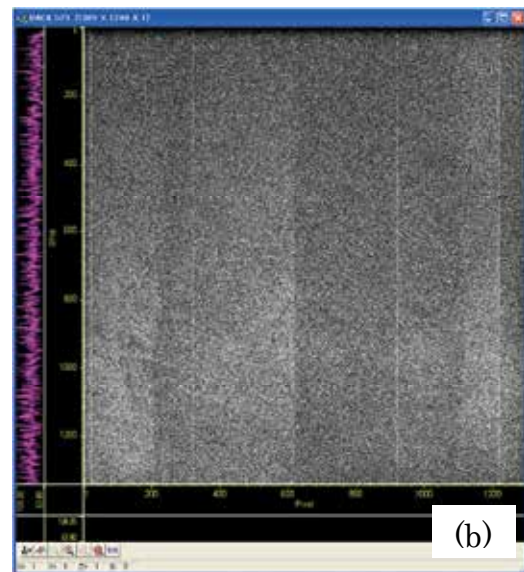


Fig.4 An example of background spectrum (a) and the CCD image (b) corresponding with (a).

spikes are observed on this spectrum, and these are significantly higher signal intensity than average signal intensity (background). The origin of these spike noise is the deterioration of the CCD camera.

One of the effective numerical data processing method for removing these spike noise is Median filter. In comparison with the any smoothing filter such as Savitzky-Golay filter[2], data distortion due to any spike noise on the processed spectrum can be suppressed. However, if a measured spectrum has so small structure that is hard to confirm before noise cut processing, there is not the conclusive evidence that such small structure should be stored in Median filter. Thus, new numerical process for only removing spike noise was tried to apply.

As known well, the algorism of the Median filter is as;

1. Take a data point  $x_i$  set for all spectrum data  $\{x_0, \dots, x_n\}$ .
2. Take a consecutive data set  $\{x_{i-m}, \dots, x_{i+m}\}$  for  $x_i$ .
3. Calculate the value of the median  $M$  of this set, and replace  $x_i$  by  $M$ .
4. Take  $i+1$  instead of  $i$ , then repeat the step 2 and 3.

The result by this process, due to the replace most of all measured data by the median values, it cannot be said with sure that any small and weak structure on the measured spectrum should be stored on the processed spectrum.

Thus, a partly remodeled median filter was tried to apply as a spike noise cut filter. The algorism of this spike noise cut filter is as;

1. Take a data point  $x_i$  set for all spectrum data  $\{x_0, \dots, x_n\}$ .
2. Take a consecutive data set  $\{x_{i-m}, \dots, x_{i+m}\}$  for  $x_i$ .
3. Calculate the value of the median  $M$  of this set.
4. If  $x_i \geq M$ , replace  $x_i$  with  $(x_{i-1}+x_{i+1})/2$ . And if  $x_i < M$ , nothing is operated.
5. Take  $i+1$  instead of  $i$ , then repeat the step 2, 3 and 4.

In above process,  $x_i \geq M$  is the criterion for that  $x_i$  is a spike noise or not. And, no operation when  $x_i < M$  is the guarantee that any small and weak structure is stored.

One of the results of this spike noise cut filter is shown in Fig.5 as an example. It can be seen that almost all spike noise peaks are removed by the processing with this filter.

#### Acknowledgement

The authors thank gratefully Kazunori Tsukamoto and Dr. Toyohiko Tazawa (JEOL ltd.) for the adjustment of the equipment.

#### References

- [1] S. Fukushima *et al. Microchim. Acta* **161** 399 (2007)
- [2] A.Savitzkey *et al. Anl. Chem.* **36** 1627 (1964)

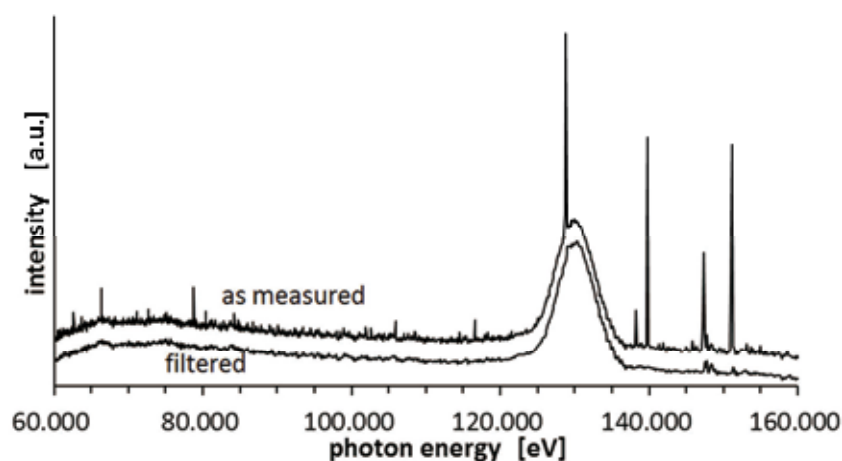


Fig.5 An example of the results of the spike noise cut process. Almost all noise spikes are removed.

# Development of a transfer vessel system for XAS analysis of anaerobic samples in BL10

Yasuji Muramatsu and Keigo Yoshida  
Graduate School of Engineering, University of Hyogo

## Abstract

A transfer vessel system was developed for X-ray absorption analysis of anaerobic samples in BL10. The system was designed considering the following conditions; (1) The usual large-size sample plate can be transferred from a glovebox to the preparation chamber in BL10, (2) Size of the vessel should be smaller than  $300 \times 200 \times 200 \text{ mm}^3$ . The system has been successfully developed and been used in the period of 2017B.

## 1. Introduction

The analysis station for X-ray absorption spectroscopy (XAS) has been developed and installed upstream the X-ray reflectometer in BL10 at the NewSUBARU [1-4]. The XAS station enables the chemical/electronic-state analysis, and the X-ray reflectometer enables layer structure analysis from the X-ray reflectivity (XRR) measurements. For the XAS analysis, a transfer vessel system has been strongly required to measure the anaerobic samples such as electrode compounds and organic/inorganic compounds which are easily degraded by oxygen in atmosphere. Hence, the transfer vessel system has been developed and installed into the XAS station in BL10. In the present article, design concept and schematics of the system are briefly described.

## 2. Design of the transfer vessel system

The transfer vessel system was designed, based on the following concept;

- (1) The usual large-size sample plate ( $75 \text{ mm}^L \times 25 \text{ mm}^W$ ) can be transferred from a glovebox to the preparation chamber of the XAS station.
- (2) Size of the vessel should be smaller than  $300 \times 200 \times 200 \text{ mm}^3$  to be used in a popular glovebox.

To satisfy the above conditions, the system was designed as shown in Figure 1. The main body of the transfer vessel is a cylinder pipe sealed with an ICF70φ flanges with O-rings. One flange is a manual gate valve and another has a compact pressure gauge and a small leak valve for gas-inlet/outlet. Sample plate is put on a transfer holder in the vessel. The vessel is connected to the preparation chamber through the manual gate valve. Size of the vessel is smaller than  $300 \times 200 \times 200 \text{ mm}^3$ . A transfer vessel rod is connected to the

preparation chamber at the counter position of the transfer vessel. The transfer vessel rod can hold the transfer holder with a M4 screw, and pull out the holder with sample plate from the vessel. The sample bank in the preparation chamber was improved; A sample bed for the transfer holder is added to the bottom of sample bank. The sample-plate on a sample holder can be put on the additional sample bed. From the sample bed, only the sample plate can be held by M3 screw and be pull out by the main sample transfer rod.

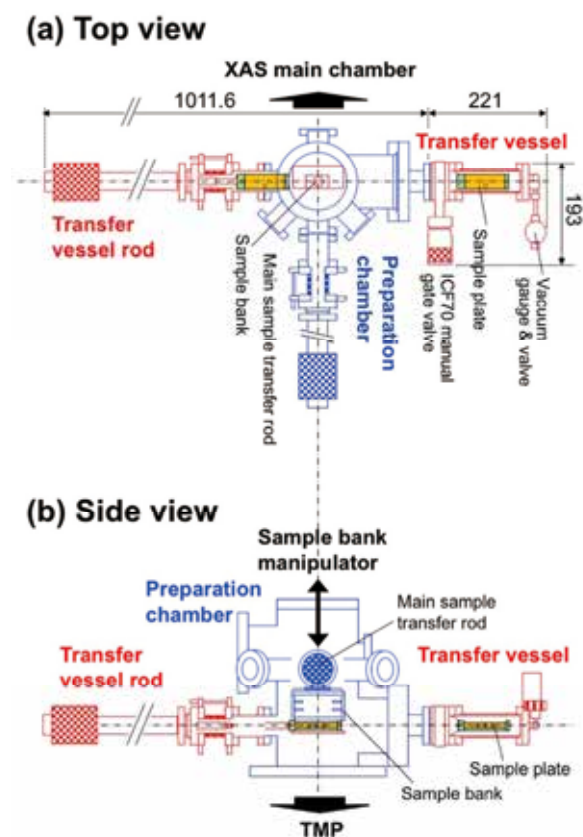


Fig. 1 Schematics of the transfer vessel system

connected to the preparation chamber.

### 3. Transfer vessel system

Figure 2 shows the transfer vessel and the XAS station employed the transfer vessel system. The main body of the transfer vessel is made from acrylic resin (polymethyl-2-methylpropenoate) cylinder pipe. This enables to easily observe inside the vessel and to be compact without additional view ports.

Transfer of the anaerobic sample can be performed with the following steps;

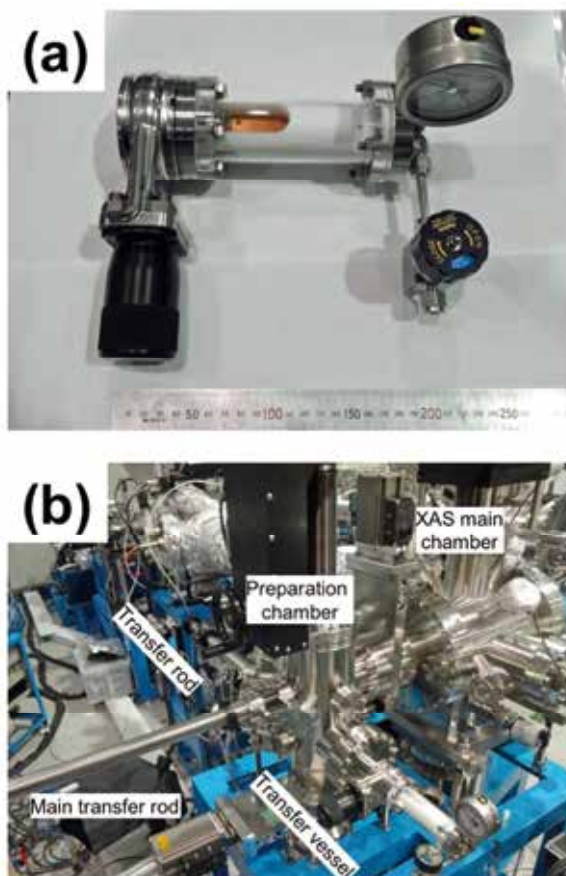
- (1) The transfer vessel involving a sample-plate/holder in inert gas atmosphere is connected to the preparation chamber.
- (2) The preparation chamber is pumped with a roughing pump and a turbo molecular pump (TMP). On the pumping by TMP, the manual gate valve of the vessel is opened and the vessel is pumped.
- (3) Sample-plate/holder is pulled out from the vessel by the transfer rod. Then, it is put on a sample bed in the preparation chamber.
- (4) Only sample-plate is pulled out from the bed by a main sample transfer rod, and transferred to XAS main chamber.

The transfer vessel system will be open to users in the period of 2017B.

**Fig. 2** Photos of a transfer vessel (a) and the transfer vessel system installed in the XAS station in BL10.

### References

- [1] Y. Muramatsu, A. Tsueda, T. Harada, and H. Kinoshita, *Adv. X-ray Chem. Anal., Japan*, 43, 407-414 (2012).
- [2] Y. Muramatsu, A. Tsueda, T. Uemura, T. Harada, and H. Kinoshita, *Adv. X-ray Chem. Anal., Japan*, 44, 243-251 (2013).
- [3] T. Uemura, Y. Muramatsu, K. Nambu, T. Harada, and H. Kinoshita, *Adv. X-ray Chem. Anal., Japan*, 45, 269-278 (2014).
- [4] T. Uemura, Y. Muramatsu, K. Nambu, D. Fukuyama, M. Kuki, T. Harada, T. Watanabe, and H. Kinoshita, *Adv. X-ray Chem. Anal., Japan*, 46, 317-325 (2015).



# Large area patterning using a new deep x-ray lithography system (BL11)

Masaya Takeuchi<sup>1</sup>, Akinobu Yamaguchi<sup>1</sup>, Yuichi Utsumi<sup>1</sup>  
(Univ.Hyogo<sup>1</sup>)

## Abstract

We developed a new deep x-ray lithography system (BL11) that fabricates high three-dimensional microstructure with high aspect ratio at “NewSUBARU” synchrotron radiation facility. In this study, we considered the beam scanning method that expose sample with uniform intensity distribution in large patterning area and evaluated the processing characteristics of resist (PMMA). As a result, uniform processing depth of the deviation of a few percent was obtained.

## Introduction

There have been rapid developments in the application of microsystems in advanced industries such as intelligent information systems, energy and environment conservations, and medical and biochemical services. Microsystems typically consist of different types of minute part for various applications. The realization of three-dimensional (3D) microstructures integrating multiple functions, such as electrical, optical, mechanical, and chemical functions in a restricted space, will bring many advantages to the industrial applicability of such microsystems. Additionally, demand for microfabrication with high aspect ratio and high accuracy has been increasing recently. To realize this requisition, the lithography, galvanofomung and abfomung process (LIGA process), which consists of deep-X-ray lithography (DXL), electroforming, and molding, is a promising candidate [1]. The LIGA process starts from the fabrication of high-aspect-ratio polymer microstructures with heights greater than a few hundred microns using DXL of a photosensitive polymer (resist) [2]. In the next step, a metal replica structure is formed by electroforming using the fabricated polymer microstructures as a master. The obtained metal replica structure can be used as a component in a microsystem or as a mold insert for final molding processes, such as hot embossing and injection molding. The aspect ratio of microstructures are decided at the X-ray lithography step.

In this paper, we developed a new DXL system that enables a large area processing and generates with high parallelism (0.1 mrad) and high photon flux (1.7 kW/cm<sup>2</sup>). Using this system, we investigated the processing characteristics of resist, and proposed the beam scan method that exposes a large patterning area with uniform intensity distribution on sample's surface.

## Constitution of this system

Fig.1 shows a schematic diagram of the lithography system. This system consists of SR beamline with x-ray optics and an exposure apparatus with six-axis motion stages. The beamline leads a SR beam from an electron storage ring to an end station for exposure. The SR beam propagates with enlarging horizontal intensity distribution of the cross section and inserts to a toroidal mirror (Pt coating on single crystal Si substrate). The x-ray beam collimated by the mirror goes through two Be filters (300 μm and 125 μm thickness) for cutting photon energy below 2 keV and reaches the exposure apparatus. Fig.2 shows calculated SR spectrum at exposure stage when the storage ring energy is 1.0 GeV and 1.5 GeV operation respectively where the storage ring current is 300 mA. These operation mode is selected depending on required line width, shape, processing depth, accuracy and throughput. Also, by using ray tracing program SHADOW, the x-ray beam shape at the exposure stage was calculated as shown in Fig.3. As a result, we confirmed that the intensity distribution was non-uniform arc shape at the cross section. This shows that the SR dose distribution is non-uniform when the x-ray beam simply scans the sample in the horizontal and vertical direction.

## Large area patterning

To solve above problem, we propose the scanning method that combines 2-dimensional shift of sample in the Y-axis and X-axis direction (Fig.4). we have attempted large area microfabrication by using this method with pitch = 1 mm for 1.5 GeV operation. Ploymethyl methacrylate (PMMA) was used as photosensitive material. Also, GG developer (60 vol% dieyhylene glycol, 20 vol% morpholin, 15 vol% pure water, 5 vol% ethanolamine) was utilized as developer and the development

condition was dip for 24 hours. Fig.5 shows the experimental result. The average processing depth was  $323\ \mu\text{m}$ , and the deviations were below 1 % respectively. In this way, we have succeeded obtaining uniform processing depth in large patterning area of  $8.5\ \text{cm} \times 10\ \text{cm}$ .

### Conclusion

The needs of 3D microstructure shifts for the fabrication of the line width of dozen of microns with high precision and high aspect ratio in various industrial fields. We have developed a deep x-ray lithography system that generates x-ray beam with high intensity and high parallelism in the universal energy range from 2 keV to 7 keV. Additionally, we have considered the beam scanning method realizing uniform large area processing. As a result of patterning using stainless steel mask, we have obtained the pattern with uniform processing depth of the maximum deviation of below 1 %. By utilizing this system, large area 3D microstructure can be obtained with high aspect ratio and uniform processing depth. It is expected that this x-ray lithography system will offer some advantages in the industrial applicability of LIGA process in the near future.

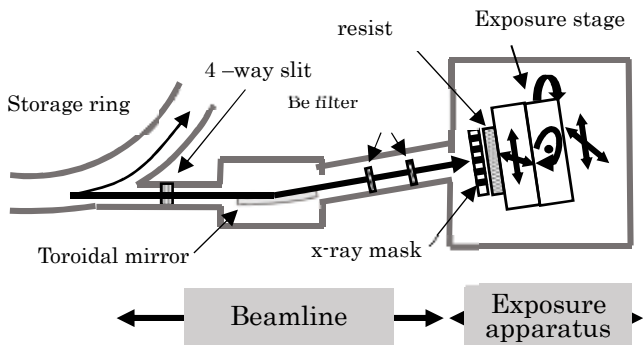


Fig.1 Schematic diagram of this lithography system

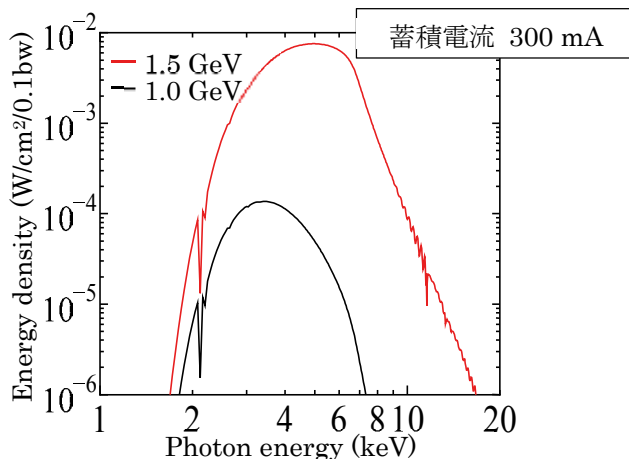


Fig.2 Calculated SR spectrum at exposure stage for BL11

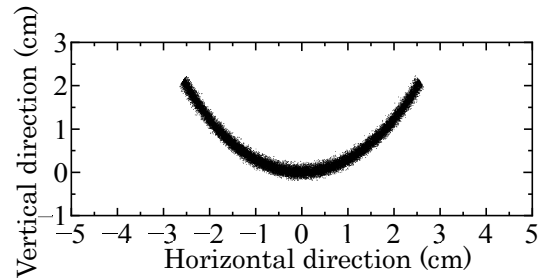


Fig.3 Calculated intensity distribution at exposure stage

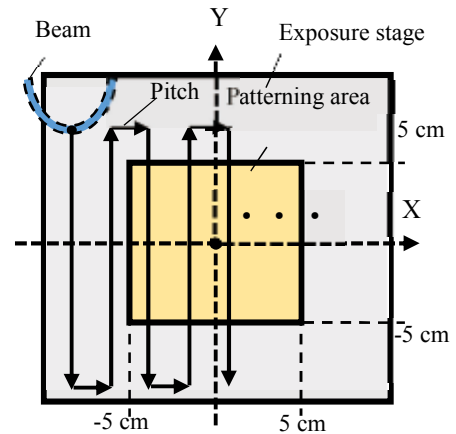


Fig.4 Scanning method

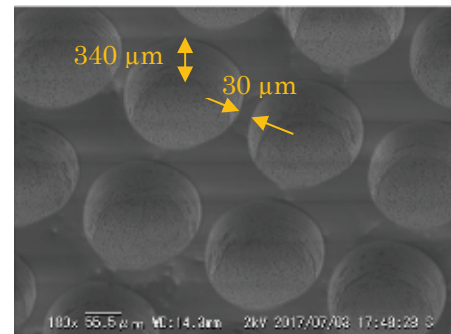


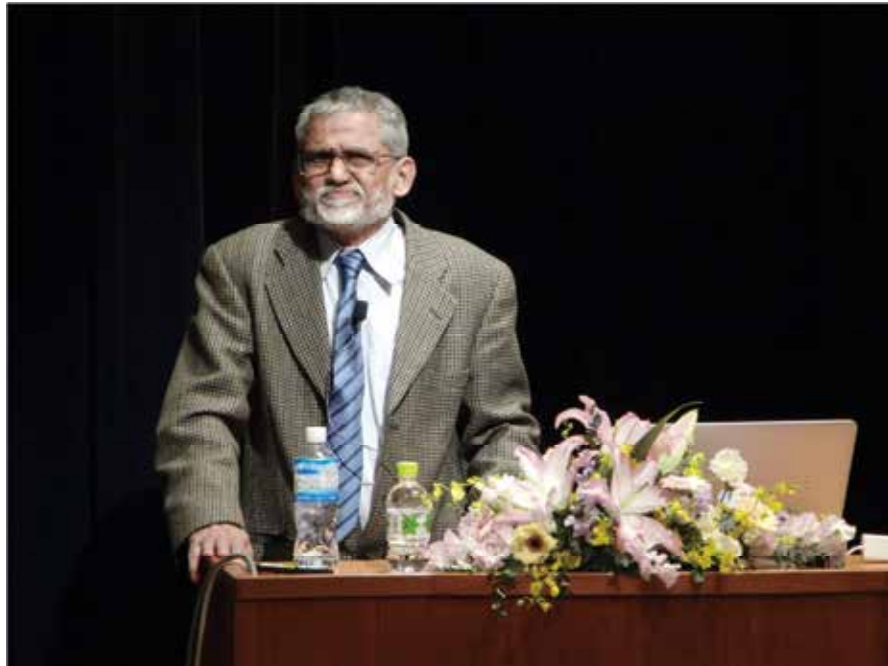
Fig.5 Fabricated pattern for 1.5 GeV operation

### References

- [1] E. W. Becker, W. Ehrfeld, P. Hagmann, A. Maner, and D. Munchmeyer, *Microelectron. Eng.* **4**, 35 (1986).
- [2] F. J. Panterbung, S. Achenbach, and S. Mohr, *Microsystems Tech.* **4**, (1998).



## **Part 2. Research Activities**



Invited talk of Prof. Chary Rangacharyulu  
at Advanced Technology Seminar 2017



# Upgrade plan toward the higher-brightness radiation source, NewSUBARU-2.0

Satoshi HASHIMOTO  
LASTI, University of Hyogo

## Abstract

We have started to study the upgrade plans for the NewSUBARU storage ring. The “NewSUBARU-2.0” ring will have the lower electron beam emittance and generate the higher-brightness radiation than the current ring. In this paper, the current status of the design study is reported.

## Introduction

NewSUBARU synchrotron radiation facility [1,2] has been operated for nearly 20 years. At NewSUBARU, soft X-ray, EUV light and gamma-ray by Compton scattering have been used for mainly industrial applications.

The general layout of the NewSUBARU storage ring is shown in Fig. 1. The ring has two long and two short straight sections for insertion devices. In one of two long straight sections, 10.8 m long undulator (LU) has been installed and the other is for the gamma-ray generation by the Compton scattering. In one of the short straight sections, the short undulator (SU) is equipped.

The ring is composed from six unit arrangements of electromagnets called “cell”. Fig. 2 shows one cell composed from two 34 degrees bending magnets (BMs) and one -8 degrees inverse bending magnet (BI). Horizontal and vertical beta functions and horizontal dispersion function are shown in Fig. 3. 1.0 GeV Electron beams are injected from SPring-8 Linac to the NewSUBARU ring. The stored energy can be changed from 0.5 to 1.5 GeV. The natural emittance is 37 nm-rad at 1.0 GeV.

One of the possible upgrade plans of the storage ring is the lower-emittance ring, which can generate the higher-brightness radiation. It is important for our facility to keep research activities high for next two decades. In considering upgrade designs we assumed that the present building and shield tunnel are reused as much as possible. Thus the circumference of the new ring must be almost same as the current value (118m). The interesting problem is how low the emittance can be possible at the small and relatively low-energy ring. In simulation works, tools like MADX[3], Bmad[4], elegant[5] are used. In this paper, we wish to report the current status of the design studies of the future upgrade plans for the NewSUBARU ring. Here we call it “NewSUBARU-2.0”.

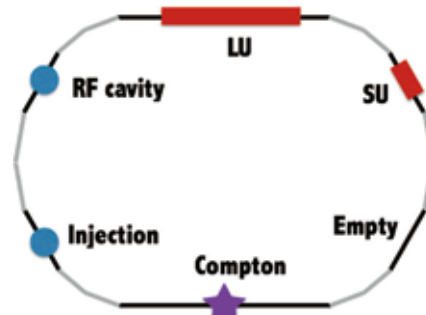


Fig.1 Layout of the current NewSUBARU storage ring.

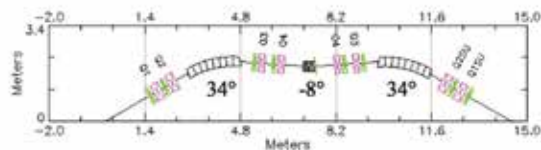


Fig.2 Geometrical plot of magnets in NewSUBARU per cell, which is composed from two 34 deg. bending magnets (BMs) and one inverse bending magnet (BI).

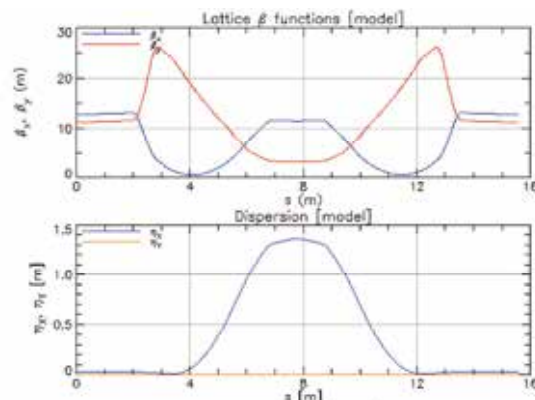


Fig. 3 Lattice functions of one cell of the NewSUBARU ring. Horizontal and vertical beta functions (upper) and horizontal dispersion (lower).

## Low emittance lattices

The natural emittance  $\epsilon_{x0}$  of an electron

beam in a storage ring is described in the following simplified form [6],

$$\varepsilon_{x0}[\text{nm}\cdot\text{rad}] = 1470 \frac{(E[\text{GeV}])^2}{J_x} \frac{\Phi^3 F}{12\sqrt{15}}$$

where  $J_x$  horizontal damping partition,  $\Phi$  deflection angle per bend,  $F$  factor depending on the lattice type.

In NewSUBARU-2.0, keeping the bending angle per cell 60 degrees, that is the same as the current ring, we searched optimum solutions in TBA and QBA lattice types.

In the case of TBA (Triple Bend Achromat) lattice, a cell is composed from three 20 degrees BMs as shown in Fig. 4. These BMs are combined-types, i.e., have horizontally defocusing quadrupole fields, and slightly increase  $J_x$  (~1.2). Optimizing lattice functions by adjusting four quadrupole families Q1~Q4, the minimum emittance is 5.5 nm-rad at 1.0 GeV.

In the case of QBA (Quadruple Bend Achromat), where four 15 degrees BMs are used per cell, the minimum emittance is 2.2 nm-rad. The MBA (Multi Bend Achromat) whose number of BMs is more than four is difficult because of limited path length.

As a result, the emittance of 2.2~5.5 nm-rad, that is about one order smaller than the current value, may be possible.

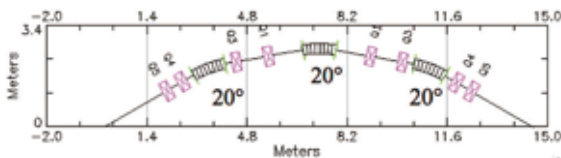


Fig. 4 Geometrical plot of Triple Bend Achromat cell.

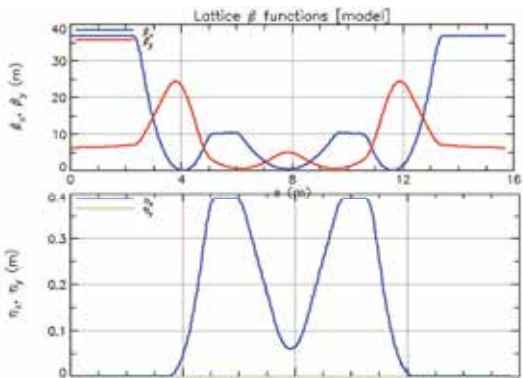


Fig. 5 Lattice functions of TBA: horizontal and vertical beta functions (upper) and horizontal dispersion (lower)

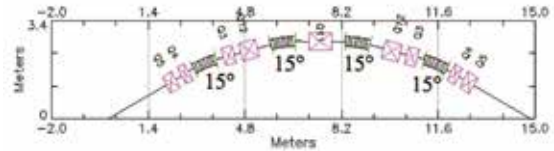


Fig. 6 Geometrical plot of Quadruple Bend Achromat cell.

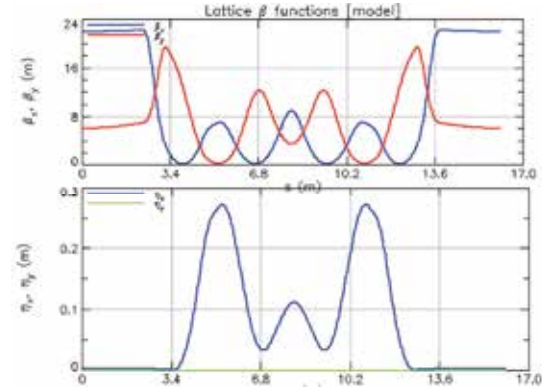


Fig. 7 Lattice functions of QBA: horizontal and vertical beta functions (upper) and horizontal dispersion (lower)

### Synchrotron radiation from bending magnets and wigglers

The critical photon energies at 1.0 and 1.5 GeV of NewSUBARU are 0.69 and 2.3 keV, respectively. Some users using X-ray as micro-fabrication tools prefer higher-energy photons and the operation at 1.5 GeV. Thus about 40% of the user-time is operated at 1.5 GeV, and the remaining is 1.0 GeV. The situation would be the same in the case of NewSUBARU-2.0. However, the increased beam energy makes emittance worse, because of its energy dependence.

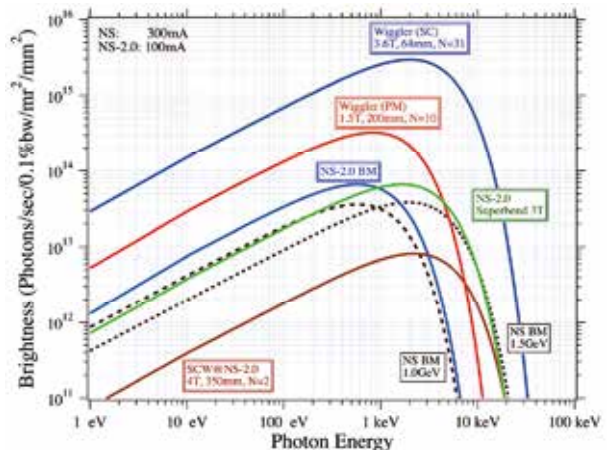


Fig. 8 Brightness of synchrotron radiation from bends and wigglers. Dotted lines are bending radiation of NewSUBARU at 1.0 and 1.5 GeV. The stored beam energy of NewSUBARU-2.0 is 1.0 GeV.

Multi-pole damping wiggler in a short straight section is one of solutions for this problem. If the parameters are well defined, such device can decrease emittance and also generate the higher-energy photons than BM. Emittance is determined in the balance between radiation damping and radiation excitation,

$$\frac{\varepsilon_W}{\varepsilon_0} = \frac{1 + I_5^W / I_5^0}{1 + I_2^W / I_2^0}, \quad \frac{\sigma_{\varepsilon W}^2}{\sigma_{\varepsilon 0}^2} = \frac{1 + I_3^W / I_3^0}{1 + I_2^W / I_2^0},$$

where  $I_2, I_3, I_5$  are radiation integrals [6] and the indices  $^0$  and  $^W$  indicate that the integral be taken over bending magnets and wiggler magnets separately.  $\sigma$  denotes horizontal beam size.

Using typical wiggler parameters shown in Table 1, brightness curves are plotted in Fig. 8. As shown in this figure the radiation intensity from multi-pole wiggler at 1.0 GeV is sufficiently replaced to BM light at 1.5 GeV with damping effect.

Table 1 Typical wiggler parameters

	Wiggler #1	Wiggler #2	Wiggler #3
Magnet type	SC	PM	SC
$\square w$ [T]	4.0	1.5	3.6
$\lambda w$ [mm]	350	200	64
Nw	2	10	31
L [m]	0.7	2.0	1.984
$\varepsilon w / \varepsilon 0$	1.19	0.91	0.64
$\sigma \square w / \sigma \square 0$	1.21	1.01	1.31

**Brightness of Long Undulator**

One of the big features of NewSUBARU is the 10.8m long undulator (LU), which is very long compared to the total circumference of 118m. Fig. 9 shows brightness of LU in both NewSUBARU and NewSUBARU-2.0. Because of the low emittance electron beam, LU brightness in NewSUBARU-2.0 is several-times larger than the present ring, if the stored current is the same value. In addition to the present LU, the installation of the second long undulator (LU2) in another straight section is most attractive in NewSUBARU-2.0 for users.

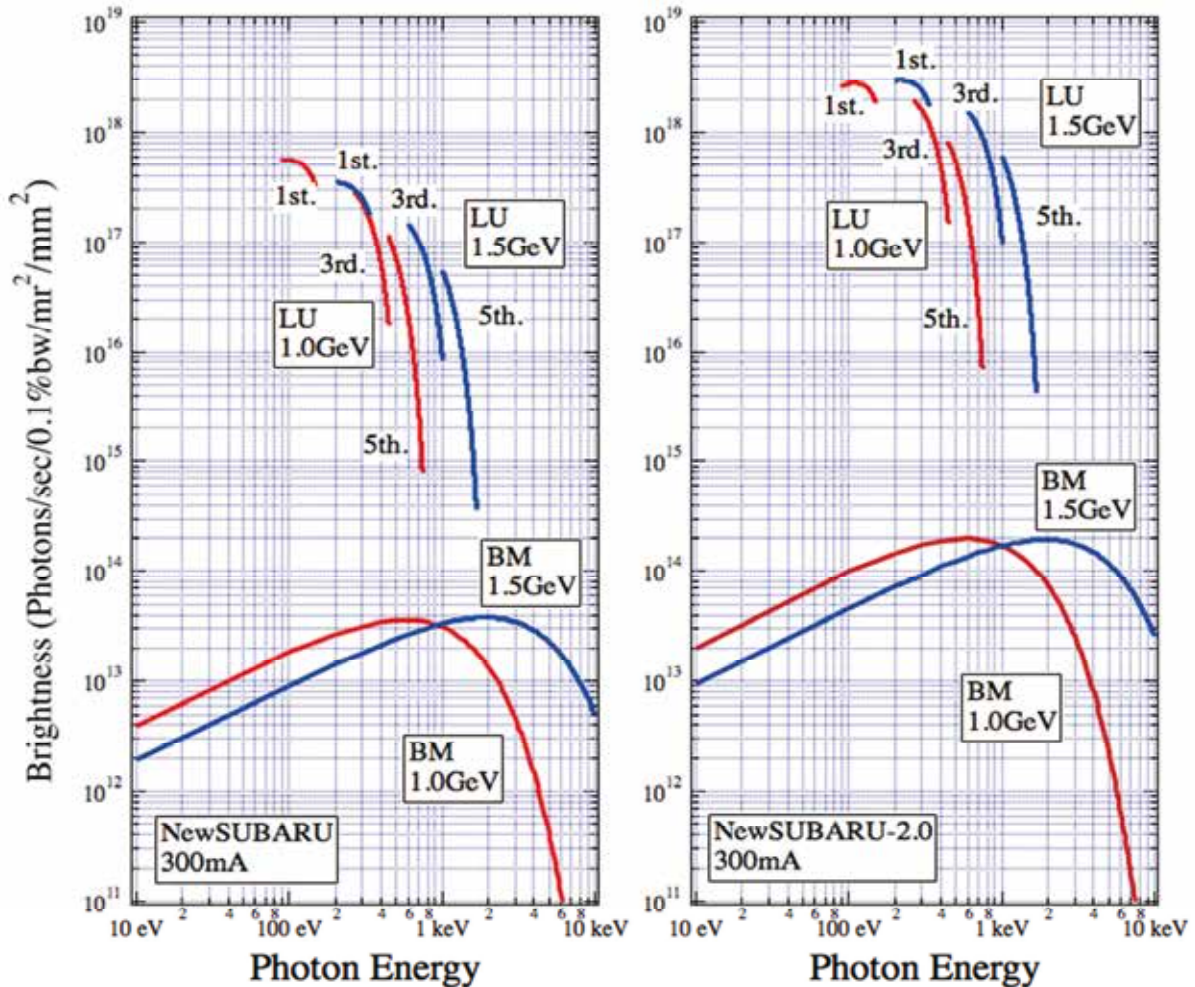


Fig. 9 Brightness of LU radiation in NewSUBARU (left) and NewSUBARU-2.0 (right).

### Phase Enhanced Harmonic Generation of the high-power EUV light

The alternative use of the long straight section is the Phase Enhanced Harmonic Generation (PEHG), which was proposed to generate a high-power coherent radiation by making micro-bunches in an electron beam [7]. The high-power (~KW) radiation source by PEHG for EUV Lithography was proposed [8]. The possibility of PEHG in NewSSUBARU-2.0 for EUVL light source is reported in the other paper of this annual report [9].

### Compton Scattering Gamma-ray generation

Gamma-ray generation by Compton scattering and its application has been an important research field in NewSUBARU and the situation will be the same in NewSUBARU-2.0.

For the effective collisions between laser photons and electrons, the overlap factor should be close to unity, i.e., the photon beam waist size should be equal to the electron beam size at the center of straight section. However, in NewSUBARU, the distance from a laser source and the collision point in long straight section is too long to efficiently focus laser beam. Moving the Compton beam-line from the current position to one of the short straight section may be advantageous in the NewSUBARU-2.0 ring.

### Summary

For the upgrade of the NewSUBARU ring, we have just started design study of the low-emittance and high-brightness radiation source, NewSUBARU-2.0. The estimated emittance is under 10 nm-rad. And we also evaluated the usage of straight sections for insertion devices. We would like to propose that two short straight sections are used for current short undulator or wiggler, and for Compton gamma-ray. And also one of two long straight sections is used for the current Long Undulator. The other long straight section can be used for another Long Undulator (LU2) as shown in Fig. 10 (left). The alternative usage is for both a middle long undulator (MU) and PEHG for EUVL light source as shown in Fig. 10 (right). Table 2 shows main parameters of NewSUBARU and NewSUBARU-2.0 rings.

This is only the first step towards the future upgrade in the accelerator researcher's point of view. Dynamic aperture, tune survey, chromatic correction, Intra-Beam Scattering, etc. are in under work. It should be also mentioned

that many changes according to user's opinions would be included in the future draft.

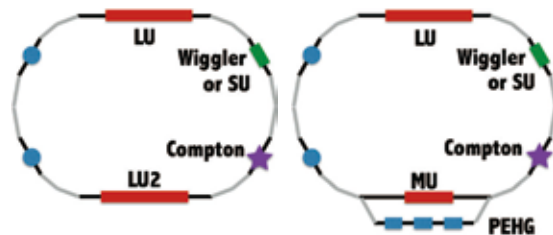


Fig. 10 Proposed layouts of NewSUBARU-2.0. "LU2" and "MU" denote "2<sup>nd</sup> Long Undulator" and "Middle long Undulator", respectively.

Table 2 Typical parameters of NewSUBARU and NewSUBARU-2.0 rings

	NS	NS-2.0
Circumference [m]	118	~118
Beam energy [GeV]	0.5-1.5	0.5-1.5
Beam current [mA]	500 (max.)	<500
	350 (top-up)	<300
Insertion devices	LU	LU
	Compton	LU2 or
	SU	PEHG+MU
		MPW/SU
		Compton
Emittance [nm]	37	5.5 (TBA)
		2.2 (QBA)

### Acknowledgements

Thanks are due to Prof. S.Miyamoto of LASTI, University of Hyogo, and my many colleagues of NewSUBARU accelerator group (JASRI/SES), Dr.Y.Minagawa, Mr. K.Kajimoto, Mr. K.Morisato, and Mr. H.Takeuchi.

### References

- [1] A.Ando et al., J. Synchrotron Rad., 5, 342-344 (1998)
- [2] <http://www.lasti.u-hyogo.ac.jp/NS-en>
- [3] <http://mad.web.cern.ch/mad/>
- [4] <https://wiki.classe.cornell.edu/ACC/ACL/OffsiteDoc>
- [5] M. Borland, "elegant: A Flexible aSDDS-Compliant Code for Accelerator Simulation", Advanced Photon Source LS-287, September 2000.
- [6] Handbook of Accelerator Physics and Engineering, Wu.Chao, M.Tigner
- [7] Chao Feng, "Theoretical and Experimental Studies on Novel High-Gain Seeded Free-Electron Laser Schemes", Springer Theses
- [8] Chao Feng et al., "Storage ring based EHG FEL for EUV lithography", High-Brightness Sources and Light-Driven Interactions (EUV, HILAS, MICS) © 2016 OSA
- [9] S.Hashimoto et al., "Possibility of High-power EUV light by PEHG scheme at NewSUBARU-2.0", in this Annual Report

# Possibility of High-power EUV light by PEHG scheme at NewSUBARU-2.0

Satoshi HASHIMOTO and Shuji MIYAMOTO  
LASTI, Univ. of Hyogo

## Abstract

For the generation of coherent high-power radiations, many schemes based on accelerator and Free Electron Laser (FEL) technologies have been proposed [1]. Phase-Enhanced Harmonic Generation (PEHG) is one of these schemes and a high-power EUV light source for lithography using the PEHG at a storage ring was theoretically proposed [2]. We evaluated the possibility of our storage ring as a high-power EUVL source in the case of the future upgrade plan “NewSUBARU-2.0”.

## Introduction

The lower-emittance electron storage ring generates the higher-brightness radiation, for which many users are eager. As a future upgrade plan of the NewSUBARU storage ring [3,4], we have been performing design studies of the lower-emittance ring “NewSUBARU-2.0”. As a result of early simulation studies [5], the natural emittance of the NewSUBARU-2.0 ring is under 10 nm-rad.

As for insertion devices, one of the two long straight sections in NewSUBARU-2.0 should be used for the current 10.8 m Long Undulator (LU) as it is now. In the other long straight section, installing the second Long Undulator seems to be very attractive for radiation users. On the other hand, another candidate of how to use this section is the R&D for the generation of the high-power EUV radiation by the PEHG scheme. A general layout of the proposed NewSUBARU-2.0 ring is shown in Fig. 1 [5].

## Phase-Enhanced Harmonic Generation

A high-power coherent radiation can be generated from an electron beam that is bunched or density modulated in radiation wavelength. How to make micro-bunch effectively is a key issue and many methods have been proposed and studied [1].

The PEHG scheme is illustrated in Fig. 2. After the trajectory of an electron beam is horizontally shifted by dogleg-1, electrons are

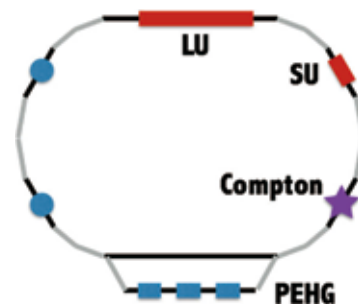


Fig. 1 General layout of insertion devices for the NewSUBARU-2.0 ring,

ordered horizontally according to its energy. A seed laser in visible range and an undulator (modulator) give electrons an energy modulation. Transverse Gradient Undulator (TGU), where K parameter varies according to the horizontal coordinate, gives electrons “merge” in its longitudinal phase-space. At chicane magnets, the energy modulation is converted to the density modulation by the dependence of electron’s path length on its energy. The bunching factor at the entrance of an undulator (radiator) includes relatively higher harmonics of the seed laser wavelength. In the radiator, electron beams coherently radiate at harmonics of the laser wavelength.

## Typical PEHG parameters at NewSUBARU-2.0

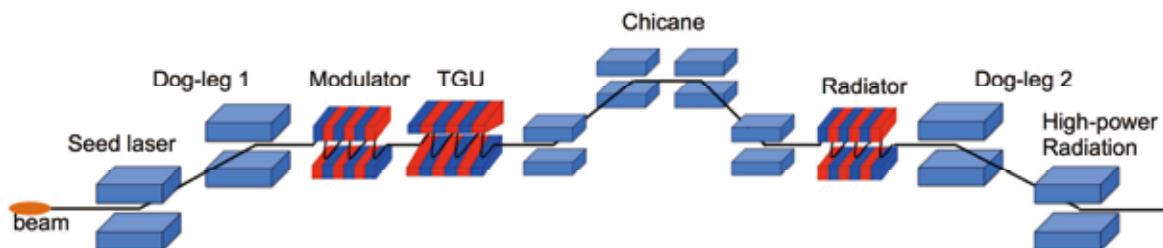


Fig.2 Layout of the Phase-Enhanced Harmonic Generation (PEHG) scheme.

At first, we examined the PEHG scheme using the current NewSUBARU ring parameter. However, it found to be difficult to sufficiently full-fill the PEHG conditions because of too large emittance and beam size in horizontal. Thus we simulated the PEHG bunching process in the longitudinal phase-space in the case of NewSUBARU-2.0 with smaller emittance and beam size than the present ring.

Typical parameters of each component of the PEHG scheme are listed in Table. 1. A seed laser of wavelength 270 nm is used. Its 20<sup>th</sup> harmonics corresponds to 13.5 nm needed for EUVL. Fig. 3 shows the bunching factor at the entrance of the radiator, where the bunching factor of the 20<sup>th</sup> harmonics is about 0.09.

Table. I Typical parameters of PEHG the in NewSUBARU-2.0 ring

----- Seed laser -----	
wavelength [nm]	270.0
harmonic number	20
power [MW]	100.0
Rayleigh length [m]	0.760
waist size [mm]	0.256
radius [mm]	0.286
area [cm <sup>2</sup> ]	1.28E-03
power density [W/cm <sup>2</sup> ]	7.80E+10
E-field strength [V/m]	7.65E+08
normalized vector potential	6.43E-05
----- Electrons -----	
average energy in gamma	1957.0
energy spread in gamma	0.780
initial Hor. rms beam size [mm]	0.050
----- Dogleg1 -----	
dispersion [m]	0.600
D, dimensionless dispersion	4.783
Hor. beam size with dispersion [mm]	0.244
----- Modulator -----	
K parameter	1.800
total length [m]	2.700
normarilzed vector potential	1.273
maximal modulation depth (in gamma)	2.165
A, maximal modulation amplitude	2.776
----- TGU -----	
K0	1.80
gradient Alpha [1/m]	56.00
T parameter of TGU	0.074
----- Chicane -----	
R56, the strength of the chicane	-4.00E-05
B parameter	-0.371

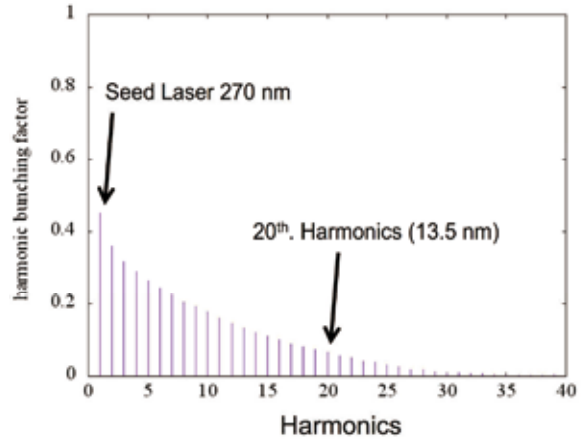


Fig.3 Harmonic bunching factor at the radiator.

### Summary

We studied the possibility of the high-gain seeded FEL scheme called PEHG for the high-power EUV source for lithography in the case of the NewSUBARU-2.0, the future upgrade plan. Relatively large bunching factor at the higher harmonics can be achieved. The high-power EUV source using the PEHG can be promising and one of attractive options in the future NewSUBARU-2.0. Design studies on the PEHG in NewSUBARU-2.0 in more detail are in progress.

### References

- [1] Chao Feng, "Theoretical and Experimental Studies on Novel High-Gain Seeded Free-Electron Laser Schemes", Springer Theses
- [2] Chao Feng et al., "Storage ring based EHG FEL for EUV lithography", High-Brightness Sources and Light-Driven Interactions (EUV, HILAS, MICS) © 2016 OSA
- [3] A.Ando et al., J. Synchrotron Rad., **5**, 342-344 (1998)
- [4] <http://www.lasti.u-hyogo.ac.jp/NS-en>
- [5] S.Hashimoto, "Upgrade plan toward the higher-brightness radiation source, NewSUBARU-2.0", in this Annual Report

# Test of a gamma-ray diamond detector

A. Martens<sup>1</sup>, T. Williams<sup>1</sup>, S. Amano<sup>3</sup>, K. Cassou<sup>1</sup>, K. Dupraz<sup>1</sup>, E. Griesmayer<sup>2</sup>, S. Hashimoto<sup>3</sup>, P. Kavrigin<sup>2</sup>, S. Miyamoto<sup>3</sup>, C. Ndiaye, A. Takemoto<sup>3</sup>, M. Yamaguchi<sup>3</sup>, F. Zomer<sup>1</sup>

<sup>1</sup>*LAL, Univ Paris-Sud, CNRS/IN2P3, Université Paris-Saclay, Orsay, France  
martens@lal.in2p3.fr*

<sup>2</sup>*Vienna University of Technology, Austria,*

<sup>3</sup>*Laboratory of Advanced Science and Technology for Industry, University of Hyogo, Kouto, Hyogo, Japan.*

## Abstract

A 4-quadrant sCVD diamond sensor was installed and tested at NewSUBARU BL01 in June 2016. Preliminary results are described here. They give confidence that such a radiation hard, fast and hardly destructive sensor is extremely useful for gamma beam monitoring, in particular at ELI-NP-GBS.

## Introduction

The Extreme Light Infrastructure Nuclear Physics Gamma Beam System (ELI-NP GBS) [1] is a novel source of photons with unprecedented spectral density, under construction in Magurele Romania. Photons in the range 200keV to 20MeV will be produced by Compton scattering off electrons. A new optical system is implemented in order to reach a spectral density greater than 5000 photons/(s eV). The sub-picosecond synchronization and alignment within a few micrometers of this apparatus require a thorough optimization procedure with dedicated optical tools described in Ref. [2]. The individual time separation between each of the 32 successive collisions is approximately 16 ns. A fast monitoring tool capable of distinguishing 16 ns spaced bunches of gamma-rays produced by this system would be beneficial to confirm the bunch to bunch performance and the final optimization of the setup. The ability to evaluate the transverse shape of the beam would be an additional asset for such a detector, indeed the photon beam polarization is expected to be given by the laser-beam polarization, provided that on-axis photons are selected and that smearing due to the finite size and emittance of the beams is negligible [3].

Diamond sensors are known to be fast and radiation hard detectors which make them better candidates to accomplish the above mentioned task with respect to the more usual (in the nuclear physics community) solution consisting of using scintillating detectors [4, 5, 6]. They are also used in the X-ray community with, among others, excellence performance as an alignment tool [7]. A first experiment with bunched gamma-beams was conducted in 2015 at the HIGS facility, showing the ability of the detector to measure bunches separated by 16 ns

[8]. The roughly flat energy dependence of the response in the few MeV range was also checked but more precise measurement would be beneficial.

In order to further test the performance of a diamond sensor in the context of the online monitoring of gamma-beams, a new experiment was conducted in June 13 to 22, 2016 at NewSUBARU. Preliminary results of this experiment are reported

## Experimental setup

A 4-quadrant, 500  $\mu\text{m}$  thick, single-crystal chemical vapour deposited (sCVD) diamond sensor, provided by CIVIDEC Instrumentation GmbH [9], is placed in BL01 experimental hutch, at about 22 meters from the interaction point between the laser and the electron beams. Each quadrant of the sensor is a square with 1.5 mm sides and is read-out with C6 or C2 amplifiers from CIVIDEC Instrumentation GmbH, depending on the configuration of the experiment. Waveforms from each amplifier are digitalized synchronously thanks to a 8-channel wavecatcher board [10] and stored to a local computer for offline analysis. A dedicated system allowing to carefully mount tungsten foils 2 mm in front of the diamond sensor was used during the experiment to investigate the signal amplification introduced by the conversion of a significant part of the photons into electrons achieved by this high-Z material.

## Results

Several types of experiments were conducted. Linearity tests of the sensor were performed by means of varying the laser-beam power (see Figure 1) and the laser-beam Q-switch frequency. As expected, increasing the laser-beam power at a given Q-switch frequency, or decreasing the Q-switch frequency at a constant

average power, gives a rise in the yield of detected photons.

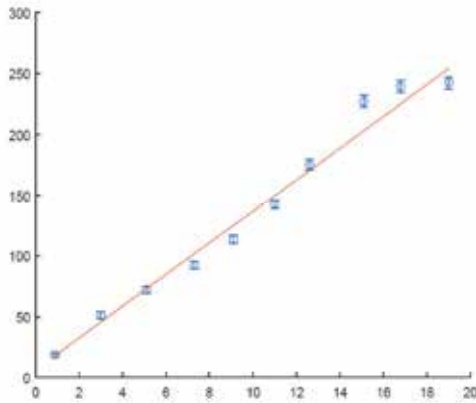
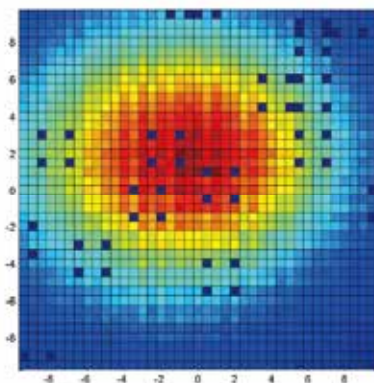


Figure 1: Number of detected gamma (arbitrary unit) versus laser-beam average power in Watts.

The use of a W-foil of about 0.5mm allowed to increase by a factor about 10 the detection efficiency of the setup. Detailed simulations are required to compare predictions with the obtained results. This work is still in progress.

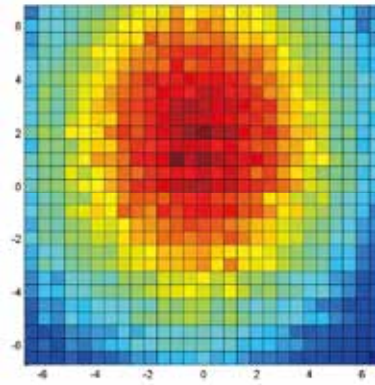
Transverse scans of the gamma beam allowed to measure the transverse shape of the gamma beam. Some preliminary results are shown in Figures 1 and 2. These results were obtained with two different configurations of polarization. The fact that the gamma-beam is not perfectly circular in the case of a circularly polarized laser-beam is related to the fact that electron beam sizes and emittance cannot be neglected in the case of NewSUBARU. These images are relatively free of background thanks to the fact that the sensor is not sensitive to photons below about 200 keV.

Detailed calculations taking into account all known parameters of the electron and laser beams are being held in order to extract the



laser-beam polarisation from the transverse shape of the gamma-beam. First results showed that a precision of about 0.05 on the Stokes

Figure 2: Signal yield in the diamond sensor as a function of its transverse position in the case of a circularly polarized laser-beam (preliminary). Dark dots correspond to missing measurement points due to some malfunction of the acquisition software.



parameters can be reached. If this exercise seem meaningless in the NewSUBARU setup, Figure 3: Similar as Figure 2 but with a linear polarization (preliminary).

because the laser-beam polarisation can be directly measured, it will not be the case bunch per bunch in ELI-NP-GBS due to the complexity of the optical system. Such an indirect measurement through the transverse shape of the gamma-beam may be proved useful to check the polarisation of the gamma beam.

## Conclusion

A 4-quadrant sCVD diamond sensor was successfully tested at NewSUBARU BL01 in June 2016. The results show that the expected performance is reached. They give confidence in the use of such type of sensor for a radiation hard, fast and hardly destructive monitoring of the gamma beam for the upcoming radiation sources, and in particular at ELI-NP-GBS.

## References

- [1] O.Adriani, *et al.*, arXiv:physics.acc-ph/1407.3669.
- [2] K. Dupraz, *et al.*, Phys. Rev. ST Accel. Beams **17**, 033501 (2014).
- [3] V. Litvinenko, *et al.*, Phys. Rev. Lett. **78** 4569 (1997).
- [4] Kölbl *et al.*, IEEE Trans. Nucl. Science **6** (2004).
- [5] W. Drozdowski, NSS MIC proceedings 2008.
- [6] Behnke *et al.*, Nucl. Inst. Methods A (2002)
- [7] Desjardins, J. Synchrotron Rad. **21**, 1217–1223 (2014).
- [8] T. Williams *et al.*, Nucl. Inst. Methods in Physics Research A **830** (2016) 391–396.
- [9] CIVIDEC Instrumentation GmbH, [www.cividec.at](http://www.cividec.at).
- [10] wavecatcher reference

# Test of Gamma-ray detector (LaBr<sub>3</sub>)

F. Camera<sup>1,2</sup>, G. Gosta<sup>1,2</sup>, N. Blasi<sup>2</sup>, B. Million<sup>2</sup>, A. Giaz<sup>2</sup>, O. Wieland<sup>2</sup>, F. M. Rossi<sup>1</sup>, H. Utsunomiya<sup>3</sup>, T. Ari-izumi<sup>3</sup>, D. Takenaka<sup>3</sup>, D. Filipescu<sup>4</sup>, I. Gheorghe<sup>4,5</sup>

<sup>1</sup> University of Milano, Department of Physics, Via Celoria 16, 20133 Milano, Italy

<sup>2</sup> INFN Section of Milano, Via Celoria 16, 20133 Milano, Italy

<sup>3</sup> Konan University, Department of Physics, Okamoto 8-9-1, Higashinada, Kobe 658-8501, Japan

<sup>4</sup> Extreme Light Infrastructure Nuclear Physics, "Horia Hulubei" National Institute for Physics and Nuclear Engineering (IFIN-HH), 30 Reactorului, 077125 Bucharest-Magurele, Romania

<sup>5</sup> Faculty of Physics, University of Bucharest, Bucharest, Romania

## Abstract

Intense beams of gamma-rays with energies ranging from 5 MeV to 38 MeV were used to illuminate two large volume (3.5" x 8") LaBr<sub>3</sub>:Ce detectors. The gamma-rays beams were produced in the NewSUBARU facility and the measurements were performed in the GACKO experimental hutch. The response function and the absolute detection efficiency of these two detectors have been measured making use, as a reference, of a very large volume NaI(Tl) (8" x 12") scintillator detector.

## Introduction

The response function and the absolute detection efficiency of LaBr<sub>3</sub>:Ce detectors are known in case of low-medium energy gamma-rays, see for example ref [1]. The response function and the efficiency values for gamma rays with energy higher than 10 MeV is in general extrapolated from the low energy values. At the moment, there are very few measurements [2,3] of the response function for gamma-rays up to 22 MeV and no direct measurement of the LaBr<sub>3</sub>:Ce response function and absolute detection efficiency for gamma rays with energies higher than 22 MeV.

In the case of large volume LaBr<sub>3</sub>:Ce (3.5" x 8") these measurements are even more important as only with high energy gamma-rays the full volume of the crystal will be used. In fact, to stop 661 or 1322 keV gamma rays only the first 5-10 cm of the detector are used, as gamma-rays do not penetrate deeply in the detector. Any GEANT4 extrapolation for high energy gamma rays, therefore, needs to be confirmed by experimental data.

## Experiments and Results

The measurements were performed in the GACKO experimental hutch [4] of the NewSUBARU synchrotron radiation facility located in the SPring8 site. The facility provides gamma beams using the Laser Compton Scattering (LCS) mechanism. A GEANT4 simulation shows that the resulting gamma beam is well collimated. The incident gamma-ray energy distributions were obtained by performing GEANT4 simulations of the response functions of the LaBr<sub>3</sub>:Ce detector to the LCS gamma-ray beam, involving the kinematics of LCS and collimation geometry. Fig. 1 shows the extracted incident beam energy spectra while Fig. 2 shows the LaBr<sub>3</sub>:Ce measured spectra. Table 1 summarizes the electron and the gamma-ray

energies used in the measurements. The gamma-ray energies correspond to the maximum values in the energy distributions.

Table 1. The maximum gamma beam energies and the NewSUBARU storage ring electron energies are listed in column one and two.

$E_\gamma$ [MeV]	$E_{e^-}$ [MeV]
5.53	550
6.04	575
9.00	704
13.00	849
14.99	914
16.93	974
20.99	1087
24.02	1162
29.02	1273
34.03	1380
38.00	1460

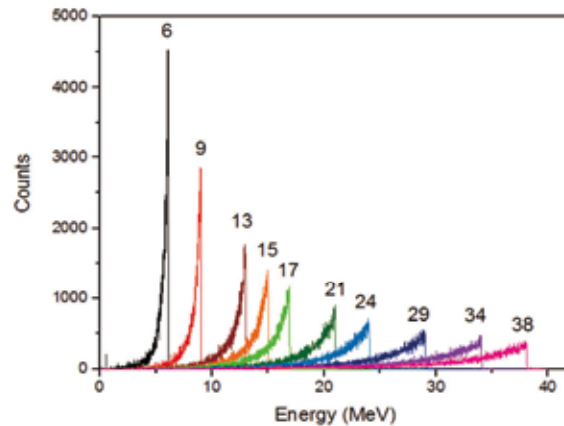


Figure 1: The incident gamma-ray energy spectra from GEANT4 simulations. The nominal beam energy, corresponding to the maximum energy of the gamma-rays, is indicated over the spectrum.

In the measurements, for each beam energy we have used two 3.5" x 8" crystals, each coupled to two PMTs in order to disentangle crystals and PMT's performances. The measurement of the detector response function and of its non-linearity was done using the laser beam in CW mode and using a 5cm Pb absorber to avoid multiple gamma rays in a single shot. For the measurement of the absolute detection efficiency we have used the laser beam in pulsed mode measuring the multi-phonon (MP) and single phonon (SP) spectra first with the NaI(Tl) and then with the two LaBr<sub>3</sub>:Ce detectors.

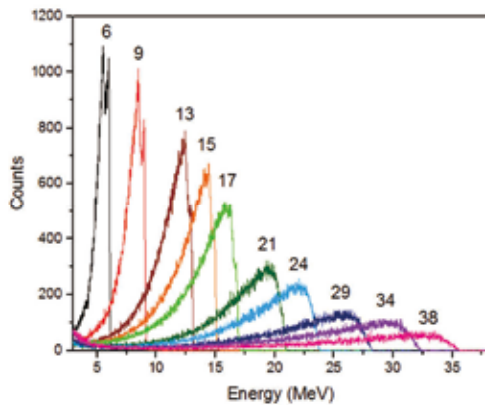


Figure 2: The LaBr<sub>3</sub>:Ce measured gamma-ray energy spectra. The maximum energy of the gamma-rays is indicated over each spectrum

The analysis of the response function of the two detectors is completed (see figure 3). We have found that i) the two crystals, having the same size, showed an identical behavior (within the error bars), ii) the PMTs showed a different degree of non-linearity which can be parameterized using a third order polynomial as shown in figure 4.

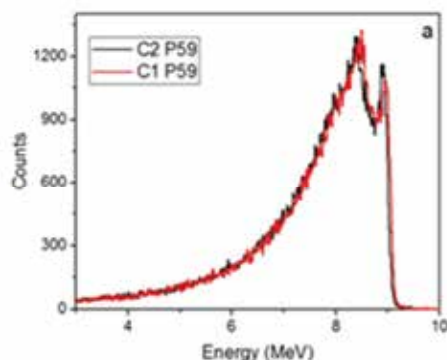


Figure 3: The measured response function of both crystals (C1 and C2 in the figure caption) coupled to PMT R10233 S/N ZE5559. The gamma-ray beam maximum energy was 9 MeV.

The analysis of the data for the determination of the absolute detection efficiency is not completed yet, as the first step consists in the

measurement of the PMTs non-linearity curves. Figure 5 and 6 show the multiple photon (MP) spectra (with and without beam) for the NaI(Tl) and one LaBr<sub>3</sub>:Ce detector (for gamma-rays of 9 MeV).

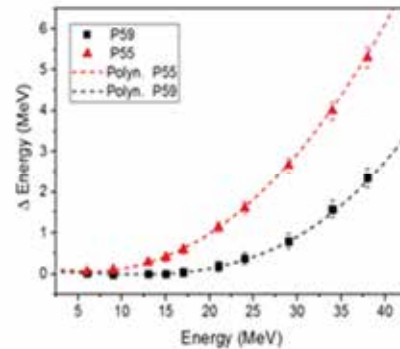


Figure 4: The non-linearity measured for the two used PMT (P55 in the figure caption indicate PMT R10233 S/N ZE5555 while P59 indicate PMT with S/N ZE5559). The filled points indicate the measured values, the dashed lines show third order polynomial curves which fitted the experimental points.

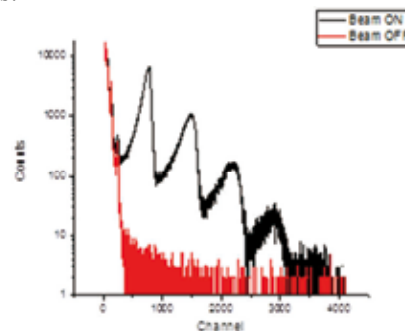


Figure 5. The NaI(Tl) measured MP (black with beam on, read for beam off) for the 9 MeV incident gamma energy.

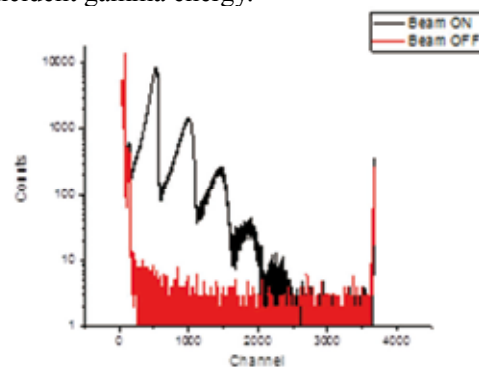


Figure 6. The LaBr<sub>3</sub>:Ce measured MP (black with beam on, read for beam off) for the 9 MeV incident gamma energy.

## References

- [1] A. Nicolini et al. NIM A582(2007)554.
- [2] M.Ciemala et al. NIMA608(2009)76
- [3] A.Giaz et al. NIMA 729(2013)910
- [4] H. Utsunomiya et al., NPN 25(2015)25.

# Improvement of Performance for XAFS Measurements in BL05A

T. Hasegawa<sup>1,2,3</sup>, S. Fukushima<sup>2,3</sup> and K. Kanda<sup>3</sup>

1 Synchrotron Analysis L.L.C., 3-2-24 Wadamiya-dori, Hyogo-ku, Kobe-shi, Hyogo 652-0863 Japan  
2 Kobe Material Testing Laboratory Co., Ltd., 47-13 Niijima, Harima-cho, Kako-gun, Hyogo 675-0155 Japan

3 LASTI, University of Hyogo, 3-1-2 Koto Kamigori-cho, Ako-gun, Hyogo 678-1205 Japan

## Abstract

A renewed double crystal monochromator (DCM) improved performance of BL05A for X-ray absorption fine structure (XAFS) measurements in the soft X-ray region. We were successful in increasing of photon intensity by replacing the beryllium filter (45  $\mu\text{m}$  thickness) with previous one (25  $\mu\text{m}$  thickness). In addition, we succeeded to obtain the sodium *K*-edge X-ray absorption near edge structure (XANES) spectra, which enabled practical analysis in the X-ray region about 1keV.

## Introduction

In the soft X-ray region around 1keV, X-ray absorption fine structure (XAFS) spectroscopy is important to industry because there are *K* absorption edges of elements: sodium, magnesium, aluminum and so on, in this energy region. Due to these elements are abundant in the Earth's crust and extremely wide variety of uses, XAFS analysis of them in the industry has high demand. BL05 is constructed on the basis of strong demand of industrial users for XAFS spectroscopy on 2008 [1, 2]. BL05A, a branch line of BL05, is a unique double crystal monochromator (DCM) for XAFS measurements in the soft X-ray region up to 4000eV in NewSUBARU. In BL05A, a Golovchenco-type DCM has been used from 2008, the operation for public use of BL05 has started. But there was a problem with stability of the exit X-ray beam intensity, caused by deterioration of a driving mechanical translating system of the crystals on the DCM. So we replaced the DCM to new one, calculation and combination-type, in 2014. In this paper, we report improved performance of BL05A for XAFS measurements in the X-ray region about 1keV.

### 1. Improvement of beryllium filter

Certain beamlines, such as the soft X-ray beamlines, a beryllium filter is often used to protect the vacuum within the storage ring from contamination because of providing a vacuum isolation and transmitting the X-ray beam. The beryllium filter in BL05A is located in the front end, which is bonded to mounting flange and used to separate the ultra-high vacuum in the storage ring with the front-end from the high vacuum in the beamline. For the purpose of improving the transmission factor of X-rays at the lower-energy region (e.g., the *K* absorption edges of elements with atomic numbers less

than silicon), we succeeded to make the filter of thickness from 45  $\mu\text{m}$  down to 25  $\mu\text{m}$ . Fig.1 shows a comparison of transmission of the beryllium filters with thickness between 45  $\mu\text{m}$  and 25  $\mu\text{m}$ . It can be seen that the transmission is improved in the X-ray region around 1keV.

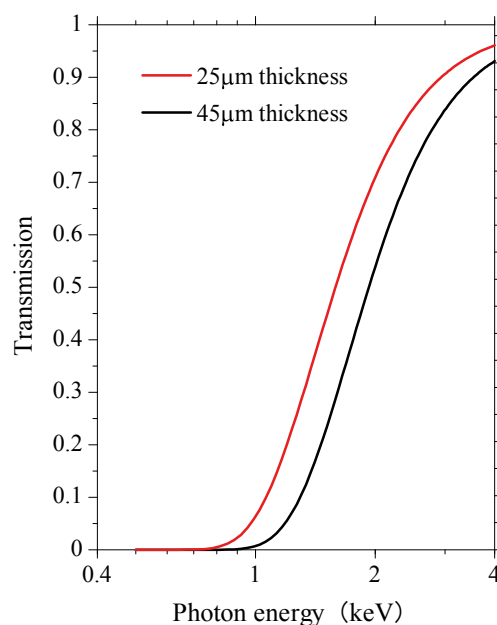


Fig.1 Transmission of beryllium filter.

### 2. Development of the available energy range of BL05A for XAFS measurements

The renewed DCM was equipped with 2 pairs of crystals, Beryl (10 $\bar{1}$ 0) and KTP (011), due to covering the lower-energy than InSb (111) crystal. Beryl crystals are often used for XAFS measurements of magnesium, the other KTP crystals are used for aluminum. But there

is a problem that these crystals are likely to be affected by radiation damage on synchrotron light. Furthermore, the thermal loading of the crystals gives rise to a difference in lattice spacing. For the reason, high sensitive XAFS measurements using these crystals are difficult. In order to minimize these effects, we introduced a water-cooling system to the DCM, which stage equipped with the first crystals is maintained at a precisely-controlled temperature with  $22.0 \pm 0.1$  degrees Celsius accuracy. In addition, the improvement of photon intensity by replacing the filter led to obtain the high-quality magnesium and aluminum *K*-edge XANES spectra [3, 4]. Then we tried to measure the sodium *K*-edge XANES spectrum using beryl crystals. In Fig.2, the measured sodium *K*-edge XANES spectra of several sodium compounds are shown. These samples were mounted to a molybdenum holder with double-sided conductive tape. The spectra of the samples were measured in the total electron yield mode, but it can be seen that highly sensitive spectra were obtained despite the insulating powder. We verified that there is enough photon intensity in these lower-energy region and can be obtained high-precision XANES spectra, which provide a detailed information related to chemical bond.

### References

- [1] T. Hasegawa *et al.*, *Advances in X-ray Chem. Anal. Jpn.*, **41**, pp.99-106 (2010) [in Japanese].
- [2] K. Kanda *et al.*, *J. Phys.: Conf. Ser.*, **425**, 132005/1-4 (2013).
- [3] T. Hasegawa *et al.*, *LASTI Annual Report*, **vol.16**, pp.73-74 (2014).
- [4] T. Hasegawa *et al.*, *LASTI Annual Report*, **vol.17**, pp.16-17 (2015).

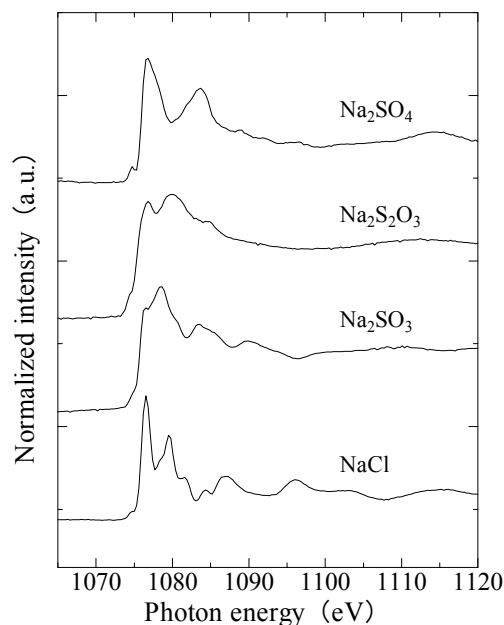


Fig.2 Na *K*-edge XANES spectra of sodium compounds.

# Erosion process of fluorinated diamond-like carbon films by exposure to soft X-rays

Kazuhiro Kanda<sup>1\*</sup>, Hiroki Takamatsu<sup>1</sup>, Eri Miura-Fujiwara<sup>2</sup>, Hiroki Akasaka<sup>3</sup>, Akihiro Saiga<sup>4</sup>, Koji Tamada<sup>4</sup>  
1 Laboratory of Advanced Science and Technology for Industry, University of Hyogo, Kamigori, Hyogo, Japan  
2 School of Engineering, University of Hyogo, Himeji, Hyogo, Japan  
3 School of Engineering, Tokyo Institute of Technology, Meguro-ku, Tokyo, Japan  
4 National Institute of Technology, Tokyo College, Hachioji-shi, Tokyo, Japan

## Abstract

The effect of soft X-ray irradiation on fluorinated diamond-like carbon (F-DLC) films was investigated using synchrotron radiation (SR). The Vickers hardness of the F-DLC films substantially increased from an initial value of  $\approx 290$  HV to  $\approx 800$  HV at a dose of 50 mA·h, the remained constant at  $\approx 1100$  HV at doses of more than 300 mA·h. This dose dependence was consistent with those of the film thickness, elemental composition, and  $sp^2/(sp^2+sp^3)$  ratio of carbon in the film. A depth profile of the elemental composition inside each F-DLC film obtained by measurement of the X-ray photoelectron spectrum (XPS) during sputtering showed that the composition ratio of fluorine was approximately constant from the surface to the neighborhood of the substrate. Namely, fluorine atoms were desorbed by the SR irradiation from not only the surface but also the substrate neighborhood. Modification by the SR irradiation was found to occur in the entire F-DLC film of thickness  $\approx 200$  nm.

## Introduction

Diamond-like carbon (DLC) film is an amorphous material that consists of  $sp^2$  hybridized carbon,  $sp^3$  hybridized carbon, and hydrogen. DLC films have been the subject of considerable attention because of their exceptional properties, namely, high hardness, low friction, chemical inertness, and good electrical insulation. DLC films have therefore been utilized as a coating material on edged tools, automobile engines, molds, optical devices, and heads of computer hard disks owing to their excellent properties. A huge market for DLCs is thus expected, and various novel DLC films have been synthesized and utilized for numerous industrial purposes. One effective way to impart a new property is to incorporate a heteroelement in addition to carbon and hydrogen into a DLC film.

Fluorinated DLC (F-DLC) films are known to exhibit particularly high insulation, a low dielectric constant, a smooth surface, low surface free energy, and chemical inertness, and are used to improve tribological properties and for the corrosion protection of steel and alloys. In addition, F-DLC films are expected to be utilized as a coating material on medical devices, electronic devices, and astronomical parts because of their excellent stain resistance due to their low surface free energy. In the industrial fields employing these applications, tolerance to X-rays is required. In general, DLC films have very strong tolerance to soft X-ray irradiation [1]. However, we have observed that the irradiation of soft X-rays on some DLC films induces the etching and/or modification of the films [2-4]. In our previous study, we found that the surface properties of F-DLC films were affected by

the irradiation of soft X-rays [5]. Upon SR irradiation, the sudden desorption of fluorocarbon species from the F-DLC film surface, increases in surface wettability, film density, and the ratio of  $sp^2$  hybridized carbon atoms, and decreases in the film thickness and fluorine content of films were observed. These reactions stopped when the fluorine ratio in the F-DLC films decreased to  $\approx 10\%$  as a consequence of SR irradiation. In the present study we attempt to clarify the surface modification process of F-DLC films by the irradiation of soft X-rays. We studied the effect of soft X-rays on the bulk properties of F-DLC films with the aim of ensuring the safe use of F-DLC films in the X-ray environments.

## Experimental

Fluorinated DLC film was deposited on Si wafer using an amplitude-modulated radio-frequency plasma-enhanced chemical vapor deposition method (Nippon ITF) [6], which was same sample as used in our previous study [5]. The film thickness was estimated to be 216 nm by the observation of a section image of F-DLC film using a scanning electron microscope (SEM; JEOL, JSM-6700). The fluorine and hydrogen contents of as-deposited F-DLC film were estimated to be about 50 at.% and less than 4 at.%, respectively, using a combination of Rutherford backscattering spectrometry (RBS) measurement and elastic recoil detection analysis (ERDA) measurement. This hydrogen was likely to have originated from adsorbed molecules. In other words, the film was considered to include no hydrogen. Such film has

been industrially used for coating rubber and resin to improve their abrasion resistance and sliding properties.

The soft X-ray irradiation of F-DLC films was carried out at BL06 in the NewSUBARU synchrotron facility of the University of Hyogo. Details of the experimental apparatus at BL06 have been described in previous reports [7]. In brief, the SR extracted from a bending magnet, which is the light source of BL06, was introduced to the sample stage as a straight beam via a pair of mirrors. The SR was irradiated onto the film surface perpendicularly. The SR at the BL06 sample stage had a continuous spectrum from the infrared to soft X-ray region and an energy below 1 keV. This energy range includes 300 eV and 690 eV, which are the ionization energies of a carbon *K* shell and a fluorine *K* shell, respectively. During the experiment, the electron energy of the NewSUBARU ring was 1.0 GeV and the ring current was 300 mA in the top-up mode. The SR dose [mA·h] was derived as the product of the ring current [mA] and the exposure time [h]. During the exposure of the F-DLC films to soft X-rays, the pressure in the irradiation chamber was on the order of  $10^{-5}$  Pa and the temperature of the sample stage was confirmed to be room temperature using a thermocouple. After the SR exposure, the modified F-DLC films were stored in a dry box.

## Results

The F-DLC films were exposed to SR to investigate their modification process upon the irradiation of soft X-rays. The dependence of the Vickers hardness of the F-DLC film on the SR dose was measured for SR doses from 0 to 1000 mA·h. The measurement of the depth profile of the elemental composition from the surface to the substrate and the observation of surface images and

section images of the F-DLC films were performed at several doses.

Figure 1 shows the dependence of the Vickers hardness of the F-DLC films on the SR dose. Vickers hardness was measured using a nanoindenter (ELIONIX NT-110a). In this measurement, the maximum load was 0.1 mN, using a quadrilateral diamond as the indenter. The Vickers hardness of the F-DLC film before irradiation was  $\approx 290$  HV, which markedly increased to  $\approx 800$  HV after 50 mA·h SR exposure. It further increased to  $\approx 1100$  HV after 300 mA·h SR exposure, then remained constant at  $\approx 1100$  HV at doses of more than 300 mA·h.

The depth profile of the elemental composition of the inside of the F-DLC film was investigated by the measurement of XPS, while Ar sputtering. XPS spectra were measured using a conventional XPS apparatus (ULVAC-PHI, PHI X-tool) with the Mg *K $\alpha$*  line (1253.6 eV) as the X-ray source. Figure 2 shows the depth profile of (a) the elemental composition of the F-DLC film before irradiation, (b) that after irradiation with an SR dose of 100 mA·h, and (c) that after irradiation with an SR dose of 1000 mA·h. The X-axis indicates the number of cycles of Ar sputtering. In all films, the composition ratio of silicon suddenly increased after about ten cycles. This increase indicated that the Si wafer substrate had been exposed by Ar sputtering. The etching depth per sputtering cycle was estimated to be about 20 nm for the F-DLC film before irradiation. The composition ratio of fluorine on the film surface was before irradiation about 0.4, in agreement with our previous measurement [5]. The composition ratio of fluorine in the F-DLC film before irradiation was slightly higher in the neighborhood of the surface but approximately constant from bulk to the neighborhood of the substrate. The mean composition ratio of fluorine from the film surface to the substrate was estimated to be 0.31. Upon SR irradiation, the composition ratio of fluorine in the F-DLC film decreased; the composition ratio after SR irradiation was slightly lower near the surface but approximately constant from bulk to the neighborhood of the substrate, similarly to the F-DLC film before irradiation. In other words, the thickness of the F-DLC film that can be modified by SR irradiation was greater than 200 nm. The mean composition ratio of fluorine from the film surface to the substrate decreased to 0.22 after an SR dose of 100 mA·h and to 0.15 after an SR dose of 1000 mA·h.

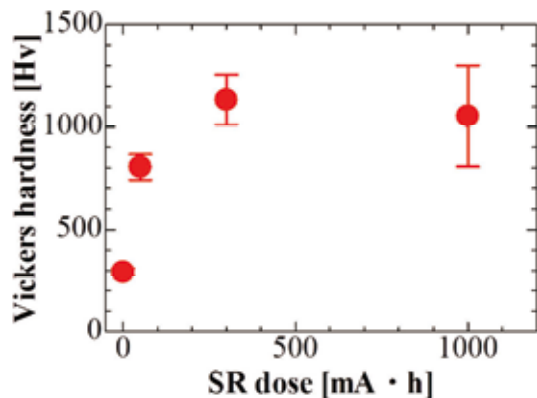


Fig.1 Dependence of Vickers hardness of F-DLC films on SR dose.

Surface images and section images of the F-DLC films were observed using a SEM, section of each F-DLC film was created by dividing the F-DLC film with the Si wafer substrate. The F-DLC

film surface was coated with Au to impart conductivity because the charging of the film surface by the irradiation of an electron beam was expected because of the high insulation of the F-DLC film. SEM images of F-DLC film surfaces enlarged by a factor of 70,000 are shown in Fig. 3

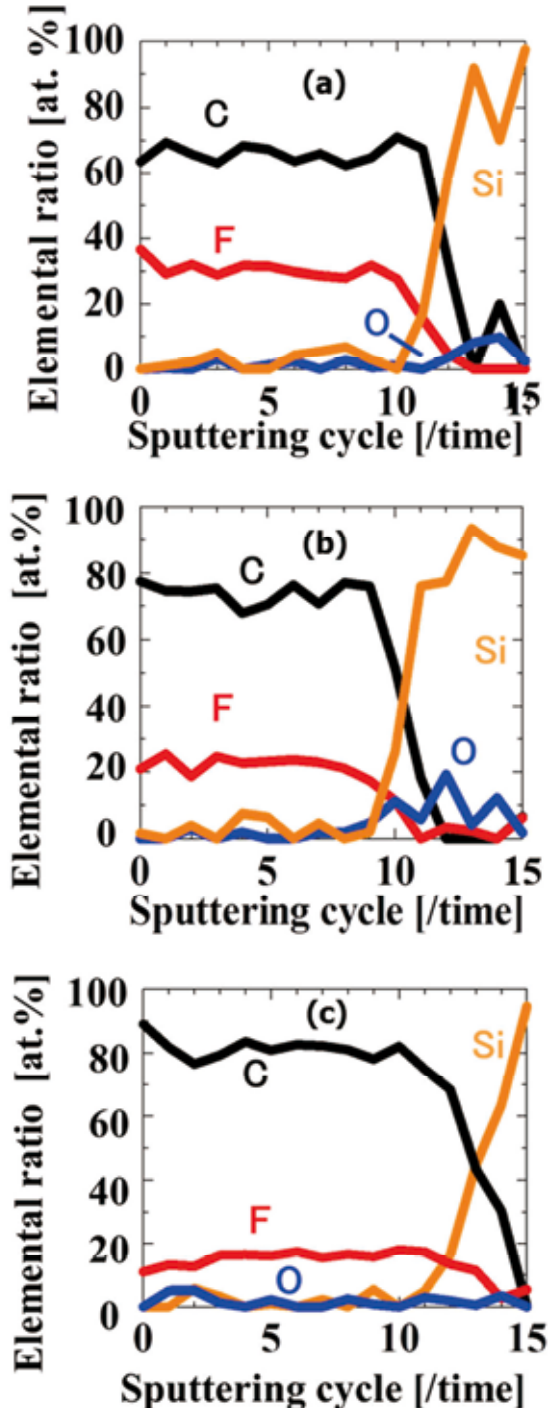


Fig. 2 Dependence of depth profile of elemental composition of inner F-DLC film on SR dose (a) before irradiation, (b) after irradiation with SR dose of 100 mA·h, and (c) after irradiation with SR dose of 1000 mA·h.

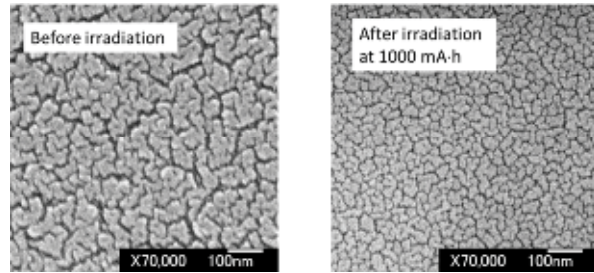


Fig. 3 SEM images of F-DLC film surface (a) before irradiation and (b) after irradiation with SR dose of 1000 mA·h.

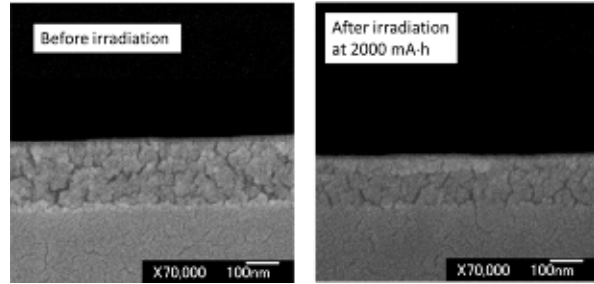


Fig. 4 SEM section images of F-DLC film (a) before irradiation and (b) after irradiation with SR dose of 2000 mA·h.

(a) before irradiation and in Fig. 3 (b) after irradiation with an SR dose of 1000 mA·h. Numerous cracks were observed on the F-DLC film surface before irradiation as shown in Fig. 3 (a). Upon SR irradiation, the number of cracks increased and their width decreased. Figures 4 (a) and (b) show section images of the F-DLC film enlarged by a factor of 70,000 before irradiation and after irradiation with an SR dose of 2000 mA·h, respectively. Many cracks that reached the substrate were observed in both images. Species that desorbed upon the irradiation of SR were considered to have passed through these cracks.

#### Discussion

We investigated the effects of soft X-ray irradiation on F-DLC films by focusing on the depth of modification. The modification process of the F-DLC film by the irradiation of SR is considered to be as follows. (i) Carbon and/or fluorine atoms in the F-DLC film were excited by the soft X-rays corresponding to the ionization energies of the C K shell and/or F K shell. (ii) Carbon-carbon bonds, which were bonded to fluorine atom, were decoupled and F-containing species were desorbed from the F-DLC film. The composition ratio of fluorine in the film decreased because the main desorbed species were CF and CF<sub>3</sub>. (iii) The desorption of CF<sub>x</sub> species caused a decrease in the film thickness. (iv) Carbon atoms with an unpaired electron that remained after

desorption of  $CF_x$  species coupled neighboring carbon atoms also having an unpaired electron. This coupling caused an increase in the  $sp^2/(sp^2+sp^3)$  ratio of carbon atoms in the F-DLC film because carbon-carbon double bonds were formed by this coupling. (v) The process stopped when the fluorine ratio in the F-DLC film decreased to  $\approx 10\%$  upon the irradiation of SR with a dose of 300 mA·h [5]. As a result, the film thickness, the composition ratio of fluorine, and the  $sp^2/(sp^2+sp^3)$  ratio of carbon atoms had a similar dependence on the dose; they substantially changed up to a dose of 50 mA·h and remained constant at doses of more than 300 mA·h.

An increase in the Vickers hardness of the F-DLC films was observed after SR irradiation in the present work. The creation of new bonds between carbon atoms in step (iv) of the above process is considered to have enhanced the film hardness. The Vickers hardness substantially increased up to a dose of 50 mA·h and remained constant at doses of more than 300 mA·h. This dependence of the Vickers hardness on the SR dose is in agreement with those of the film thickness, elemental composition, and  $sp^2/(sp^2+sp^3)$  ratio of the carbon in the film on the SR dose. This indicated that modification by SR irradiation proceeded on the film surface at the same time as inside of the F-DLC film because the film hardness was determined by the structure of the whole film. This was proved from the measurement of the depth profile of the elemental composition by XPS during

Ar sputtering, which indicated that the F composition ratio changed almost uniformly from the surface of the film to the neighborhood of the substrate. The transmission of the F-DLC film in the present work was estimated using the X-ray database of the Center for X-ray Optics at Lawrence Berkeley National Laboratory [8]. Assuming the elemental composition, density, and thickness substituted from the result of our previous work [5], F/C ratio = 1, 1.99 g/cm<sup>3</sup>, and 216 nm, respectively, the transmission of this film was estimated to be 0.29 at 287.2 eV, which corresponded to the absorption edge of the C K-edge. Therefore, it was possible to excite carbon atoms in the neighborhood of the substrate by X-rays in the present experiment. As observed using the SEM, numerous cracks that connected the substrate to the surface existed in the films. We consider that the desorbed species were emitted through these cracks.

The behavior of the F-DLC film upon SR irradiation, such as the decrease in film thickness, the increase in the  $sp^2/(sp^2+sp^3)$  ratio of carbon atoms, and the increase in Vickers hardness, stopped above an the SR dose of over 300 mA·h. This was ascribed to the decrease in the fluorine content in the film to  $\approx 15\%$  by desorption of the F-containing species induced by the SR irradiation. As a result, the F-DLC film whose F content was lower than 15 % exhibited durability against the irradiation of soft X-rays.

## References

- [1] H. Kyuragi and T. Urisu, Synchrotron radiation-induced etching of a carbon film in an oxygen gas, *Appl. Phys. Lett.* **50** (1987) 1254-1256.
- [2] K. Kanda, K. Yokota, M. Tagawa, M. Tode, Y. Teraoka, S. Matsui, Effect of the soft X-rays on highly hydrogenated diamond-like carbon films, *Jpn. J. Appl. Phys.* **50** (2011) 055801.
- [3] R. Imai, A. Fujimoto, M. Okada, S. Matsui, T. Yokogawa, E. Miura, T. Yamasaki, T. Suzuki, K. Kanda, Soft X-ray irradiation effect on the surface and material properties of highly hydrogenated diamond-like carbon thin films, *Diamond Relat. Mater.* **44** (2014) 8-10.
- [4] K. Kanda, R. Imai, M. Niibe, H. Yoshioka, K. Komatsu, H. Saitoh, Modification processes for highly hydrogenated diamond-like carbon thin films by soft X-ray irradiation, *Sens. Mater.* **29** (2017) in press.
- [5] H. Takamatsu, M. Niibe, X.L. Zhou, K. Komatsu, H. Saitoh, H. Akasaka, A. Saiga, K. Tamada, M. Tagawa, K. Yokota, Y. Furuyama, K. Kanda, Soft X-ray irradiation effect on the fluorinated DLC film, *submitted to Diamond Relat. Mater.*
- [6] T. Nakahigashi, Y. Tanaka, K. Miyake, H. Oohara, Properties of flexible DLC film deposited by amplitude-modulated RF P-CVD, *Tribol. Int.* **37** (2004) 907-912.
- [7] K. Kanda, T. Ideta, Y. Haruyama, H. Ishigaki, S. Matsui, Surface modification of fluorocarbon polymers by synchrotron radiation, *Jpn. J. Appl. Phys.* **42** (2003) 3983-3985.
- [8] <http://www.cxro.lbl.gov/>

# Surface modifications in Silica-Based Films by Undurator Radiation with a multilayer spectrometer

K. Moriwaki, T.Miyamoto, Graduate School of Eng., Kobe Univ.,  
and K.Kanda, LASTI/Univ. Hyogo

## Abstract

Undurator radiation (UR) by the NewSUBARU (BL7A) is used for silica-based films modifications for future applications of optical devices like waveguides. UR with or without a multilayer spectrometer is used for the samples, and the observed effects are compared. Increases in the refractive index (about  $10^{-3}$ ) are obtained by shortening the peak wavelength. The peak wavelength dependence is found in the experiments, but is not clear at the present stage. A correlation is found between the absorbance increases and the refractive-index changes, which suggest the origin of the refractive-index change. This is also supported by the refractive index decreases after removing the high absorbance layer in the sample. The difference between the samples irradiated with and without the spectrometer may be caused by the irradiation intensity and a sample temperature effect.

## Introduction

Synchrotron radiation (SR) and undurator radiation (UR) are used for radiation-induced refractive index changes or other modifications in silica-based glass for optical devices like optical waveguides<sup>1,2)</sup>. Especially, the former experiments revealed differences between UR-irradiated samples with and without a spectrometer<sup>2)</sup>. UR is a very useful tool for the materials modifications, because it can select a useful wavelength, having very high intensity. UR with a multilayer spectrometer would be more useful for the purpose because it has high intensity and the most suitable wavelength can be selected without higher order ones. In this report, modification effects are compared with or without the spectrometer further than that in the previous reports<sup>2)</sup>.

## Experiments and Results

Thermally grown SiO<sub>2</sub> films on Si substrates and fused quartz substrates were used for the UR irradiation. UR with the first-peak energy ranging from 80 to 300eV is used with the spectrometer. Irradiated samples were characterized by XPS (X-ray Photoelectron Spectroscopy), optical absorption spectroscopy, and refractive index measurements.

Figure 1 shows refractive index changes after irradiation by UR without the spectrometer<sup>2)</sup>. Very high refractive index changes are introduced in the samples that are mainly by the surface reduction layer having Si-Si bonds<sup>1,2)</sup>. By using monochromatic irradiation with a multilayer film spectrometer, refractive index rises are observed (Fig.2), but Si-Si bonds are not found by XPS measurements. That may be caused by decrease in the irradiation intensity and the temperature by UR with the

spectrometer. The photon energy dependence on the refractive index is shown in Fig.2. The refractive indices in Fig.2 have a peak at around 180eV peak energy, but reproducibility is not clear at the present experiments.

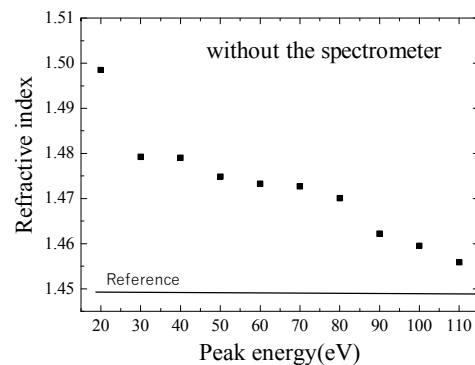


Fig.1 Refractive index changes after irradiation by UR without the spectrometer.

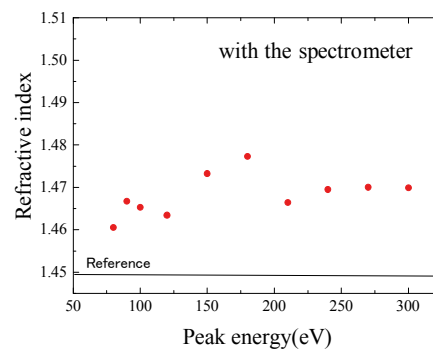


Fig.2 Refractive index changes after irradiation by UR with the spectrometer.

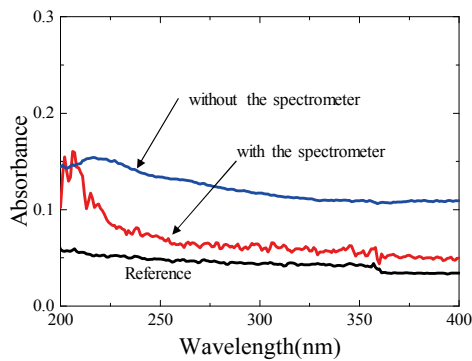


Fig.3 Optical absorbance for samples irradiated by UR with and without the spectrometer.

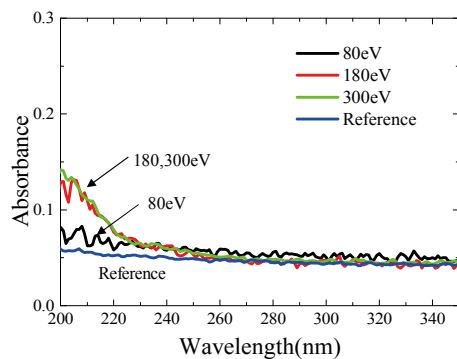


Fig.4 Optical absorbance for samples irradiated by UR with the spectrometer. The peak photon energies are changed as 80, 180 and 300eV.

Absorbance increases are observed for the samples irradiated by UR with and without the spectrometer (Fig.3), although the increases are relatively low for ones with the spectrometer. Absorbance are also measured by changing the peak photon energies (Fig.4). In Fig.4, changes by the peak energy are found. Defects in the samples by the UR irradiation may be the origin of the refractive index changes, therefore, correlation between the absorbance and the refractive index changes is expected, and is confirmed as shown in Fig.5.

It is concerned that the defects generation is the cause of the refractive index changes. That is supported by the results of refractive index decrease after removing the high absorbance layer. Figure 6 shows refractive index decreases gradually after etching an UR-irradiated sample. The sample after 80nm etching shows a large decrease in the index but a little change is

remained comparing to the reference of the initial one.

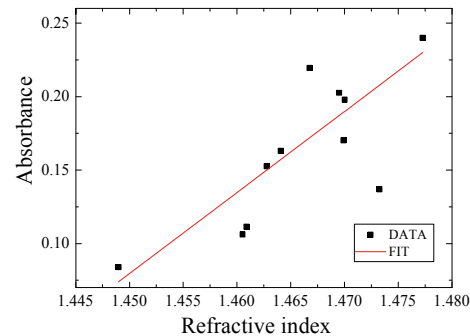


Fig.5 Correlation between absorbance and refractive-index changes after irradiation by UR with the spectrometer.

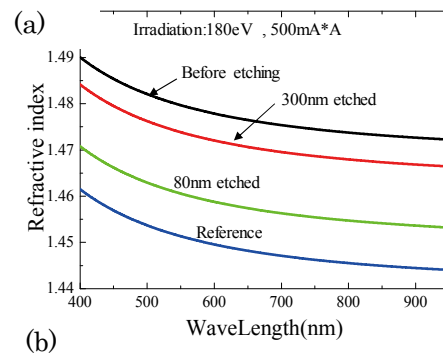
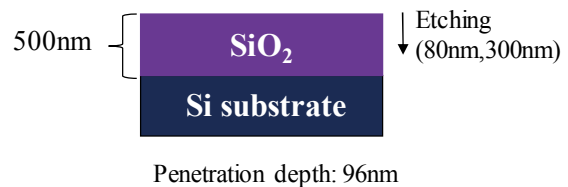


Fig.6 (a) Cross-sectional view for an UR-irradiated sample. (b) Measured refractive-index changes after UR irradiation with the spectrometer, before and after etching by 80 and 300nm.

## Conclusions

UR irradiation with the spectrometer made defects in the sample, which may be the origin of the refractive-index changes. Further investigations are needed to determine both the cause of the changes and also the most effective radiation conditions for future applications

## References

- [1] K.Moriwaki et al., LASTI Annual Report vol.16 (2014).
- [2] K.Moriwaki et al., LASTI Annual Report vol.17 (2015).

# Molecular orientation of imprinted photoreactive liquid crystalline polymer measured by near-edge X-ray absorption fine structure

Y. Haruyama<sup>1</sup>, M. Okada<sup>1</sup>, E. Nishioka<sup>2</sup>, M. Kondo<sup>2</sup>, N. Kawatsuki<sup>2</sup>, and S. Matsui<sup>1</sup>

<sup>1</sup> LASTI, University of Hyogo, Ako, 678-1205, Japan

<sup>2</sup> Graduate School of Engineering, University of Hyogo, Himeji, 671-2280, Japan

## Abstract

Near-edge X-ray absorption fine structure (NEXAFS) spectra of polymethacrylate, which has a hexamethylene spacer group terminated with a 4-oxycinnamic acid in its side chain (P6CAM), were measured at the C K-edge region. From the dependence on the incident angle of the linear polarized synchrotron radiation in the NEXAFS spectra of imprinted P6CAM thin films, it was found that the unoccupied  $\pi^*$  orbitals originating from aromatic ring sites in P6CAM thin films orient to the surface normal direction irrespective of the line direction formed by the imprint process.

## Introduction

The studies on the photoinduced orientation of the polymeric films have attracted significant attention for a potentially wide range of applications such as birefringent optical devices, the photo alignment layer of liquid crystal displays, and optical memories. Optical anisotropy of the polymeric films has been created by irradiating the linearly polarized UV light to the films [1]. From the UV-vis spectra, Kawatsuki *et al.*, indicated that the liquid crystals in P6CAM orient is perpendicular to the polarization direction of the UV light [1].

Nanoimprint lithography is a promising method to fabricate various nanostructures by pressing the mold to the resist. Recently, Okada *et al.*, had successfully demonstrated that the photoreactive liquid crystalline polymer was reoriented along to the line direction formed by the imprint process [2]. However, the mechanism of the molecular reorientation of photoreactive liquid crystalline polymer is not clear at present. To investigate the molecular reorientation of the photoreactive liquid crystalline polymer, near-edge X-ray absorption fine structure (NEXAFS) spectra were measured at the C K-edge region.

## Experiments

A polymethacrylate, which has a hexamethylene spacer group terminated with a 4-oxycinnamic acid in its side chain (P6CAM),

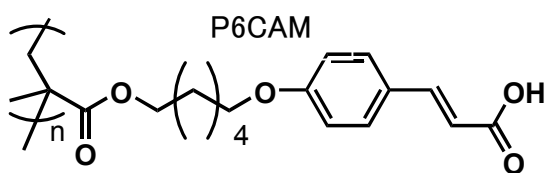


Fig.1 Chemical structure of P6CAM.

was used as a photoreactive liquid crystalline polymer. The chemical structure was shown in figure 1. P6CAM was synthesized as described in a previous paper [1]. P6CAM thin films of 200 nm thickness were prepared by spin-coating a tetrahydrofuran (THF) solution of the polymers onto ITO coated glasses. The 2  $\mu$ m line and space patterns were formed on the surface by the imprint process as shown in figure 2.

NEXAFS spectra measurements were carried out using the beamline 7B of the NewSUBARU facility at the University of Hyogo. To investigate the molecular orientation of P6CAM films, NEXAFS spectra at the C K-edge region were measured by the total electron yield (TEY) method. The sample could be rotated around a vertical axis to change the incidence angle of the SR to the sample surface. The direction of the linear polarization in the SR was horizontal. NEXAFS spectra of P6CAM thin films were recorded in parallel and perpendicular configurations, where the direction of linearly polarized light in SR was parallel and perpendicular to that of the line pattern formed by imprint process on the surface, respectively.

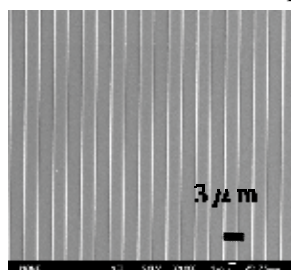


Fig.2 SEM image of the 2  $\mu$ m line and space pattern formed by imprint process on the surface of P6CAM.

## Results and discussion

Figures 3(a) and 3(b) show the C K-edge NEXAFS spectra of imprinted P6CAM thin films, measured by the TEY method, as a function of incidence angle of the SR in parallel and perpendicular configurations, respectively. A sharp peak at 284.8 eV, which was assigned to transitions from the C 1s orbital to the unoccupied  $\pi^*$  orbitals originating from aromatic ring sites, was observed. With increasing the incidence angle, the intensity of the peak at 284.8 eV decreased gradually in the parallel configuration. In addition, the similar angular dependence was observed in the perpendicular configuration. These results indicate that the unoccupied  $\pi^*$  orbitals originating from aromatic ring sites in P6CAM thin films orient to the surface normal direction although the molecular axis of the liquid crystals in the side chains of P6CAM is random.

Figure 4 shows the angular dependences of the  $\pi^*$  resonance intensity in the parallel and perpendicular configurations for imprinted P6CAM thin films. The angular dependence of the  $\pi^*$  resonance intensity in the parallel configuration is almost the same as that in the perpendicular configuration. Therefore, in the case of the imprinted P6CAM thin films, this indicates that the unoccupied  $\pi^*$  orbitals originating from aromatic ring sites in P6CAM thin films orient to the surface normal direction irrespective of the line direction formed by the imprint process. This is in contrast to the previous result [2]. The difference may be attributed to

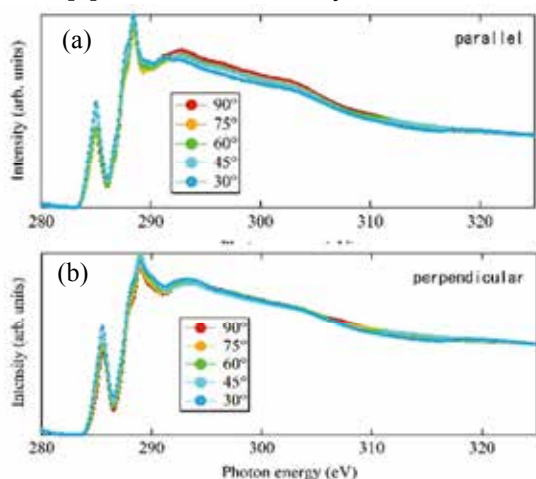


Fig.3 C K-edge NEXAFS spectra of imprinted P6CAM thin films as a function of the incidence angle  $\theta$ , relative to substrate surface in (a) parallel and (b) perpendicular configurations, respectively.

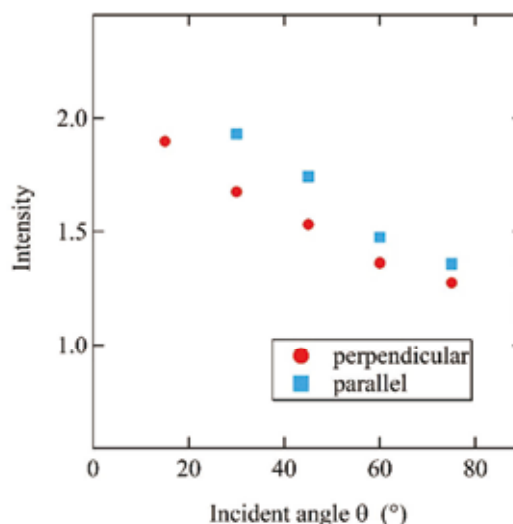


Fig.4 Angular dependence of the  $\pi^*$  resonance intensity in the parallel and perpendicular configurations for imprinted P6CAM thin films.

the detected area in each experimental method. The NEXAFS spectra observed by the electron yield method in this study is detectable only near the surface region. On the other hand, the whole area of the thin films is detectable in the previous study [2]. Therefore, there is a possibility that the molecular ordering of the liquid crystals in P6CAM thin films differs between the surface and the bulk.

## References

- [1] N. Kawatsuki, T. Kawanishi, and E. Uchida: *Macromolecules* **39**, pp. 9357 (2006).
- [2] M. Okada, S. Manabe, M. Kurita, M. Kondo, Y. Haruyama, K. Kanda, A. Emoto, H. Ono, N. Kawatsuki, and S. Matsui: *Jpn. J. Appl. Phys.*, **49**, pp. 128004 (2010).
- [3] M. Okada, S. Manabe, M. Kurita, M. Kondo, Y. Haruyama, K. Kanda, N. Kawatsuki, and S. Matsui: *Microelectronic Engineering* **88**, 2079 (2011).

# Development of fine-grained 316L steel with 1.0-2.0 mass% TiC for nuclear reactor materials

Mititaka Terasawa<sup>a</sup>, Hiroaki Kurishita<sup>b</sup>, Tatsuaki Sakamoto<sup>c</sup>, Masahito Niibe<sup>a</sup>, Heishichiro Takahashi<sup>d</sup>, Satoru Nishikawa<sup>e</sup>, Atsusi Yamamoto<sup>f</sup>, Michiru Yamashita<sup>g</sup>, Tohru Mitamura<sup>a</sup>, Tohru Yamasaki<sup>f</sup> & Masayoshi Kawai<sup>h</sup>

<sup>a</sup>Laboratory of Advanced Science & Technology for Industry, University of Hyogo, Kamigori-cho, Japan;

<sup>b</sup>International Research Center for Nuclear Materials Science, IMR, Tohoku University, Ibaraki, Japan;

<sup>c</sup>Department of Materials Science and Biotechnology, Ehime University, Matsuyama, Japan;

<sup>d</sup>Center for Advanced Research of Energy and Materials, Hokkaido University, Sapporo, Japan;

<sup>e</sup>Nondestructive Evaluation Center, Japan Power Engineering and Inspection Corporation, Yokohama, Japan;

<sup>f</sup>Graduate School of Engineering, University of Hyogo, Himeji, Japan;

<sup>g</sup>Hyogo Prefectural Institute of Technology, Kobe, Japan;

<sup>h</sup>High Energy Accelerator Research Organization (KEK), Tsukuba, Japan

## Abstract

Development of fine grain 316L with small amount of TiC for high radiation tolerant performance was tried considering the fabrication process of thermo-mechanical treatments. The materials obtained are UFG316L+2.0 mass% TiC with the grain size of 90 to 270 nm, depending on the final annealing temperature from 700°C to 900°C. The materials was examined by TEM observation, XANES spectroscopy, HVEM electron irradiation and Stress Corrosion Cracking by crevice bent beam method in high temperature water with 8 ppm dissolved oxygen. The test results showed the material is generally excellent quality. Especially void swelling induced by the electron irradiation at 400°C is less than 1/10 compared to the commercial SUS316L.

## Introduction

Austenitic stainless steels have been employed extensively for nuclear power reactors for many years, because the materials show very tough mechanical strength and excellent performances in the environment of water coolant exposure and neutron irradiation in high temperature. Although void swelling induced by neutron irradiation is the typical severe problem in fast breeder reactors (FBR), it has not been considered so far in the light water reactors (LWR) because the irradiation fluence is much more lower than in FBR. However, void formation (swelling) was recognized at lower temperature (400°C) even in LWR by Garner [1]. It is noticed that swelling-creep interaction in fuel pin cladding may cause the fuel pins to deform into spiral rods. As grain boundaries (GBs) of the poly-crystal materials are great sink for the defects produced by neutron irradiation, fine grain materials are expected to show high radiation-tolerant performance [2,3].

We tried to develop ultra-fine grain austenitic stainless steels (UFG316L) with addition of TiC-nanoparticles. In the previous paper, we reported the fabrication of UFG316L+1.0 mass% TiC, which was examined by neutron irradiation in JMTR (JAEA) and high voltage electron microscope (HVEM) 1.0 MeV electron irradiation. Less hardening and low void swelling in the irradiations by neutron and/or high-energy electron were recognized [4]. We have tried the fabrication of UFG316L+2.0 mass% TiC as the next step of the

material development.

## Experiments and Results

Powders of SUS316L (an average particle size: 44–105  $\mu\text{m}$ ) and TiC (0.57  $\mu\text{m}$ ) were used as the starting materials. These powders were mixed to provide the target compositions of SUS316L and 2.0 mass% TiC. These mixed powders together with hard steel balls were put into a vessel made of SUS316L steel and then subjected to mechanical alloying (MA) treatment by vibrational ball milling for 125 h in a purified hydrogen atmosphere (purity: 99.99999%). All of these procedures were conducted in a specially designed glove box that prevents the powders from being contaminated with oxygen and nitrogen in air before and after the MA treatment. Hot isostatic pressing (HIP) treatment was conducted at 850 °C at 196 MPa for 3 h in an argon atmosphere. The HIPed compacts were subjected to thermomechanical treatments (TMTs) to introduce ultrafine grained, thermally stable nanostructures by using reverse transformation of deformed martensite to austenite.

The grain sizes are as small as 90, 140, 190, and 270 nm, after heat treatment at 700°C, 750°C, 800°C, and 900°C, respectively.

In the present experiment, *in situ* observation of the defects evolution in UFG316L+2%TiC materials was performed during the material irradiation with 1.0 MeV electron beam in the HVEM facility in Hokkaido University, Japan.

Figure 1 shows the swelling as a function of the

irradiation fluence, dpa. The swelling data of the specimen UFG316L+2%TiC are compared with the commercial normal grained SUS316L and UFG+1%TiC, which (the latter two) were reported in the previous report [4]. As shown in this diagram, amounts of the swelling of these steels increase with increasing the fluence of the irradiation. The swelling of the commercial normal-grained SUS316L steel increases up to 0.08% at 5 dpa. On the other hand, the UFG316L+1%TiC specimen shows extremely slow increment of swelling with less than 0.01% in the same dpa range. It is found in this study that the material with 2.0 mass% TiC reveals much more effect to suppress the void formation in comparison with the 1.0 mass% TiC materials until the fluence increases up to 6 dpa, though in much higher fluence than 6 dpa, the void swelling data are almost the same level for both

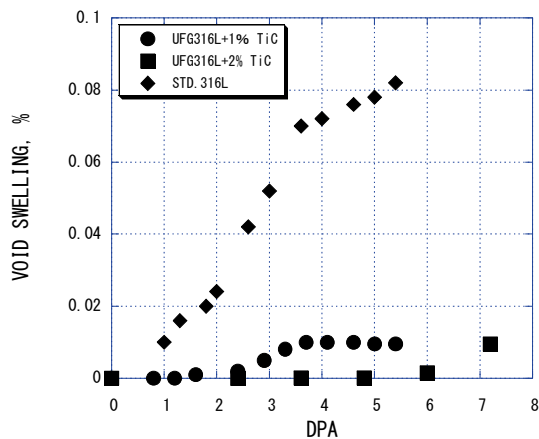


Fig. 1 Swelling as a function of the irradiation fluence, dpa.

materials.

It is confirmed that TiC addition of 1 to 2 mass% is quite effective to prevent the defects evolution and void formation during high-energy electron irradiation. It is understood that many of the radiation-induced defects could be annihilated at the GB, because small TiC dispersoids reduce the grain growth owing to the radiation-induced defects could be annihilated at the GB.

The average sizes of TiC existing at GBs are from 70 to 110 nm, while those within grains are from 20 to 50 nm, depending on the heat treatment: The particle sizes at GBs and within grains increase with the increasing heat treatment temperature from 700 °C to 900°C. UFG316L+2%TiC (as HIPed).

We tried to measure the electronic states of Ti in the UFG316L+2%TiC materials in order to elucidate the behavior of Ti or TiC in the fabrication process. X-ray absorption near edge structure (XANES) spectroscopy was performed at the end-station of the undulator beamline BL-09A

in the 1.5 GeV synchrotron light source, NewSUBARU in the University of Hyogo. Figure 2 shows XANES spectra of Ti-L<sub>2,3</sub> for the UFG316L+2%TiC specimens. The black line denotes as the measurement, the green line as decomposed, and the red line as superposition of the decomposed lines. The Ti-L<sub>2,3</sub> spectra are separated to two peaks (463.8 and 465.5 eV) for L<sub>2</sub>, and other two peaks (458.7 and 460.3 eV) for L<sub>3</sub>. The lower energy peak in L<sub>2</sub> is t<sub>2g</sub> ( $\pi$ -type bonding formed by Ti3d<sub>xy, dxz, dyz</sub> orbitals and C2p orbitals), and the higher energy peak is e<sub>g</sub> ( $\sigma$ -type bonding formed by Ti3d<sub>x<sup>2</sup>-y<sup>2</sup>, dz<sup>2</sup></sub> orbitals surrounding C atoms with the NaCl-type structure. Likewise the lower energy peak in L<sub>3</sub> is due to t<sub>2g</sub>, and higher energy peak in e<sub>g</sub>. The energies of the peaks in the UFG materials coincide with the corresponding

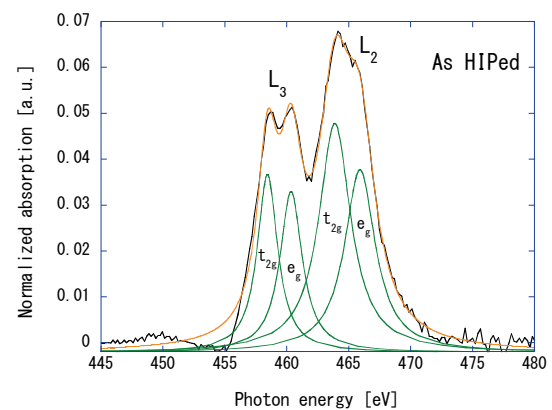


Fig. 2 XANES spectra of Ti-L<sub>2,3</sub> for the UFG316L+2%TiC specimens.

peaks in the TiC powder.

Although the 316L stainless steel is evaluated normally as excellent nuclear reactor materials for stress corrosion cracking (SCC), the present materials UHG316L+2%TiC was tested for the SCC because the effect of fine-grained material for the SCC is not known. The SCC test by crevice bent beam method was performed in hot water with 8 ppm dissolved oxygen at 289°C and 7 MPa for 3000 hr. The test results were reasonable and quite similar to the result reported for normal 316L materials.

## References

- [1] Garner FA., In: 1st International Workshop on Voids in In-core Structural Materials in LWR; Dec 15; Kyoto, Japan. (2003)
- [2] Kurishita et al., J Nucl Mater. **233–237**:557–564 (1996)
- [3] Kitsunai et al., J Nucl Mater. **239**:253–260 (1996)
- [4] Matsuoka et al., Congress on Advances in Nuclear Power Plants (ICAPP05) in cooperation with IAEA; 2005 May 15–19; Seoul, Korea (paper 5687) (2005)

# Surface Structure Analysis of AlGa<sub>N</sub> thin films damaged by Oxygen and Nitrogen Plasmas

Ryo Tanaka<sup>1</sup>, Masahito Niibe<sup>1</sup>, Retsuo Kawakami<sup>2</sup>, Yoshitaka Nakano<sup>3</sup>, Takashi Mukai<sup>4</sup>  
<sup>1</sup>University of Hyogo, <sup>2</sup>Tokushima University, <sup>3</sup>Chubu University, <sup>4</sup>Nichia Corporation.

## Abstract

In order to understand the details of the surface damage to the AlGa<sub>N</sub> film by plasma etching, we etched it with oxygen and nitrogen plasmas, and analyzed by using NewSUBARU beamline BL-09A. The peak of near-edge X-ray absorption fine structure (NEXAFS) spectra in the N-K absorption edge was broadened by oxygen plasma etching with increased processing time. In the case of nitrogen plasma, it was more broadened than the sample etched by oxygen plasma. And the peak of X-ray emission spectroscopy indicated that the etching damage does not reach the bulk of the sample. From the above results, the changes in the crystalline structure of AlGa<sub>N</sub> are considered to be caused by the effect of UV light irradiation from plasma. We found that the change in the surface composition, the disordering of the crystalline structure occurred on a shallow region from the surface, and those did not occur on a deeper region of the sample.

## Research background

Aluminum gallium nitride (AlGa<sub>N</sub>) is attracting a great deal of attention as a new material for electronic devices. AlGa<sub>N</sub> has a large band gap, is chemically stable, and is physically strong. In particular, the AlGa<sub>N</sub> / Ga<sub>N</sub> high electron mobility transistor (HEMT) can realize high-speed operation and low power consumption operations. In the heterostructure of AlGa<sub>N</sub> / Ga<sub>N</sub>, the lattice constants of AlGa<sub>N</sub> and Ga<sub>N</sub> are different so that the crystal is distorted, and the two-dimensional electron gas (2DEG) is induced in the AlGa<sub>N</sub>/Ga<sub>N</sub> interface. Since the 2DEG has high carrier density and high electron mobility, very fast switching operation becomes possible. There are several issues for realizing AlGa<sub>N</sub>/Ga<sub>N</sub> HEMT devices into practical use, one of the biggest problems is to make normally-off HEMT devices.

Regularly, HEMT devices have normally-on characteristics. Normally-on operation is a state in which drain current ( $I_D$ ) flows when gate voltage ( $V_G$ ) is 0 V. Normally-off operation is a state in which  $I_D$  does not flow when  $V_G$  is 0 V.

HEMT devices are expected to be used for high-current power amplifiers. Therefore devices of the normally-off operation is required especially from the viewpoint of fail-safe. In recent years, Kotara et al. [1] reported that AlGa<sub>N</sub>/Ga<sub>N</sub> HEMT devices turned to normally-off characteristics by

using CF<sub>4</sub> plasma etching. According to this report, a 25 nm AlGa<sub>N</sub> film was grown on a Ga<sub>N</sub> substrate with a thickness of 1.1 μm and the surface was CF<sub>4</sub> plasma etched. As a result,  $V_G$  was shifted to the normally off side by + 2 V compared to the HEMT which was not plasma-etched. In addition, Miyawaki et al. [2] studied that AlGa<sub>N</sub>/Ga<sub>N</sub> HEMT devices turned normally-off HEMT devices by using O<sub>2</sub> or N<sub>2</sub> plasma etching.

It seems that the reason normally-off is related to surface damage by plasma etching and ion species to be taken in. However, the mechanism of normally-off HEMT devices are not yet clarified. To investigate this mechanism in detail, we used plasma etching with O<sub>2</sub> gas and N<sub>2</sub> gas (gas pressure was changed 10 to 100 mTorr and processing time was changed 5 to 100 min) to the AlGa<sub>N</sub>/Ga<sub>N</sub> substrate.

## Experimental Methods

AlGa<sub>N</sub> films used were 100 nm thick un-doped Al<sub>0.24</sub>Ga<sub>0.76</sub>N thin films which were grown on 4 μm thick bufferlayer of Ga<sub>N</sub> by metal organic chemical vapor deposition (MOCVD) in this study(Nichia Corp.).

AlGa<sub>N</sub> sample was plasma etched at Kawakami laboratory in Tokushima University. The capacitively-coupled radio frequency plasma

(CCP) reactor was used for etching. Figure 2 shows a schematic diagram of the CCP reactor. The apparatus had an asymmetric electrode structure. The cathode area  $S_K = 80 \text{ cm}^2$ , the anode area  $S_A = 1217 \text{ cm}^2$ , and the distance between the electrodes was 4 cm. The radio frequency (RF) power was supplied at 13.56 MHz and  $V_{RF} = 200 \text{ V}$ . The anode electrode was grounded. In this research, plasma etching was carried out by using two types of gases, oxygen and nitrogen. The processing gas pressure was from 10 to 100 mTorr, and the treatment time was from 5 to 100 min.

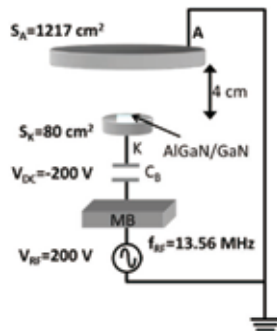


**Figure 2** Schematic diagram of capacity coupled plasma reactor

### Evaluation Devices and Methods

For the evaluation of the etched samples, the analysis of the etching damage was carried out by X-ray absorption spectroscopy (XAS) at the BL-09A at the NewSUBARU synchrotron radiation facility. The absorption coefficient was measured by two methods: total electron yield (TEY) and total fluorescence yield (TFY). TEY is a method that can know the surface crystal state from the sample surface to about 3 nm [3]. TFY is known that it is possible to observe the bulk crystalline state from 10 nm to several 100 nm from the sample surface.

In this study, an angle of incidence is defined as the angle measured from the surface normal.

### Results

Figure 3 (a) shows the N-K NEXAFS spectra of the AlGaIn sample subjected to oxygen plasma treatment measured with TEY method. The angle of incidence was  $0^\circ$  (normal incidence). The figures show spectra obtained from the sample etched by oxygen plasma at 100 mTorr.

As shown in Fig. 3 (a), when comparing the as-grown sample and the plasma etched sample as

a whole, as the gas pressure is higher and as the treatment time becomes longer, the overall spectral shape tends to be smoothed. This is probably because the crystal structure of the AlGaIn surface was distorted by etching.

Figure 3 (b) shows the N-K NEXAFS spectra of the AlGaIn treated with oxygen plasma at 100 mTorr measured with TFY method. From this it can be seen that there is not much change in the spectra even if the processing time is changed. This is probably because the influence of etching on the inside of the AlGaIn sample is small.

From the results of TEY and TFY measurements of AlGaIn samples treated with oxygen plasma, etching damage by oxygen plasma does not reach to the bulk, which shows that it influences only the AlGaIn surface (about  $\sim 3 \text{ nm}$ ).

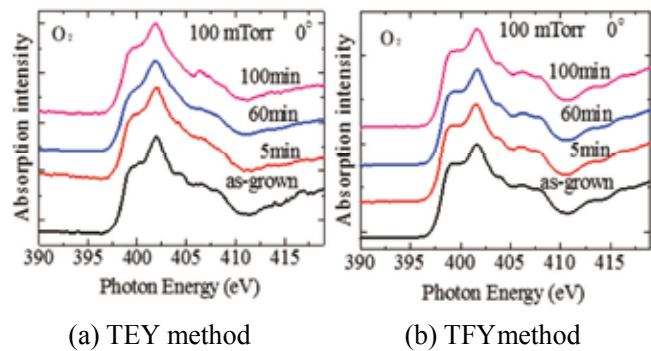
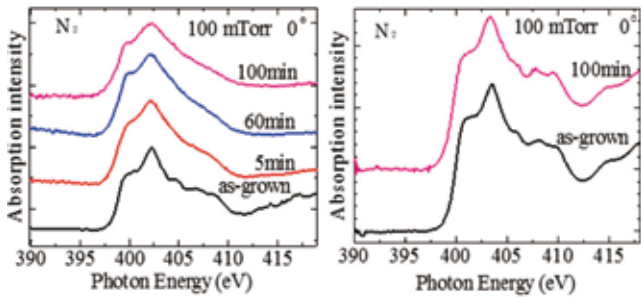


**Figure 3** N-K NEXAFS spectra of oxygen plasma treated AlGaIn samples

Figure 4 (a) shows the N-K NEXAFS spectra of the AlGaIn samples treated with nitrogen plasma measured by TEY method. As shown in Fig. 4 when comparing the as-grown sample and the plasma etched sample as a whole, as the gas pressure is higher and as the treatment time becomes longer, the overall spectral shape tends to be smoothed. This is probably because the crystal structure of the AlGaIn surface was distorted by etching.

Comparing the spectra in Figure 3 (a) with that of in Figure 4 (a), the spectra of nitrogen plasma treated samples are much smoother than that of oxygen plasma treated one. Therefore, it can be seen that etching damage by nitrogen plasma etching is larger than that by oxygen plasma etching. Figure 4(b) shows the N-K NEXAFS spectra of the AlGaIn treated with nitrogen plasma at 100 mTorr measured with TFY method. Spectra

of samples etched at 5 min and 60 min could not be observed. From this it can be seen that there is not much change in the spectra even if the



processing time is changed. This is probably because the influence of etching on the inside of the AlGaN sample is small.

(a) TEY method (b) TFY method

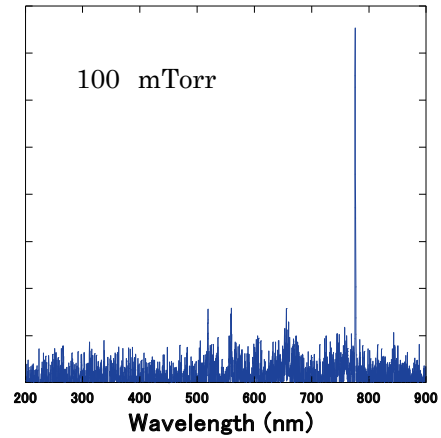
**Figure 4** N-K NEXAFS spectra of nitrogen plasma treated AlGaN samples

### Discussion

From the results of NEXAFS spectrum plasma etching greatly influenced the sample surface (about ~ 3 nm). And under the same conditions, the nitrogen plasma etching was larger in etching damage than that of the oxygen plasma etching. Our research group reported that the surface roughness increased with ultraviolet light-assisted irradiation of n-GaN samples using black light in the previous work [5]. We also reported that similar effects are generated by Ar and UV assisted CF<sub>4</sub> plasma [6]. This is probably because ultraviolet light with photon energy corresponding to a band gap is irradiated on the AlGaN surface, and electron-hole pairs are generated. The formation of holes h<sup>+</sup> on the surface weakened the bonding between Al-N and between Ga-N, which is considered to promote plasma etching. In addition, AlGaN has large dislocation density (~ 10<sup>8</sup> cm<sup>-2</sup>), so holes concentrate at dislocation sites, making it difficult to be etched easily [7]. It seems that pit-like defects were formed on the AlGaN surface.

Figure 5 shows the ultraviolet spectrum emitted from plasmas. Since the band gap energy (E<sub>g</sub>) of AlGaN is 3.67 eV, wavelength λ of the corresponding energy is 338 nm.

In the emission spectrum from the nitrogen plasma in Fig. 5 (b), since photons with the wavelength (338 nm) corresponding to the AlGaN



band gap are generated, the bond breaks due to plasma emission, thereby increasing the etching damage.

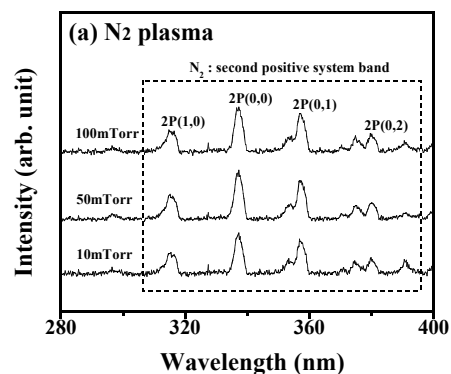
(a) Ultraviolet spectrum of oxygen plasma

(b) UV spectrum of nitrogen plasma

**Figure 5** UV spectrum of plasma emission

### References

- [1] P. Kotara et al., Phys. Status Solidi C **8**, 2207 (2011).
- [2] Miyawaki et al., 2014 autumn meeting of Applied Physics Japan (2014)
- [3] T. Kotaka et al, Adv. X-Ray. Chem. Anal., Japan, **43** ISSN 0911-7806 (2012).
- [4] M. Katsikini et al., Journal of Physics: Conference Series **190**, 012065 (2009).



[5] R. Kawakami et al., Thin Solid Films **570**, **81** (2014).

[6] S. Hirai et al., E-Journal of Surface Science and Nanotechnology, **13**, 481-487 (2015).

[7] D. M. Follstaedt et al., Journal of Crystal Growth, **310**, 766-776 (2008).

# Development of the Transmittance Measurement for EUV Resist by Direct-Resist Coating on a Photodiode

Daiki Mamezaki, Masanori Watanabe, Tetsuo Harada, and Takeo Watanabe

*Center for EUV Lithography, LASTI, University of Hyogo,  
1-1-2 Kouto, Kamigori, Ako-gun, Hyogo, Japan  
d.mame@lasti.u-hyogo.ac.jp*

To increase the sensitivity of extreme-ultraviolet (EUV) resist, the method of adding high absorption material in base resin of the resist such as hafnium or zirconium metal has been developed. Since the EUV absorption of the base resin increases, the secondary electron emissions would increase to have a high-resist-exposure sensitivity. Thus to achieve the high sensitive EUV resist, it is important to evaluate EUV absorption of the EUV resist precisely. We have developed a novel transmittance measurement method to evaluate EUV resist absorption with high precision at BL10 beamline of NewSUBARU synchrotron light facility. In this novel method, a sample resist was coated on an EUV photodiode directly. The EUV transmittance of the resist was measured with photodiode signals before and after the coating. The resist thickness uniformity coating on a photodiode has much smaller value compared to that coating on a freestanding membrane. By novel method, the measurement precisions of the resist thickness and the EUV transmittance were significantly improved. As the result, the high measurement precision of absorption coefficient of 1% was achieved. This novel method will help the development of high sensitive EUV resist with the high-absorption material.

**Keywords:** EUV resist, transmittance measurement, high absorption resist, metal resist

## 1. Introduction

The extreme-ultraviolet (EUV) lithography [1] is the most promising candidate for the manufacturing of semiconductor electronic devices. One of the critical technical issues of EUV lithography is the development of EUV resist which has the high resolution, the high sensitivity, the low line-width roughness, and low outgassing simultaneously [2]. Especially, the high sensitivity is strongly required to relax the specification of EUV light power and maintain the high-lithographic throughput. To achieve the high sensitive resist, some groups reported several methods in the paper [3, 4]. The key to increase the sensitivity is employing the high-EUV-absorption-metal material such as hafnium or zirconium in the base resin of EUV resist. Since the EUV absorption of the base resin increased and the secondary electron emissions could increase, the resist sensitivity increased. In

order to evaluate the effect of the high absorption material, it is important to evaluate the EUV absorption of the EUV resist precisely. The absorption coefficient is calculated using the following equation (1).

$$\mu = \frac{1}{D} \ln \left( \frac{1}{T} \right) \quad (1)$$

Where  $\mu$ ,  $D$ , and  $T$  are the absorption coefficient, resist thickness and transmittance of the resist. In order to evaluate the absorption coefficient of resist material, the precise measurement the resist thickness and EUV transmittance are required.

We previously performed [5-7] the transmittance measurement of EUV resist using the EUV reflectometer at BL-10 beamline in the NewSUBARU synchrotron light facility [8]. The absorption coefficient was calculated by using the transmittance and the resist thickness. In this

previous experiment [8], silicon-nitride freestanding membranes were used for the resist transmittance measurement. The resist was coated on the silicon-nitride membrane by spin-coating. The EUV transmittance of the resist was computed by the EUV transmittances of the membrane before and after the resist coating. Figure 1 shows schematic view of the membrane. The thickness, window size and substrate size of the silicon-nitride membrane was 200 nm,  $2 \times 2 \text{ mm}^2$  and  $10 \times 10 \text{ mm}^2$ , respectively. Since the membrane thickness was very thin, the membrane was deflected by the stress after the resist spin coating. And the resist thickness uniformity on the membrane affected by the adhesion of the resist. As the results, the resist thickness uniformity on the membrane became very large to be approximately 10%. On the other hand, EUV beam size on the sample of the reflectometer was 0.8 mm (horizontal)  $\times$  0.1 mm (vertical) in full width in half maximum (FWHM). Since the beam size was comparable to the membrane-window size, the precision of the transmittance measurement affected by the non-uniformity of resist thickness. And before the transmission measurement, it is necessary to align the membrane position precisely to the beam position.

Thus to increase the transmission-measurement precision, we have developed a novel transmission-measurement method for EUV resist. In the new method, sample resist was direct coated on an EUV sensitive photodiode, which is usually used for a measurement of the EUV light intensity in the EUV energy region. The EUV transmittance of the photoresist was computed with photodiode signals before and after the coating.

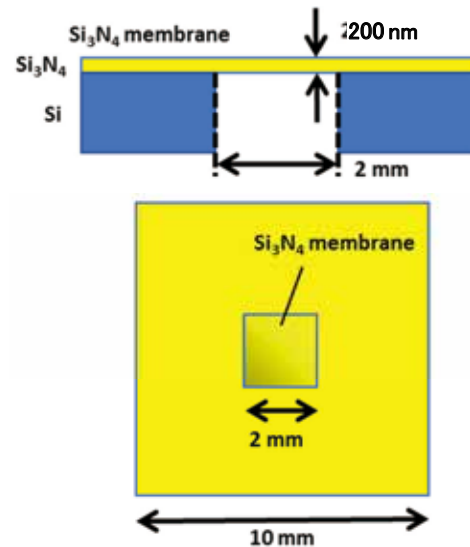


Fig. 1. Schematic view of the silicon-nitride membrane substrate used for the EUV resist transmission measurement previously.

## 2. Experimental

### 2.1 Photoresist coating

It was used in this experiment that ZEP520A (Zeon Corp.) which was non-chemical-amplified positive-tone resist and commonly used for electron-beam lithography.

Schematic view of the photodiode (SXUV-100 Opto Diode) used in this experiment is shown in Fig. 2.

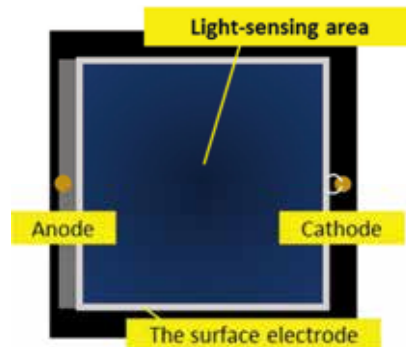


Fig. 2. Schematic view of SXUV-100 in novel transmission method.

Light-sensing area size of the photodiode was  $10 \times 10 \text{ mm}^2$ , which was much larger than the beam size. Thus the beam alignment in the novel method is much easier than that in the previous method. The resist was coated on the sensing area ( $10 \times 10 \text{ mm}^2$ ) by spin coating directly. Uniform resist thickness was expected at the spin coating process, because the photodiode surface was flat and solid. The resist thickness was measured using NanoSpec6100 (Nanometrics),

which is a film thickness measurement system based on an interference-spectrum measurement. A film thickness measurement spot size in NanoSpec6100 was 25  $\mu\text{m}$  in diameter. The prebake process of the resist film coated on a light-sensing surface of the photodiode was provided using a hot plate. The prebake temperature was 180°C, which was much lower than the heat-resistant temperature of the photodiode of 260°C.

Top surface layer of the photodiode was a passivating metal silicide [9, 10]. And the back side electrode was contacted to the anode. The surface electrode was contacted to the cathode by the wire. The wire of the photodiode-cathode shown in Fig. 2 is very narrow wire and easy to be cut off. During the spin-coating for the resist coating, the wire was cut off several time. And, during the resist-baking process, the wire was also cut off by a heat stress. Thus, we contacted a metal electrode by a kinematic contact to the surface electrode on the photodiode to measure photodiode current. Even if the wire was cut off, the signal could be measured by the metal electrode using this contact method.

## 2.2 Transmittance measurement method

In this study, the EUV mask reflectometer [11] was used for the EUV transmittance measurement, which was located at the BL-10 beamline of NewSUBARU synchrotron light facility. Figure 3 shows the photograph of the EUV mask reflectometer installed at the BL10. The bending magnet is used as a light source of the BL-10 beamline and white light is generated from this source. The monochromator type is Monk-Gillieson type [12] with a plane varied-line-spacing grating (VLSG). An energy resolution of ( $\Delta E/E$ ) in EUV region is approximately 1300.

In this experiment, the exposure wavelength was 13.5 nm, and the exposure beam size at the resist sample position in the EUV mask reflectometer was approximately 0.8 mm (horizontal)  $\times$  0.1 mm (vertical) in FWHM. Since the sensing area of photodiode was much larger than the beam size, it was easy to align the beam position.

Figure 4 shows schematic diagram of the measurement method of a EUV resist transmittance. First, the photodiode-signal distribution  $I_0(y)$  along the vertical  $y$  direction at the horizontal center position was measured

before the resist coating. Then, the signal distribution  $I(y)$  was measured after the resist coating. The transmittance distribution  $T(y)$  was calculated with  $I_0(y)$  and  $I(y)$  by the equation of  $T(x) = I(x)/I_0(x)$ .

## 3. Result and discussions

### 3.1 The measurement of resist thickness

Figure 5 shows a measurement results of the resist thickness on the photodiode. The thickness distributions for the four angles were measured, where result in 90° was corresponded to vertical  $x$  direction at the EUV transmittance measurement.

The average, maximum and minimum resist thickness were 120.1 nm, 120.4 nm and 119.8nm, respectively. Thus, the resist was coated on the photodiode with high uniformity. Non-uniformity was less than 0.5%, which was 20 times smaller than the previous method with the silicon-nitride membrane.

The resist transmittance region using photodiode is  $< 2.5$  mm at the radial position  $r$ , which the measurement region of 5-mm in diameter in this method was larger than the membrane window width size of 2 mm in the previous measurement method.

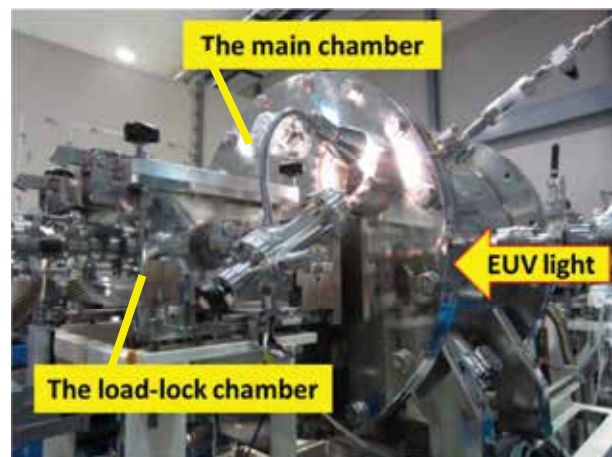


Fig. 3. Photograph of the EUV mask reflectometer.

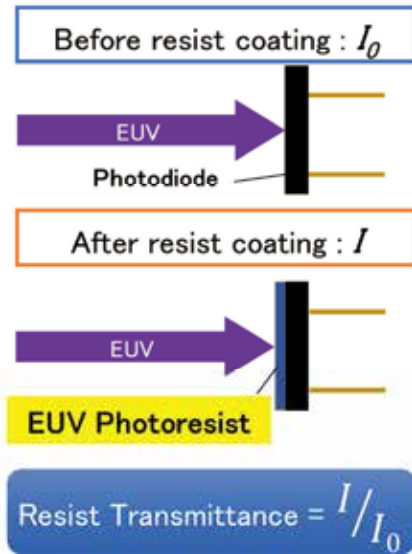


Fig. 4. Schematic diagram of the measurement method of the resist-transmittance measurement.

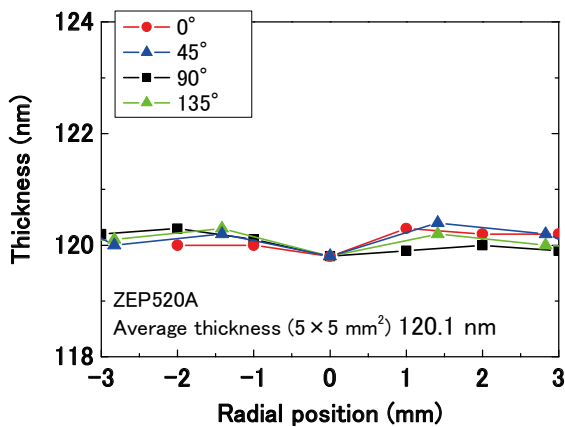


Fig. 5. Measurement results of the resist thickness.

### 3.2 Transmittance measurement

Figure 6 shows the measurement result of resist transmittance. The average resist transmittance was 62.2%, and the non-uniformity of the resist transmittance was 0.7%. Since the resist thickness was uniform shown in Fig. 5, the high precision measurement of EUV transmittance was achieved.

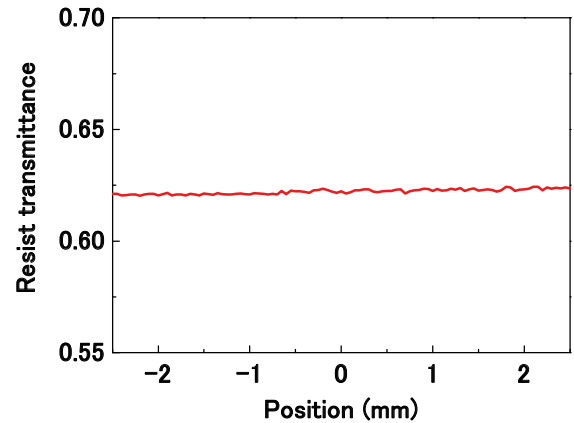


Fig. 6. Measurement result of the resist transmittance.

### 3.3 Computation of the absorption coefficient

Figure 7 shows absorption coefficient distribution which were calculated by the measurement results of the resist thickness in 90° and EUV transmittance. As a result, the computed average absorption coefficient was  $3.96 \mu\text{m}^{-1}$ . The variation of the absorption coefficient in the evaluation area ( $r < 2.5 \text{ mm}$ ) was less than 1%. This residual variation of the measurement precision would be small for resist absorption measurement.

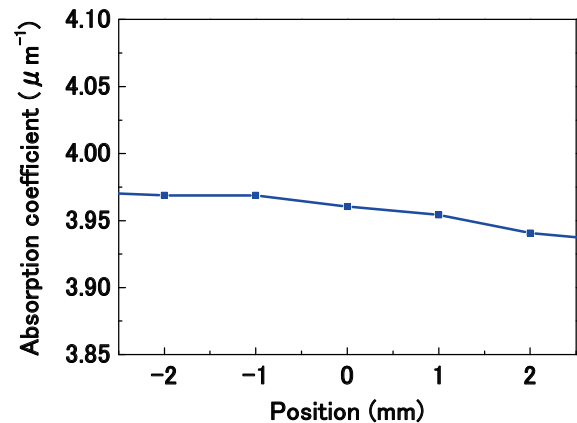


Fig. 7. Computed result of absorption-coefficient on the photodiode.

## 4. Conclusion

We have developed the novel method of the resist-transmittance measurement using the direct-resist coating method on the photodiode. The thickness nonuniformity of resist by spin coating was significantly improved to be 0.5%, because the photodiode surface was flat and solid. Thus, the variations of the resist transmittance

and the absorption coefficient were also improved to 0.7% and 1%, respectively. We performed precise EUV absorption-coefficient evaluation using this novel method. This new method will help the development of high-absorption material to achieve high-sensitive-EUV-resist material.

In the near future, we will develop the resist removal method to reuse the photodiode. And, we will evaluate a metal-resist absorption using this novel method.

## 5. References

1. H. Kinoshita, K. Kurihara, Y. Ishii and Y. Torii: *J. Vac. Sci. & Technol.*, **B7** (1989) 1648.
2. Mark Neisser and Stefan Wurm: *Advanced Optical Technologies*, **4**, (2015) 535.
3. Jing Jiang, Souvik Chakrabarty, Mufei Yu and Christopher K. Ober: *Journal of Science and Technology* **27**(2014) 663.
4. Jason K. Stowers, Alan Telecky, Michael Kocsis, Benjamin L. Clark, Douglas A. Keszler and Andrew Grenville: *Proc. SPIE* **7969** (2011) 15.
5. Atsushi Sekiguchi, Yoko Matsumoto, Tetsuo Harada, Takeo Watanabe, and Hiroo Kinoshita: *Proc. of SPIE Vol.* **9422** (2015) 2L.
6. Yasuyuki Fukushima, Takeo Watanabe, Tetuo Harada and Hiroo Kinoshita: *Journal of Photopolymer Science and Technology* **22** (2009) 85.
7. Ryuji Ohnishi, Takeo Watanabe, Yasuyuki Fukushima, Masafumi Osugi, and Hiroo Kinoshita: *Jpn. J. Appl. Phys.* **48** (2009) 06FA08.
8. Masaki Kuki, Tomoyuki Uemura, Masato Yamaguchi, Tetsuo Harada, Takeo Watanabe, Yasuji Muramatsu and Hiroo Kinoshita: *Journal of Photopolymer Science and Technology Vol.* **28** (2015) 531.
9. R. Stuik and F. Bijkerk: *Nuclear Instruments and Methods in Physics Reserch* **489** (2002) 370.
10. B. Kjomrattanawanich, R. Korde, C. N. Boyer, G. E. Holland and J. F. Seely: *IEEE Transactions on Electron Devises*, Vol. **53** (2006) 218.
11. M. Hosoya, N. Sakaya, O. Nozawa, Y. Shiota, K. Hamamoto, O. Nagarekawa, S. Shimojima, T. Shoki, T. Watanabe, and H. Kinoshita: *Jpn. J. Appl. Phy.* **47** (2008) 4898.
12. M. C. Hettrick and J. H. Underwood, *AIP Conf. Proc.* **147** (1986) 237.

# EUVL Research Activity at Center for EUV Lithography

**Takeo Watanabe and Tetsuo Harada**

*Center for EUV Lithography,*

*Laboratory of Advanced Science and Technology for Industry, University of Hyogo,*

*3-1-2 Koto, Kamigori, Ako-gun, Hyogo, 678-1205, Japan*

The advanced feature size patterning process of semiconductor conductor devices has been strongly charged in the information-technology oriented society. Extreme ultraviolet lithography (EUVL) is expected as a leading candidate of the next generation lithography for semiconductor electronic devices. The technology issues in EUV lithographic are the development of 1) EUV light source with high power and high stability, 2) EUV resist with simultaneous achievement of high resolution, high sensitivity, low line width roughness (LWR), and low outgassing. Center for EUVL in University of Hyogo has played an important role in the research and development of EUV lithography in two decades. Research and development of EUV lithography toward HVM was started its development just before twenty years ago to develop full field exposure tool employing tree aspherical imaging optics. In University of Hyogo developed 1) large reflectometer for the reflectivity measurement of the collector mirror for the EUV light source, 2) the EUV resist evaluation system such as the EUV interference lithography and outgassing system using in-situ ellipsometer for the evaluation of EUV resist of 10 nm and below, and X-ray absorption fine structure for EUV resist chemical reaction analysis to increase EUV exposure sensitivity, 4) the defects inspection of the actinic blanks and patterned mask. As the results, those evaluation tool could contribute EUV lithographic technology to lead to the HVM of electronic devices.

**Keywords:** EUV lithography, interference lithography, PAG bounded polymer, outgassing, in-situ ellipsometer, chemical reaction analysis, XAFS, actinic blank inspection, actinic patterned mask inspection, coherent scatterometry microscope

## 1. Introduction

EUVL [1] will be used in the semiconductor electronic device high volume manufacturing for the patterning in the 16 nm feature size around 2017 [2]. The top three issues of the EUVL are the development of 1) source, 2) resist, and 3) mask. For the EUV light source development, high power and high stability of EUV light source should be achieved to maintain the wafer throughput [3]. EUV source power of 250 W with the occupancy rate of 75% is required for the HVM EUV light source. And for the EUV power for 1000W, EUV light source on the basis of the

free electron laser source is planned on the basis of the accelerator technology. For the EUV resist development, the simultaneous achievement of the high resolution, sensitivity, low LER, and low out gassing. For the mask development, the defect inspection of the actinic blank and patterned mask and the pellicle to protection the mask from the particle originated from the mask loading and unloading in the exposure tool.

Currently, on Feb. 25, 2015, ASML press release announced that using ASML NXE-3300B exposure beta tool, the EUV-light-source power increased to 90 W at

the intermediate focus position, and TSMC semiconductor chip manufacturer exposed 1022 wafers in 24 hours. 10-nm-feature-size-patterning technology is required in 2020 for the high volume manufacturing listed in the international technology roadmap for semiconductor (ITRS) [2]. Now the 200 W at 60 min was continuously achieved using laser-produced plasma (LPP) system by reducing the diameter of the droplet and increasing CO<sub>2</sub> laser power.

For the EUVL extendability to the X nm resolution achievement, since increasing the numerical aperture of the imaging optics is needed, imaging optics is designed for the high NA optics.

Center for EUV lithography (CEL) is established in Oct. 2010 in Laboratory of Advanced Science and Technology for Industry of University of Hyogo to accelerated the EUV lithographic technology toward HVM.

This paper focuses on the EUVL R&D activity at Center for EUV Lithography of Laboratory of Advanced Science and Technology for Industry, University of Hyogo. CEL has three beamline such as BL3, BL9, and BL10 of NewSUBARU synchrotron light facility [4] for the R&D of EUVL as shown in Fig. 1 which is the schematics.

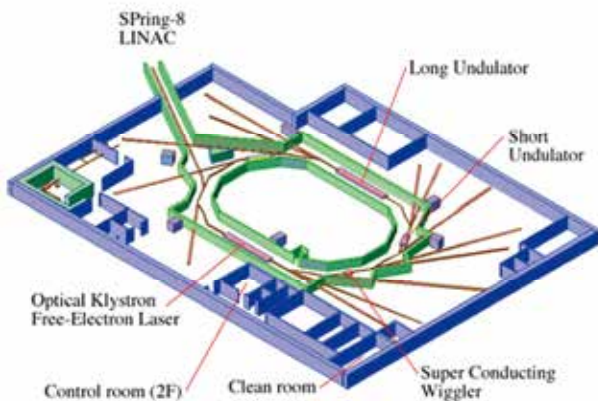


Fig. 1. The schematics view of NewSUBARU synchrotron light facility.

## 2. Large Reflectometer for the High Power EUV LPP Light Source

The high power and stability EUV source is required for HVM. The requirement of the source power is >250 W at intermediate focus position, and the occupancy rate is > 75%.

In this SPIE spring microlithography meeting, ASML announces that the conversion efficiency increases by reducing the droplet size from 34 to 27  $\mu\text{m}$ . In order to increase the power, the conversion efficiency but also the collection efficiency of the collector mirror should increase. Thus the large reflectometer is installed at the BL10 beamline of the NewSUBARU synchrotron light facility as shown in Fig. 2. The vacuum chamber size and base pressure are 2.6 m in diameter and 2.9 m in height, and  $2.0 \times 10^{-6}$  Pa, respectively. The collector mirror can be settled on the sample stage as shown in Fig 3, and the maximum

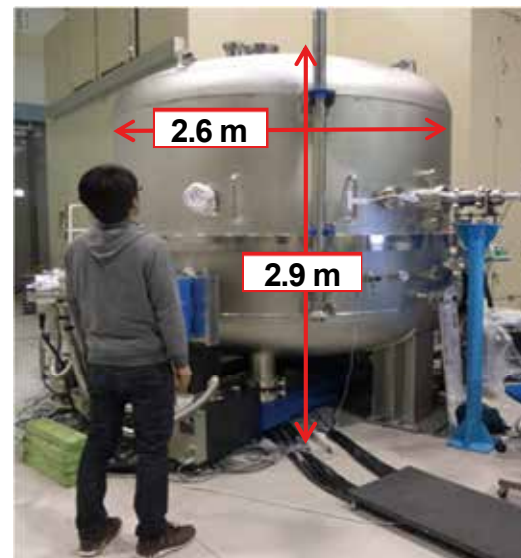


Fig. 2. Large reflectometer is installed at the BL10 beamline of the NewSUBARU synchrotron light facility.

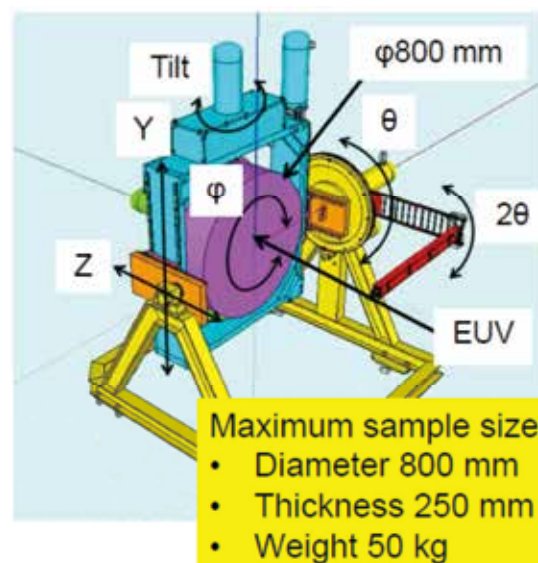


Fig. 3. The schematic view of the sample stage of the large reflectometer.

mount size of the collector mirror and weight are 800 mm in diameter and the thickness of 250 mm, and 50 kg of body weight, respectively.

Figures 4 and 5 show the mirror sample, and its reflectivity measurement result of the round robin of the reflectivity measurement between PTB and University of Hyogo, respectively. The diameter of the mirror is 412

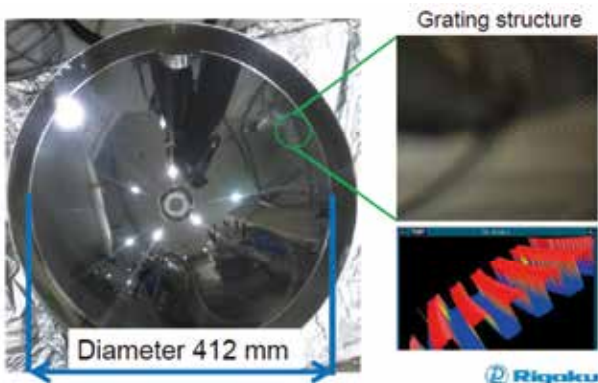


Fig. 4. Photograph of the large collector mirror used for the round-robin reflectivity measurement between PTB and University of Hyogo.

mm. The reflectivity measurement was carried out from the center position of the mirror sample to the left and right direction along the radial direction of the mirror sample. As the results, since the reflectivity measurement results between University of Hyogo and PTB is consistent, the large reflectometer which we developed has a capability to measure the reflectivity of the large collector to increase the collection efficiency for the achievement of the high-EUV-power-light source.

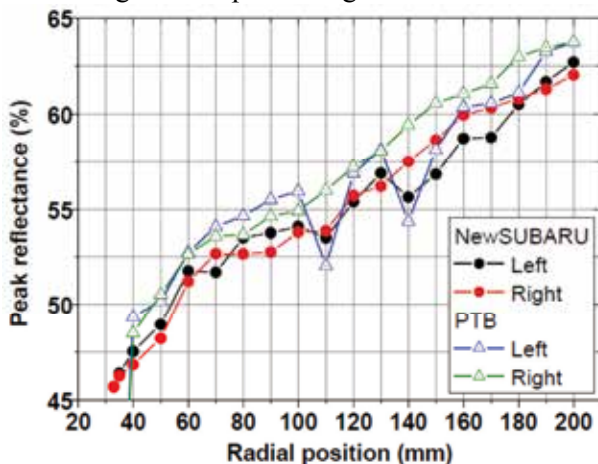


Fig.5. Reflectivity measurement results of the round robin using large reflectometer at University of Hyogo and PTB in Germany.

### 3. Resist Evaluation System

#### 3.1 EUV interference lithography

The resolution specification of ASML NXE3350B EUV exposure tool is 16 nm. Thus it cannot reach to the resolution of 10-nm order. In order to accelerate the EUV resist development of 10-nm order, it is very significant to develop the EUV interference lithographic (EUV-IL) [5] exposure tool for the resolution achievement of 10-nm order [4]. The EUV interference lithography had been developed and replicated 15 nm line and space (L/S) resist pattern by using two window-type transmission diffraction grating (TDG) on which has 30 nm L/S grating pattern. In addition, 28-nm-diameter-hole resist pattern had been replicated by four window-type TDG which has 40 nm L/S grating pattern [6, 7]. The replicated 15 nm L/S and 28 nm hole resist patterns on a silicon wafer are shown in

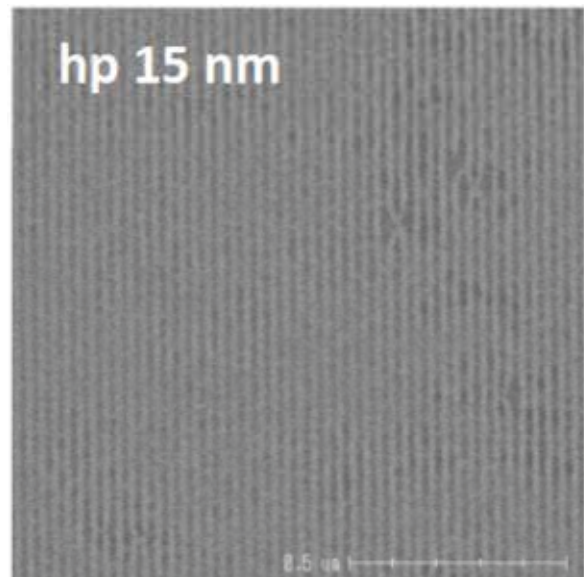


Fig. 6. 15-nm-L/S pattern of the inorganic-resist using EUV-IL.

Figs 6 and 7, respectively [8, 9].

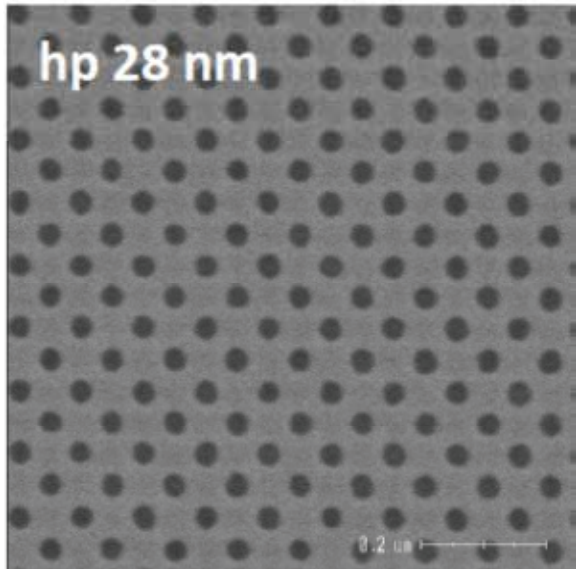


Fig. 7. 28-nm-hole pattern of the inorganic resist using EUV-IL.

The reduction of the vibration amplitude from a dry pump is a significant factor for the resist patterning of a small feature size in the EUV-IL exposure. The displacement of the vibration amplitude between the transmission diffraction grating and the wafer should be reduced to approximately 1/3 of the target resolution of 10 nm in EUV-IL [10]. In order to reduce the vibration, the high-rigidity trestle and low-vibration-dry-pumping system are employed adapted to the EUV-IL exposure chamber. The relative-vibration-amplitude spectra between TDG and wafer using the conventional air-spring bench and novel higher weight bench are shown in Fig. 8, and the relative-vibration amplitude suppressed to be less than 1 nm which is enough for the 10 nm patterning.

As the results, it is now ready to evaluate the resolution of 10 nm using EUV-IL at NewSUBARU [11].

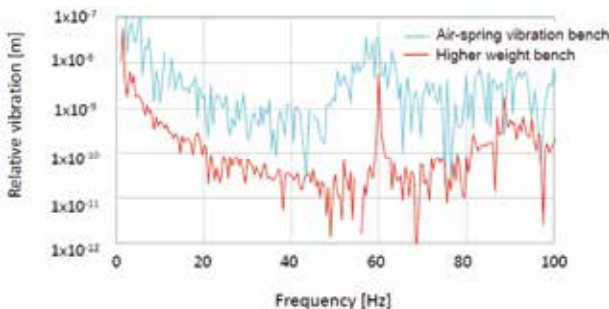


Fig.8. Relative-vibration-amplitude spectra between TDG and wafer using the conventional air-spring bench and novel higher weight bench

### 3.2 EUV resist chemical reaction analysis using X-ray absorption fine structure (XAFS)

The EUV resist technical issue is to achieve the high resolution, high sensitivity, low line-edge-roughness (LWR), and low outgassing. Since there is a trade-off relationship between the resolution, sensitivity, and LWR, the simultaneous achievement of the requirement has a difficulty. In this situation, the high sensitivity achievement has the highest priority, because the most significant issue of the EUV lithography is the achievement of the high power EUV source to maintain the wafer throughput for HVM. If the high sensitive EUV resist will achieve, it might be relaxing the requirement of the power of the EUV light source. In order to achieve high sensitivity of the EUV resist, the chemical reaction analysis using real EUV light is significant. In general, the content of the photosensitizing agent such as a photoacid generator (PAG) in the EUV chemically amplified resist [12-14] material is approximately from 10 to 15% of the base resin. In order to analysis of the cation and anion of PAG, the conventional analysis methods such as XPS, FT-IR, and Raman spectroscopy have not enough sensitivity for the analysis of the chemical reaction analysis of the EUV resist. Thus we applied x-ray absorption fine structure (XAFS) method for the chemical reaction analysis of the EUV resist material. In this method, the total electron yield method is used for the analysis of the chemical reaction, because this method is very sensitive even if the content of PAG is small.

Since it is found that the decomposition reaction of the fluorine which consist of the onium salts employed as a PAG is significant in the previous study [15-17], we increase the detection sensitivity in the TEY method by

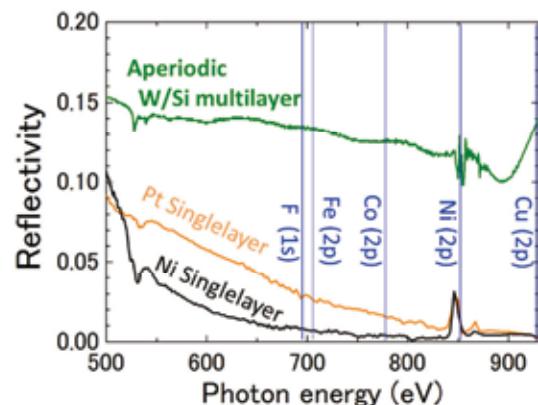


Fig.9. Reflectivity comparison of the wideband W/Si-multilayer, the Ni single-layer, the Pt single-layer samples.

refinement of the monochromator at the BL10 beamline. The W/Si aperiodic multilayer coated grating is employed for the monochromator to extend the photon energy region from 500 to

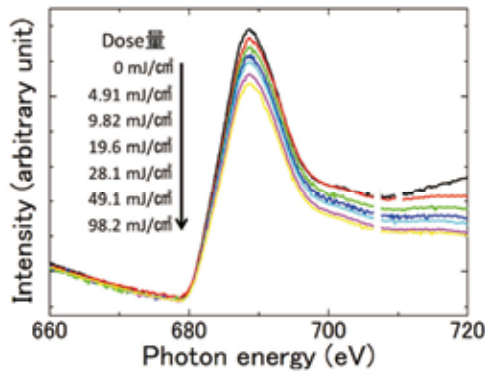


Fig.10. TEY-XAFS measurement result of the resist at fluorine absorption edge.

1100 eV as shown in Fig. 9 [18]. As the results, the absorption peak signal of the fluorine 1s core level can be measured clearly as shown in Fig. 10. As the results of the TEY-XAFS analysis applied to the EUV CA resist, it is found that to satisfy the specification of the EUV resist which require for high volume manufacturing, all the chemical reaction should be taken in account, such as the ionization and the direct excitation reactions, as shown in Fig.11. Increasing the sensitivity, it might have more space to achieve the low LWR resist [17].

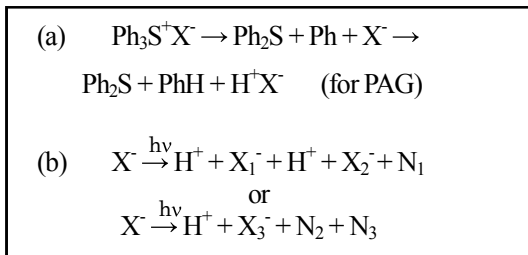


Fig. 11. (a) The decomposition reaction by the secondary electron generated from the ionization reaction and (b) the decomposition reaction of the anion of PAG by the direct excitation reaction under EUV irradiation. Where  $\text{N}_1$ ,  $\text{N}_2$ , and  $\text{N}_3$  are non-ionic species which were generated in those chemical reactions.

## 4. Mask Defect Inspection System

### 4.1 EUV microscope

An EUV mask is a reflective type, which is fundamentally different from DUV lithography. It consists absorber layer, reflective multilayer, and glass substrate. Bump and pit on the glass

substrates and particle in the multilayer modulate reflection phase of EUV, which are printed as defects. This kind of defect is called phase defect. Actinic inspection is required to evaluate printability of the phase defect. Therefore, we have developed the EUV microscopes for actinic mask observation at BL3 beamline of NewSUBARU. The first system of the EUV microscope consists Schwarzschild objective and an electron zooming tube [19]. Phase defect printability was firstly investigated. And, capability of defect hide by an absorber pattern was demonstrated.

The second EUV-microscope system was developed with Tohoku University and EIDEC. The optical layout is shown in Fig. 12 [20]. The mask sample was illuminated by a synchrotron radiation at an incident angle of  $13^\circ$ . Its objective was configured as a two-stage imaging system that formed a high magnification ( $1470\times$ ) image on its CCD camera. At first, Schwarzschild objective formed a mask pattern image on the intermediate position with low magnification of  $30\times$ , which had numerical aperture (NA) of 0.25. At second, this intermediate image was magnified ( $49\times$ ) by a concave mirror of M6. The expected spatial resolution is higher than 30 nm. And expected field of view is very large of  $160\ \mu\text{m}$  diameter.

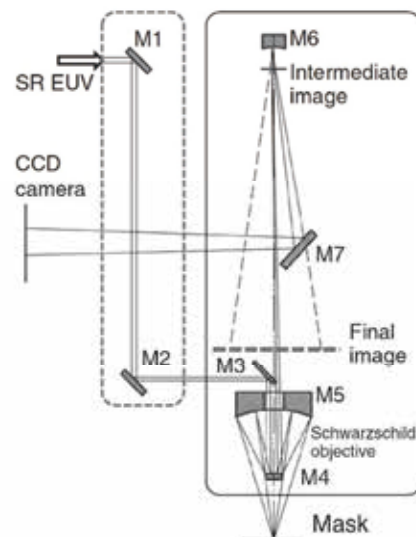


Fig. 12. Schematics of an EUV microscope, which consists of illumination optics and an imaging optics.

Figure 13 shows bright-field EUV images of test patterns with (a) 40 nm and (b) 30 nm half pitches. Image contrast of 0.3 was achieved at 30-nm half-pitch pattern, which was corresponded to 7.5-nm half-pitch pattern at the wafer position. This result demonstrated very high resolution of the EUV microscope.

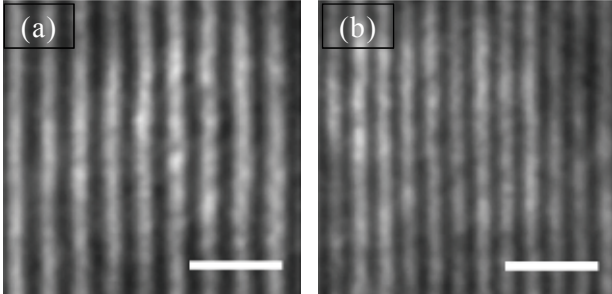


Fig. 13. Bright-field EUV images of the fine grating patterns: (a) 40, and (b) 30 nm half-pitch patterns. The bar indicates a length of 200 nm.

Figure 14 shows EUV-microscope images of 88-nm L/S pattern with the phase defects [21], which position was varied in the line. Variation of EUV reflectivity loss by the phase defect was clearly observed in the intensity profile. This result shows the high capability of the EUV microscope to pinpoint the actual position and affected area by the phase defect.

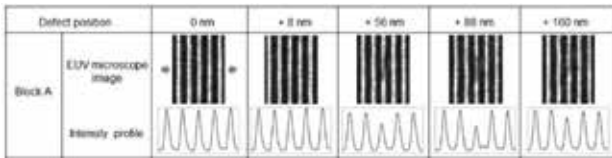


Fig. 14. EUV microscope images and intensity profiles of the 88-nm L/S with phase defect.

#### 4.2 Micro coherent EUV scatterometry microscope

An EUV mask has 3-dimensional (3D) structure for EUV wavelength, which is reflective type and consists of glass substrate, reflective Mo/Si multilayer, and absorber pattern. Since the 3D structure affects the reflective phase, a phase-imaging microscope of the EUV mask is important for EUV mask development.

At BL10 beamline, we have developed a lensless EUV microscope of micro coherent EUV scatterometry microscope (micro-CSM) to observe defects with quantitative phase contrast. Micro-CSM is simple lensless microscope based on the coherent diffraction

imaging method. The micro-CSM records diffraction from the defect directly. The defect image is reconstructed by iterative calculation.

Figure 15 shows the schematic layout of micro-CSM system [22]. The coherent EUV illumination was focused on the mask using a Fresnel zoneplate (FZP). The effective NA of the FZP was about 0.08. The angle of incidence of the main focused EUV ray was approximately  $6.8^\circ$ , which was similar to the angle of the EUV scanner ( $6.0^\circ$ ). The estimated focused size was about 140 nm, and a CCD camera was used to record the diffraction patterns from the defects. The NA of the micro-CSM system was approximately 0.27. The expected spatial resolution was 30 nm.

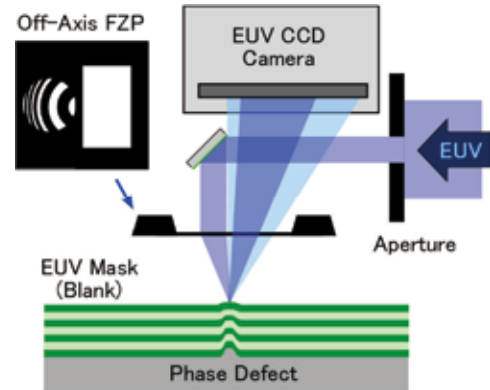


Fig. 15. Schematic view of micro-CSM system.

We observed actual defects on an EUV mask, which were already inspected with the actinic blank inspection tool [23]. Figure 16 shows the observation result of (a) AFM and (b)(c) micro-CSM, respectively. This defect was a hole-type phase defect with an area of  $67 \times 57 \text{ nm}^2$ . We successfully reconstructed the actual defect image with 30-nm spatial resolution, and quantitative intensity and phase contrast. The defect shape was reconstructed as a point shape, which was expected from the AFM image. This aberration-free micro-CSM images with

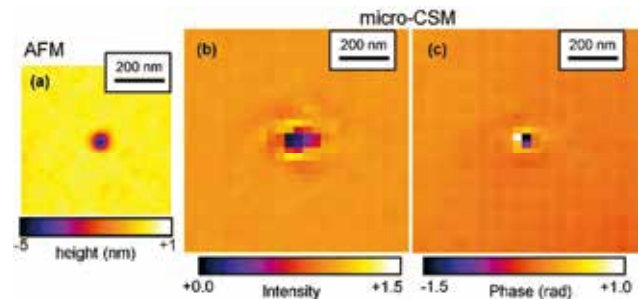


Fig. 16. The observation results of an actual defect. (a) AFM results, (b) (c) the images reconstructed by micro-CSM in intensity and phase contrast, respectively. The three panels have the same spatial scale.

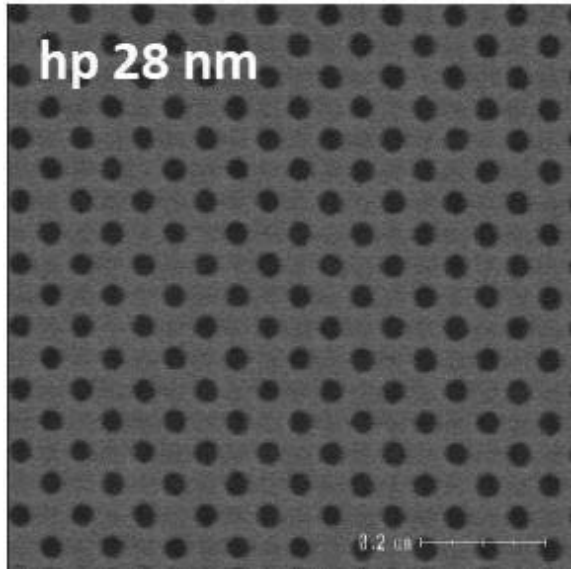


Fig. 7. 28-nm-hole pattern of the inorganic resist using EUV-IL.

employed adapted to the EUV-IL exposure chamber. The relative-vibration-amplitude spectra between TDG and wafer using the conventional air-spring bench and novel higher weight bench are shown in Fig. 8, and the relative-vibration amplitude suppressed to be less than 1 nm which is enough for the 10 nm patterning.

As the results, it is now ready to evaluate the resolution of 10 nm using EUV-IL at NewSUBARU [11].

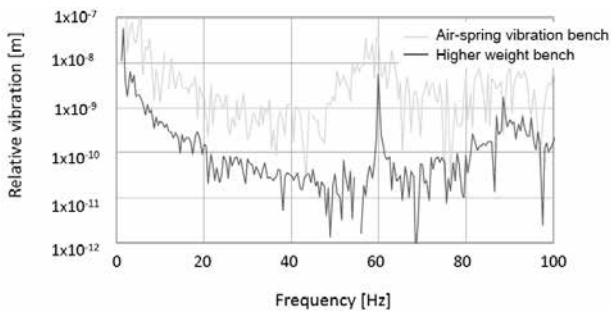


Fig.8. Relative-vibration-amplitude spectra between TDG and wafer using the conventional air-spring bench and novel higher weight bench.

### 3.2 EUV resist chemical reaction analysis using X-ray absorption fine structure (XAFS)

The EUV resist technical issue is to achieve the high resolution, high sensitivity, low line-edge-roughness (LWR), and low outgassing. Since there is a trade-off relationship between the resolution, sensitivity, and LWR, the simultaneous achievement of the requirement

has a difficulty. In this situation, the high sensitivity achievement has the highest priority, because the most significant issue of the EUV lithography is the achievement of the high power EUV source to maintain the wafer throughput for HVM. If the high sensitive EUV resist will achieve, it might be relaxing the requirement of the power of the EUV light source. In order to achieve high sensitivity of the EUV resist, the chemical reaction analysis using real EUV light is significant. In general, the content of the photosensitizing agent such as a photoacid generator (PAG) in the EUV chemically amplified resist [12-14] material is approximately from 10 to 15% of the base resin. In order to analysis of the cation and anion of PAG, the conventional analysis methods such as XPS, FT-IR, and Raman spectroscopy have not enough sensitivity for the analysis of the chemical reaction analysis of the EUV resist. Thus we applied x-ray absorption fine structure (XAFS) method for the chemical reaction analysis of the EUV resist material. In this method, the total electron yield method is used for the analysis of the chemical reaction, because this method is very sensitive even if the content of PAG is small.

Since it is found that the decomposition reaction of the fluorine which consist of the onium salts employed as a PAG is significant in the previous study [15-17], we increase the detection sensitivity in the TEY method by refinement of the monochromator at the BL10 beamline. The W/Si aperiodic multilayer coated grating is employed for the monochromator to extend the photon energy region from 500 to 1100 eV as shown in Fig. 9 [18]. As the results,

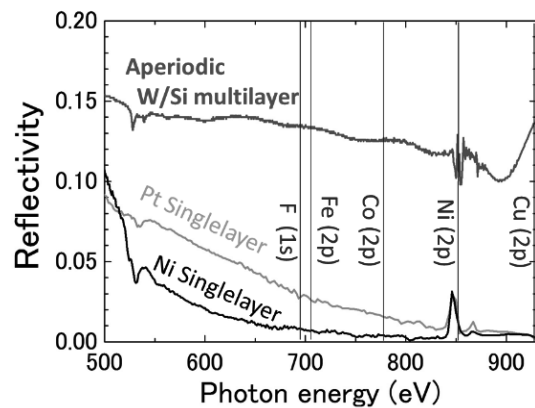


Fig.9. Reflectivity comparison of the wideband W/Si-multilayer, the Ni single-layer, the Pt single-layer samples.

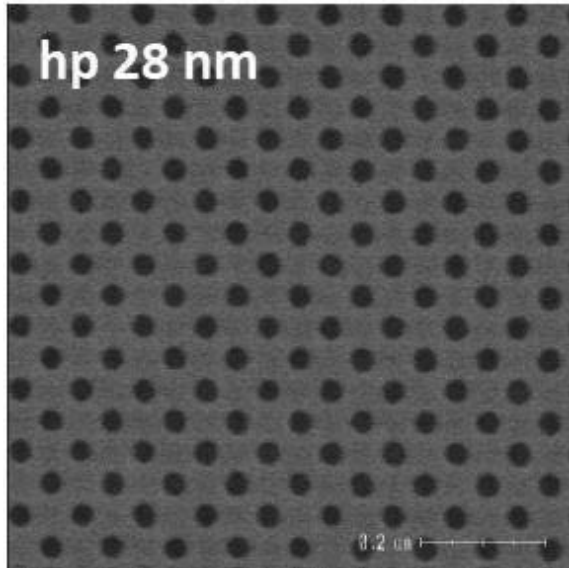


Fig. 7. 28-nm-hole pattern of the inorganic resist using EUV-IL.

employed adapted to the EUV-IL exposure chamber. The relative-vibration-amplitude spectra between TDG and wafer using the conventional air-spring bench and novel higher weight bench are shown in Fig. 8, and the relative-vibration amplitude suppressed to be less than 1 nm which is enough for the 10 nm patterning.

As the results, it is now ready to evaluate the resolution of 10 nm using EUV-IL at NewSUBARU [11].

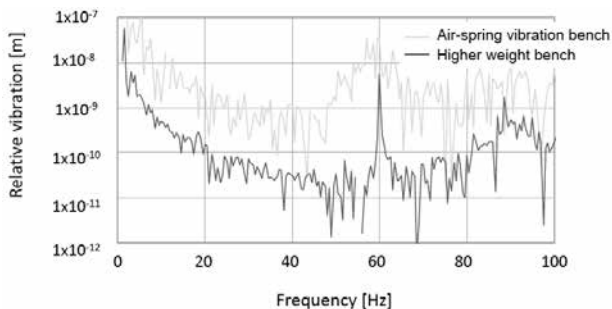


Fig.8. Relative-vibration-amplitude spectra between TDG and wafer using the conventional air-spring bench and novel higher weight bench.

### 3.2 EUV resist chemical reaction analysis using X-ray absorption fine structure (XAFS)

The EUV resist technical issue is to achieve the high resolution, high sensitivity, low line-edge-roughness (LWR), and low outgassing. Since there is a trade-off relationship between the resolution, sensitivity, and LWR, the simultaneous achievement of the requirement

has a difficulty. In this situation, the high sensitivity achievement has the highest priority, because the most significant issue of the EUV lithography is the achievement of the high power EUV source to maintain the wafer throughput for HVM. If the high sensitive EUV resist will achieve, it might be relaxing the requirement of the power of the EUV light source. In order to achieve high sensitivity of the EUV resist, the chemical reaction analysis using real EUV light is significant. In general, the content of the photosensitizing agent such as a photoacid generator (PAG) in the EUV chemically amplified resist [12-14] material is approximately from 10 to 15% of the base resin. In order to analysis of the cation and anion of PAG, the conventional analysis methods such as XPS, FT-IR, and Raman spectroscopy have not enough sensitivity for the analysis of the chemical reaction analysis of the EUV resist. Thus we applied x-ray absorption fine structure (XAFS) method for the chemical reaction analysis of the EUV resist material. In this method, the total electron yield method is used for the analysis of the chemical reaction, because this method is very sensitive even if the content of PAG is small.

Since it is found that the decomposition reaction of the fluorine which consist of the onium salts employed as a PAG is significant in the previous study [15-17], we increase the detection sensitivity in the TEY method by refinement of the monochromator at the BL10 beamline. The W/Si aperiodic multilayer coated grating is employed for the monochromator to extend the photon energy region from 500 to 1100 eV as shown in Fig. 9 [18]. As the results,

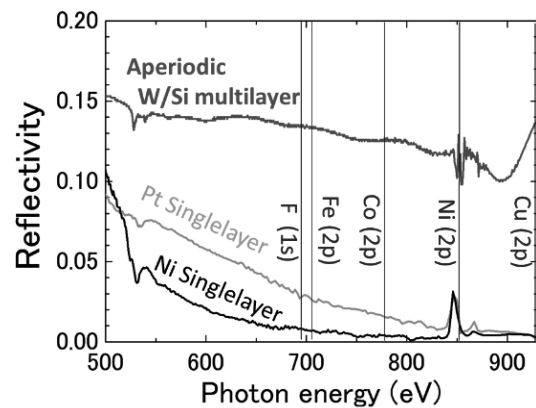


Fig.9. Reflectivity comparison of the wideband W/Si-multilayer, the Ni single-layer, the Pt single-layer samples.

# Oxidation of mechanically ground *h*-BN

Yoshida Keigo and Yasuji Muramatsu  
Graduate School of Engineering, University of Hyogo

## Abstract

Oxidation of mechanically ground hexagonal boron nitride (*h*-BN) was determined from XANES measurements in BL10/NewSUBARU and theoretical XANES analysis by using the discrete variational (DV) - $X\alpha$  method. By the mechanical grinding (MG), the  $\pi^*$  peak at 192 eV in *h*-BN drastically decreased, and three peaks were appeared in the MG-*h*-BN. However, in the 240-h milling with 20 balls, only the 194 eV peak which is corresponding to the  $\pi^*$  peak of  $B_2O_3$  remained. This shows the final product of MG-*h*-BN is  $B_2O_3$ . Theoretical analysis indicates that the three peaks are assigned to the partially oxidized boron  $BO_x$  ( $x=1\sim 3$ ) states.

## Introduction

Mechanical alloying (MA) method has been used for alloying in non-equilibrium states. Thus, unstable products may often be synthesized by MA. For example, in MA of *h*-BN and graphite, B-N bonds were broken and B-O bonds were formed under atmospheric air [1]. This suggested that MA of *h*-BN provides B radicals under anaerobic atmosphere, and the B radicals easily react with oxygen to form boron oxides.

In the present study, to clarify the oxidation reaction of B radicals formed by the mechanical grinding (MG) of *h*-BN, XANES of MG product of *h*-BN exposed to atmospheric air were measured in BL10/NewSUBARU. Oxidized structures of the MG-*h*-BN were analyzed by the theoretical method.

## Experiments

The commercially available *h*-BN powders were put in a stainless steel (SUS) vessel (40 mm $\phi$  x 65 mm $^L$ ) with SUS balls (10 mm $\phi$ ) under argon atmosphere. The number of balls was varied as 10 or 20. The vessel containing the *h*-BN powders with balls was set in a MA machine (8000M, SPEC CertiPrep), and mechanically ground for up to 240 h. After the MG reactions, the MG-*h*-BN powders were slowly exposed to the atmosphere. The MG-*h*-BN powders were pressed and hold on indium substrates for XANES measurements.

XANES measurements were performed in an X-ray absorption spectroscopy (XAS) station [2] in the BL10 at New SUBARU. XANES in the BK, CK, NK, and OK regions of MG-*h*-BN were obtained by a total-electron-yield (TEY) method.

For XANES analysis, density of state (DOS) of probable B/N/O cluster models was calculate with the discrete variational (DV) - $X\alpha$  method [3].

## Results and Discussion

Figure 1 shows the XAS spectra in the 180-620 eV region of the MG-*h*-BN and reference compounds of *h*-BN and  $B_2O_3$ . MG-*h*-BN samples exhibit BK, NK, and OK absorption peaks. Oxidation of *h*-BN by MG can therefore be confirmed from the OK absorption peaks. As the MG reaction proceeds, NK absorption peaks become lower. Especially, MG-*h*-BN milled for 240 h with 20 balls exhibit little NK peak. Hence, *h*-BN can be completely milled and nitrogen can be thoroughly eliminated by the MG condition.

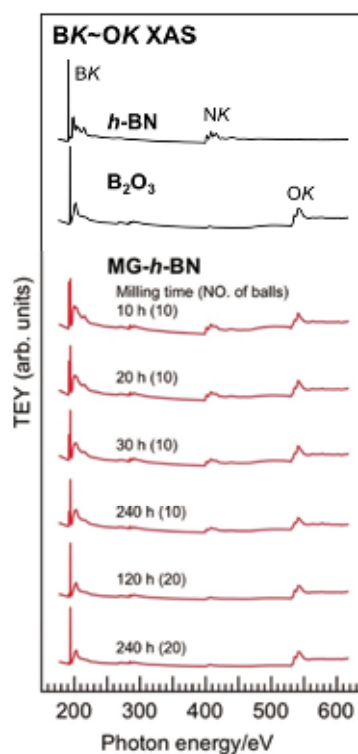


**Fig. 1** XAS spectra of MG-*h*-BN and reference *h*-BN and  $B_2O_3$ .

Figure 2 shows the BK-XANES of the

MG-*h*-BN and the references. In the early stage of the MG reaction, three satellite peaks were observed at 192.7 eV (denoted as *a*), 193.2 eV (*b*) and 194 eV (*c*) in the higher energy side of  $\pi^*$  peak at 192 eV). It should be noticed that the peak *c* corresponds to the  $\pi^*$  peak of  $B_2O_3$ .

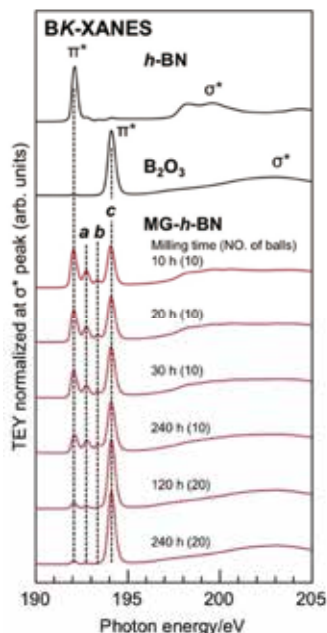


**Fig. 2** BK-XANES of MG-*h*-BN and reference *h*-BN and  $B_2O_3$ .

Figure 3 shows the peak heights of the  $\pi^*$  peak and satellite peaks as the function of MG time. In the final stage of the MG reactions, the  $\pi^*$  peak of *h*-BN and satellite peaks *a* and *b* were disappeared, while only satellite peak *c* was enhanced. Hence, it can be confirmed that the final product of MG-*h*-BN is  $B_2O_3$  and the satellites *a* and *b* suggest the intermediates of boron oxides.

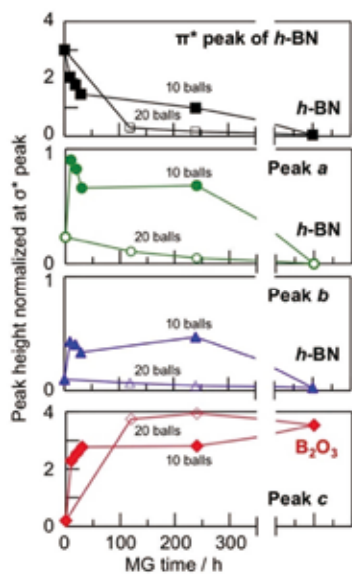


**Fig. 3** Peak intensities of the  $\pi^*$  peak of *h*-BN,

and satellite peaks *a* ~ *c* as the function of MG time.

To assign the satellite peaks, DOS of oxidized BN cluster models,  $B_{48}N_{48-x}O_xH_{24}$  ( $x=0\sim 3$ ), were calculated with the DV- $X\alpha$  method. In the cluster models, O atoms substituted for N atoms around the center B atom. Figure 4 shows the cluster models (*h*-BN model and O-substitutional models) and their unoccupied B2p- and 2s-DOS. The  $\pi^*$  peak of the center B atom in the  $B_{48}N_{48}H_{24}$  model exhibits higher-energy shifts as the B-O bond formations. The calculated  $\pi^*$  peak shifts are corresponding to the measured satellite peaks *a* ~ *c*. Therefore, the satellites can be assigned; the satellite *a* can be assigned to the BO, satellite *b* to the  $BO_2$ , and satellite *c* to be  $BO_3$  in the trigonal B configuration. In conclusion, *h*-BN can be gradually oxidized by MG reaction and the final product is  $B_2O_3$ .

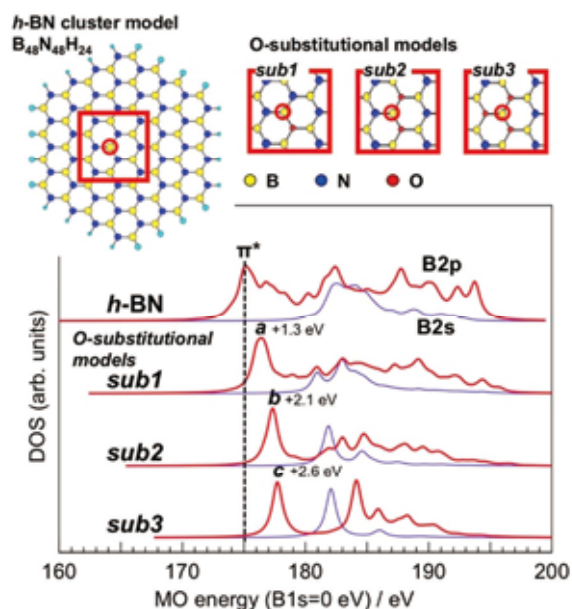


**Fig. 4** Upper panel shows the oxidized BN cluster models (*h*-BN, O-substitutional models; *sub1*~*sub3*) of  $B_{48}N_{48-x}O_xH_{24}$  ( $x=0\sim 3$ ). Lower shows the unoccupied B2p- and B2s-DOS of the cluster models.

## References

- [1] Y. Muramatsu, S. Kashiwai, T. Kaneyoshi, H. Kouzuki, M. Motoyama, M. M. Grush, T. A. Callcott, J. H. Underwood, E. M. Gullikson, and R. C. C. Perera, ALS Compendium of User Abstracts and Technical Reports, 1993-1996, 47 (1997).
- [2] Y. Muramatsu, A. Tsueda, T. Uemura, K. Nambu, T. Ouchi, T. Harada, T. Watanabe, and H. Kinoshita, LASTI Annual Report, **17**, 27-28 (2015).

[3] H. Adachi, M. Tsukada, and C. Satoko, J. Phys. Soc. Jpn., **45**, 875-883 (1978).

# XANES of fullerenes ( $C_{60}$ , $C_{70}$ ) simulated by CASTEP

Yuma Hirai and Yasuji Muramatsu  
Graduate School of Engineering, University of Hyogo

## Abstract

To discuss the electronic structure of pentagonal rings in hexagonal carbon layers, C  $K$  XANES of fullerenes ( $C_{60}$  and  $C_{70}$ ) were measured in BL10/NewSUBARU and the XANES profiles were theoretically simulated and discussed by the first principle calculations. C  $K$  XANES of them were successfully simulated by CASTEP, and the fine structures can be assigned from the density of state (DOS). It can be confirmed that the  $\pi^*$  peak splits into several peaks reflecting the symmetry which depends on the local structure around pentagonal rings.

## 1. Introduction

X-ray absorption near-edge structure (XANES) is a powerful tool for local structure and electronic structure analyses. However, to clarify them from XANES, theoretical analysis should be required to assign the peak structure in XANES. Recently, the first principle calculation method of CASTEP [1] has been applied for XANES simulations.

In the present study, to demonstrate the capability of CASTEP for XANES simulations of large carbon molecules, XANES of fullerenes ( $C_{60}$  and  $C_{70}$ ) were measured in BL10/NewSUBARU and simulated by CASTEP. Additionally, fine structures of their XANES were discussed, referring to the density of state (DOS) calculated by the DV- $X\alpha$  molecular orbital method [2].

## 2. XANES measurements and calculations

Commercially available powder samples of  $C_{60}$  and  $C_{70}$  were pressed and held on an indium substrate and used as XANES measurement sample. C  $K$ -XANES of them was measured in BL10 at NewSUBARU by using a total-electron-yield (TEY) method.

In the simulation of XANES by CASTEP, each molecular model was put in the center of a supercell. In order to suppress intermolecular interaction, the distance between the supercell boundaries and the molecular model was set to longer than 5 Å. After the structure optimization by Material Studio package, ground-state calculations were performed. Then, excited-state calculations were carried out by providing core hole in the 1s orbital of the target atom. Transition energy was corrected by the Mizoguchi method [3]. XANES of individual carbon atoms was calculated, and calculated XANES of a molecule was obtained by summing up the XANES of individual atoms. To assign the peak structure of XANES, unoccupied DOS was also calculated by the DV- $X\alpha$  method.

## 3. Results and Discussion

Fig. 1 shows the measured C  $K$  XANES compared to the calculated XANES and the unoccupied DOS of  $C_{60}$ . The measured C  $K$  XANES which exhibits eight peaks (denoted by  $a \sim h$ ) agrees to the previously

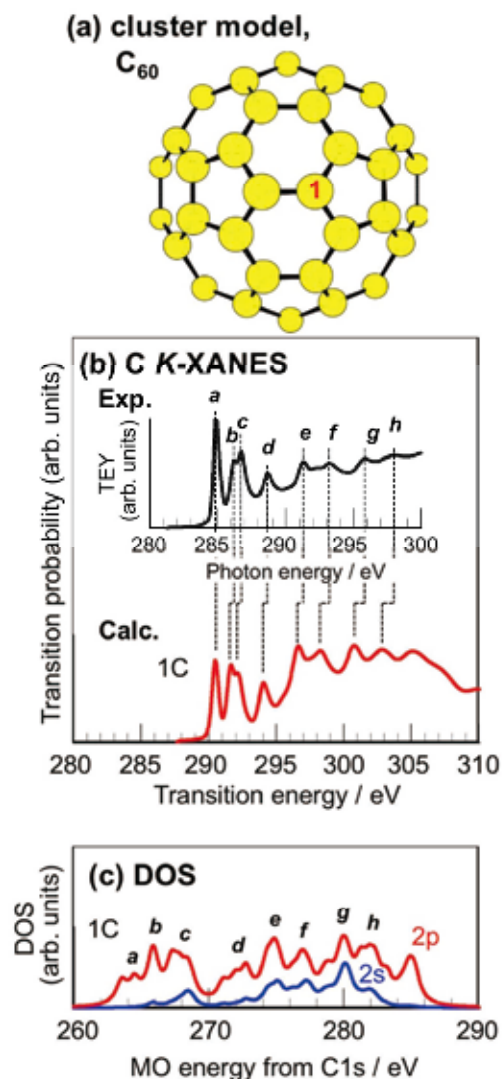


**Fig. 1** Cluster mode or  $C_{60}$  (a), the measured and calculated C  $K$ -XANES of  $C_{60}$  (b), and the

unoccupied DOS of  $C_{60}$  (c). measured spectrum [4]. The peak structure can be well reproduced by the calculated XANES. The unoccupied  $C2p$ - and  $C2s$ -DOS exhibits broader structure than the calculated XANES. However, the broad  $C2p$ -DOS peaks can approximately correspond to the peak  $a \sim h$ . Only peak  $a$  consists of  $2p$ -state. Thus, peak  $a$  can be assigned to a  $\pi^*$  peak. It should be noted that the lowest peak of  $a$  is at 284.8 eV, which is lower than the 285.5 eV  $\pi^*$  peak of graphite. Each carbon atom in  $C_{60}$  is shared by two hexagonal ring and one pentagonal ring. Therefore, the pentagonal ring results in the low energy shift of the  $\pi^*$  peak. Peaks  $b \sim h$  consist of hybridizes states with  $2p$ - and  $2s$ -orbitals. Contribution of  $2s$ -orbital in peaks  $b$  and  $c$  may reflect the non-planar structure formed by pentagonal rings in hexagonal rings.

Figure 2 shows the measured  $C K$  XANES compared to the calculated XANES and the unoccupied DOS of  $C_{70}$ . The measured  $C K$  XANES which exhibits nine peaks (denoted by  $a \sim i$ ) agrees to the previously measured spectrum [4].  $C_{70}$  consists of five different carbon atoms due to the symmetry, as labelled by  $1 \sim 5$  in the cluster model. The calculated XANES of each five carbon atom was obtained, and summing them provides XANES of  $C_{70}$  molecule. The measured XANES profile can be well reproduced by the calculated XANES. Atoms  $C1$  and  $C5$ , which are shared by hexagonal rings, exhibit peak  $b$  at 285.5 eV. Atoms  $C2 \sim C4$ , which are shared by two hexagonal rings and one pentagonal ring, exhibit peaks  $a$  and  $c$ . Such the peak assignments approximately agree to the DOS distribution. The peak profile of  $C2 \sim C4$  indicates that the carbon atom shared by pentagonal and hexagonal rings split the  $\pi^*$  peak, which is consistent to the peak profile of  $C_{60}$ .

Such the spectral analysis of  $C_{60}$  and  $C_{70}$  indicates that the  $\pi^*$  peak in  $C K$  XANES of carbon atoms partially shared with pentagonal is split into two peaks. This means that the pentagonal ring makes the  $\pi^*$  peak splitting around 285.5 eV.

## Reference

- [1] S. J. Clark, M. D. Segall, C. J. Pickard, P. J. Probert, K. Refson, M. C. Z. Payne, *Krystalloger.*, 220, 567-570 (2005).
- [2] H. Adachi, M. Tsukada, and C. Satoko, *J. Phys. Soc. Jpn.* 45, 875-883 (1978).
- [3] T. Mizoguchi, I. Tanaka, S.-P. Gao, C. J. J. Pickard, *Phys. Condens. Mat.*, 21, 104204 (2009).

- [4] L. J. Terminello, D. K. Shuh, F. J. Himpsel, D. A. Lapiano-Smith, J. Stöhr, D. S. Bethune, and G. Meijer, *Chem. Phys. Lett.*, 182, 491-496 8(1991).

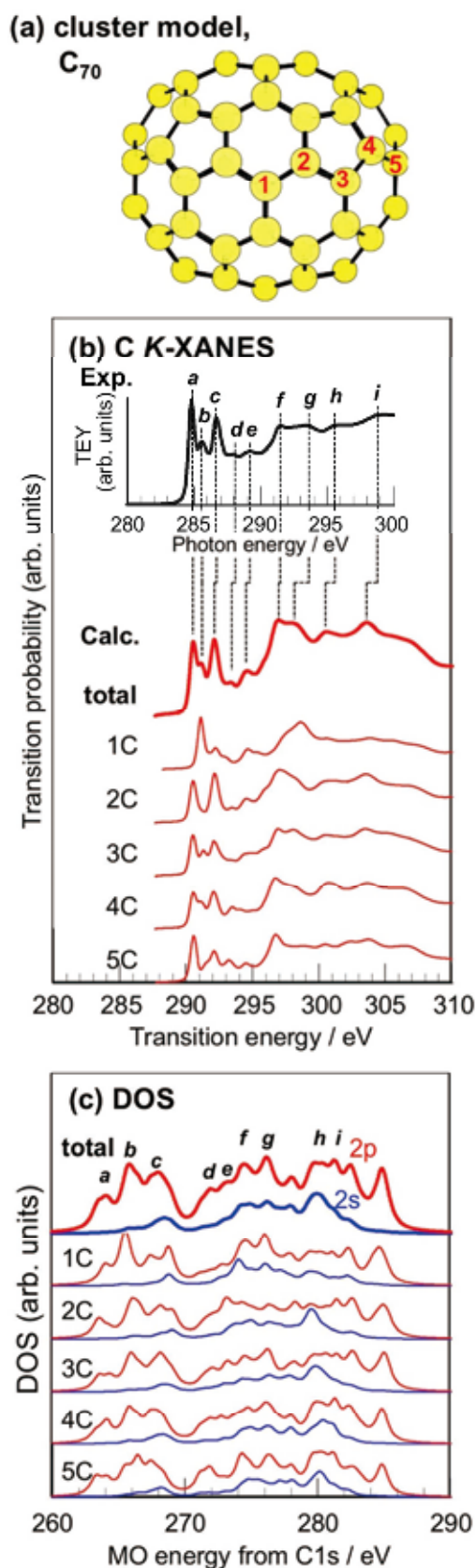


**Fig. 2** Cluster mode of C<sub>60</sub> (a), the measured and calculated C *K*-XANES of C<sub>60</sub> (b), and the unoccupied DOS of C<sub>60</sub> (c).

# Soft X-ray analyses of detonation nanodiamonds to investigate surface $sp^2$ carbon for the dispersibility improvement

Masahiro Nishikawa<sup>1</sup>, Ming Liu<sup>1</sup>, and Yasuji Muramatsu<sup>2</sup>

<sup>1</sup> Daicel Corporation, <sup>2</sup> University of Hyogo

## Abstract

Gas-phase (air) oxidation is the most promising avenue for the dispersibility improvement of detonation nanodiamonds (DND) in water or polar solvents. To elucidate oxidation mechanism, we conducted X-ray absorption near edge structure (XANES) measurements at BL-10 in the NewSUBARU SR facility. We found that the increase of edge carbon on  $sp^2$  cluster was the key to increase oxygen functional groups on the surface, not increase of  $sp^2$  carbon content.

## Introduction

Dispersibility is the key to utilize detonation nanodiamonds (DND) for various applications. We have reported that gas-phase (air) oxidation of detonation nanodiamonds (DND) is one of the powerful tools to improve dispersibility in water or polar solvents. It can be thought that it is because oxygen functional groups on the surface increase by oxidation [1]. To elucidate the oxidation mechanism, we investigated the amount and state of  $sp^2$  carbon on the surface of DND samples obtained by different oxidation conditions using soft X-ray near-edge structure (XANES).

## Experiments

XANES measurements were carried out at BL-10 [2] in the NewSUBARU SR facility. CK-edge and OK-edge XANES were recorded by the total electron yield (TEY) method.

DND raw material for gas-phase oxidation was manufactured by Daicel Corporation, of which average primary particle diameter was determined 4.5 nm according to Sherrer's equation by HMFW of the 111 peak of powder X-ray diffraction analysis. Gas-phase oxidation were performed by atmosphere furnace with the flow of 4% oxygen-nitrogen gas at different temperatures between 250 and 450°C. All oxidized DNDs by above conditions were well dispersed in water by bead-milling process [1].

## Results and Discussion

### i) Content of $sp^2$ carbon

CK-edge XANES spectra of oxidized DND samples are shown in Fig.1. We estimated  $sp^2$  carbon content from the peak height ratio of  $\pi^*$ (285 eV)/ $\sigma^*$ (293 eV) and found that the amount of  $sp^2$  carbon was almost the same as that of the untreated DND up to 400°C. When

the temperature was raised to 450°C,  $sp^2$  carbon content increased. It can be presumed that part of  $sp^3$  carbon phase changed to  $sp^2$  carbon at that temperature.

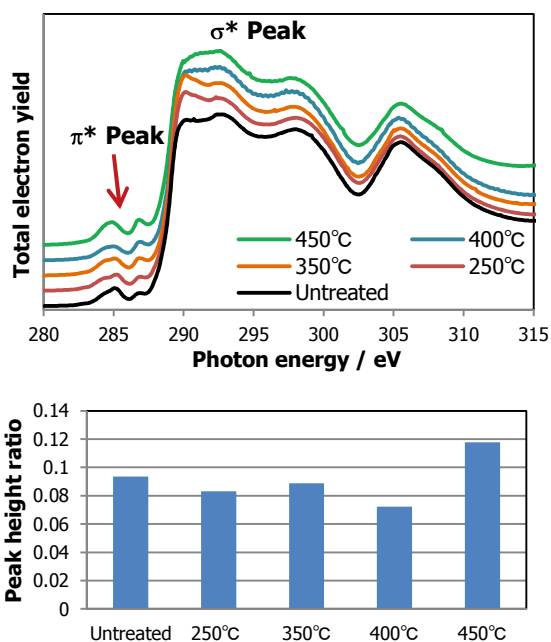


**Fig. 1** CK-edge XANES spectra of gas-phase oxidized DND at various temperatures (upper) and  $sp^2$  carbon content estimation from the peak height ratio of  $\pi^*/\sigma^*$  (lower)

### ii) Edge carbon proportion

It was found that  $\pi^*$  peak for each sample had a shoulder at about 284.5 eV (Fig. 2), which had been attributed to edge carbon of  $sp^2$  cluster [3]. To estimate the proportion of that shoulder peak, differential spectrum between DND sample and HOPG (Highly Oriented Pyrolytic Graphite), normalized at  $\pi^*$  peak, was

obtained. That differential spectrum is called “pre-peak”. We compared the peak height of each sample and found that pre-peak height increased as the temperature rose. We deduced that the proportion of edge carbon increased with  $sp^2$  clusters broken-up into small fragments.

Peak at 287 eV, which had been assigned to  $sp^2$  carbon bound to oxygen functional group [3], also increased as the temperature was raised. That supported the hypothesis that oxygen functional groups increased by the oxidation.

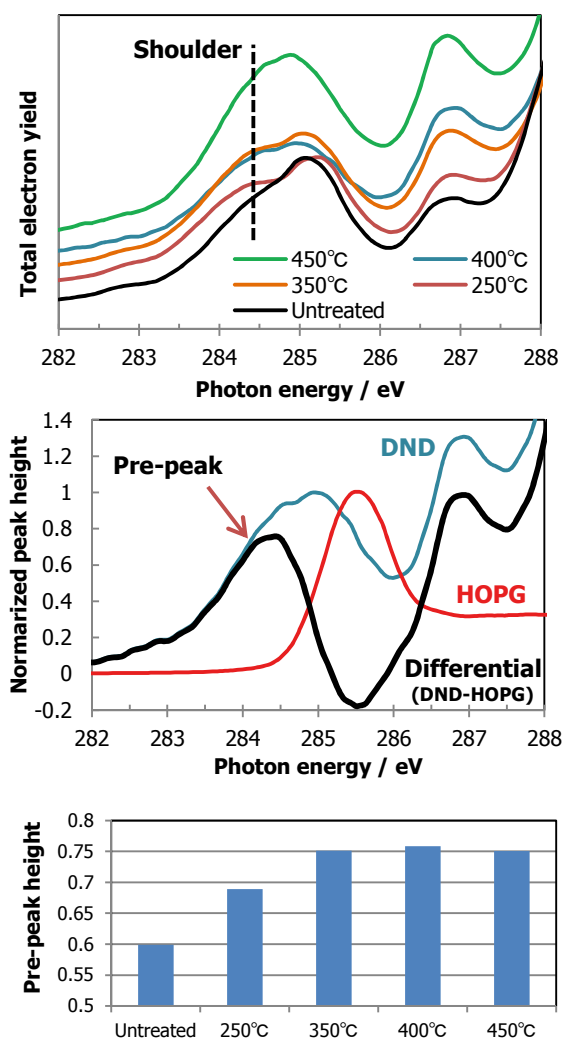


**Fig. 2** CK-edge XANES spectra of  $\pi^*$  peak region of oxidized DND (upper), the differential spectrum (black line, middle) and pre-peak height of each sample (lower)

### iii) OK-edge XANES

OK-edge XANES analyses were also conducted (Fig. 3). Peak height normalized at  $\sigma^*$  peak of CK-edge XANES increased with the treatment temperature raise, indicating that

oxygen functional groups increased by the oxidation. That agrees with the results for the peak at 287 eV of CK-edge XANES.

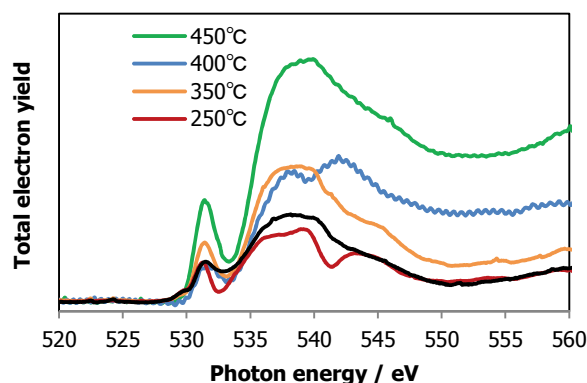


**Fig. 3** OK-edge XANES spectra of gas-phase oxidized DND at various temperatures, normalized at 293 eV ( $\sigma^*$ ) of CK-edge XANES

### iv) Oxidation mechanism

We concluded that the increase of oxygen functional group for the dispersibility improvement may occur as the following;

- Oxidation process broke-up  $sp^2$  carbon clusters into small fractions that increased edge carbon proportion, not  $sp^2$  carbon content.
- The edge carbon was subsequently oxidized with oxygen to increase oxygen functional groups.

### References

[1] M. Liu, A. Kume, M. Nishikawa, H. Ito, *10th International Conference on New Diamond and Nano Carbons Xi'an, China*, p6-14 (2016).  
 [2] T. Uemura, Y. Muramatsu, K. Nambu, D. Fukuyama, M. Kuki, T. Harada, T. Watanabe, and H. Kinoshita, *Adv. X-ray Chem. Anal., Japan*, **46**, 317-325 (2015).  
 [3] K. Murayama, T. Okada, Y. Muramatsu, *10th International Symposium on Atomic Level Characterizations for New Materials and Devices '15 Shimane, Japan*, 27p-P-38 (2015).

# Deterioration and Depth-Profile Analyses of Organic Thin Film

Shogo Suehiro<sup>1</sup>, Eiji Takahashi<sup>1</sup>, Yousuke Azuma<sup>1</sup>,  
Yasuko Mitsushita<sup>1</sup>, Yasuji Muramatsu<sup>2</sup>, and Yoshiyuki Suzuri<sup>3</sup>

<sup>1</sup> Sumika Chemical Analysis Service, Ltd.,  
1-135, Kasugade-Naka 3-chome, Konohana-ku, Osaka 554-0022, Japan

<sup>2</sup> Graduate School of Engineering, University of Hyogo,  
2167, Shosha, Himeji, Hyogo 671-2280 Japan

<sup>3</sup> Innovation Center for Organic Electronics, Yamagata University,  
1-808-48 Arcadia, Yonezawa, Yamagata 992-0119 Japan

## Abstract

The manufacturing process affects the performance of devices consisted of multilayer organic thin films such as organic electroluminescent (OEL) devices. We conducted the deterioration and the depth-profile analyses of B3PyMPM film by using soft XAS and XRR at BL10/NewSUBARU. The differences of molecular orientation and surface structure due to manufacturing process and heating treatment are discussed in this report. Because the Ar-GCIB method hardly damaged films, this method is helpful in analyzing organic thin films with depth information.

## Introduction

Organic multilayer is the common structure for OEL devices. Though the thickness of each layer is the same in several devices, the performances are not always the same because the molecular orientation, surface roughness, density, and composition ratio of each layer are affected by the manufacturing processes. In this report, we will introduce some cases of the deterioration and the depth-profile analyses by using the soft X-ray absorption spectroscopy (soft XAS) at BL10/NewSUBARU for thin film of 4,6-bis(3,5-di-3-pyridylphenyl)-2-methylpyrimidine (B3PyMPM) which is commonly used for the electron transport layer of OEL devices.

## Experiments

The total electron yield (TEY) - XAS measurements were performed across carbon k-edge and nitrogen k-edge (C K and N K), and the X-ray incident angle was varied as  $\theta = 90^\circ$ ,  $70^\circ$ ,  $54.5^\circ$  and  $30^\circ$  in XAS measurements. For the X-ray reflectometry (XRR) measurement, the X-ray incident angle was varied  $5^\circ - 20^\circ$ .

### 1. Deterioration analysis of B3PyMPM film

B3PyMPM films were vacuum deposited or spin coated to 100 nm thickness onto silicon substrate. In order to examine the degradation process by XAS and XRR, those untreated films and a heat treatment films, heated for 1 hour at  $120^\circ\text{C}$ , were compared. The density of state (DOS) was calculated using the discrete variational (DV)-X $\alpha$  molecular orbital calculation and the electron state was analyzed. The XRR results were analyzed with the simulation soft offered by

the center for X-ray optics (CXRO).

### 2. Depth-profile analysis by the XAS measurement with the GCIB method

B3PyMPM thin films were vacuum deposited or spin coated to 100 nm thickness onto an Indium-Tin-Oxide (ITO) substrate. These films were etched by the Ar-GCIB (Gas Cluster Ion Beam) method. The etched areas were 2 mm in width and length, and 10 nm, 30 nm, and 50 nm in depth. To examine the molecular orientation, the incident angles ( $\theta$ ) of soft XAS were tuned to a normal ( $90^\circ$ ) and a magic angle ( $54.5^\circ$ ).

## Results and Discussion

### 1. Deterioration analysis of B3PyMPM film

The molecular orientation could be elucidated by change of the  $\pi^*$  peak to  $\sigma^*$  peak intensity ratio in the N K region of the X-ray absorption near edge structure (XANES) spectra. This result indicates that the vacuum deposited film shows the horizontal orientation of B3PyMPMs before heat treatment, but the orientation decreased after heat treatment. The spin coated film does not show the molecular orientation regardless of the heat treatment.

In the XRR spectra shown in Table I, the X-ray interference patterns, come from reflects at the interface between the film and the substrate, appear for the untreated films. However, that patterns does not appear for the heat treatment films.

In SEM images shown in Table I, the roughness of the film surface is getting large with crystallization progress by heating. This result indicates that the film preparation method have an

influence on a crystallization a surface of films.

Table I. Heat treatment effects for vacuum deposited films with XRR and SEM.

Sample	XRR (X-ray incident angle = $10^\circ$ )	Film surface by SEM
Deposited film (Before heating)		
Deposited film (After heating)		

## 2. Depth-profile analysis by the XAS measurement with the GCIB method

The vacuum deposited and spin coated films show the same N K - XANES spectra on the GCIB processed surface regardless of the processed depth shown in Figure 1. This result indicates that the Ar-GCIB method hardly damage films. In other words, the Ar-GCIB method is helpful in analyzing the angle variable XAS exactly at the processed area in BL10.

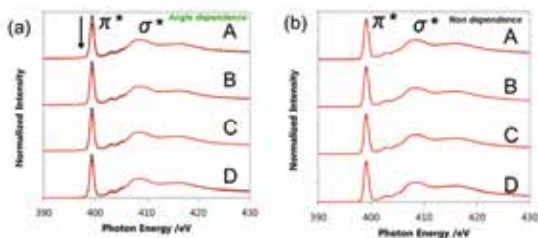


Figure 1. N – K XANES spectra for vacuum deposited films (a) and spin coated films (b) with untreated (A), GCIB treatment 10 nm (B), 30 nm (C), and 50 nm (D). The red curves mean the incident angle was  $90^\circ$ , and the black curves mean that was  $54.5^\circ$ .

## Reference

[1] F. Zheng, B. N. Park, S. Seo, P. G. Evans, F. J. Himpsel: *J. Chem. Phys.*, **126**, 154702 (2007).

# Analysis of adsorbed monolayer molecules formed by oil additives on frictional surfaces by NEXAFS

Naoko Takahashi<sup>1</sup>, Masaru Okuyama<sup>1</sup>, Noritake Isomura<sup>1</sup>, Mamoru Tohyama<sup>1</sup>  
 Yasuji Kimoto<sup>1</sup>, Toshihide Ohmori<sup>1</sup>,  
 Yasuji Muramatsu<sup>2</sup>, Keita Nanbu<sup>2</sup>, Takahito Ouchi<sup>2</sup>  
<sup>1</sup>Toyota Central R&D Labs., Inc., <sup>2</sup>University of Hyogo

## Abstract

To understand frictional mechanism of automatic transmission, it is important to detect adsorbed monolayer molecules on the frictional surfaces formed by ATF (automatic transmission fluid) additives. We measured C K-edge spectra of the frictional surfaces, which were slid with base oil and ATFs with two types of amine-based additives. The spectra with additives were successfully obtained and showed a unique feature, which was different from the spectrum of the base oil.

## Introduction

Since friction reduction of mechanistic parts in automobiles is important from the viewpoints of energy conservation and CO<sub>2</sub> exhaust reduction, analysis of the low friction surfaces is the key technology to understand and improve the performances. Particularly in the case of lubricated surfaces with ATF, adsorbates from the additives significantly influence on the friction properties and there analysis is necessary to elucidate the friction mechanism.

In general, there are adequate methods to obtain the chemical and physical information of adsorbed species of the additive, infrared spectroscopy (IR), Raman spectroscopy and electron probe micro analyzer (EPMA). However, their analysis depth is too deep and lacks sensitivity to detect the adsorbed molecules on the frictional surface shown in Fig. 1. On the other hand, X-ray photoelectron spectroscopy (XPS) and time of flight secondary ion mass spectrometry (TOF-SIMS) are able to detect the adsorbed molecules with high sensitivity because their analysis depth is only several nanometers and shallow enough to detect the surface layer information. However, it is still challenging for these methods to elucidate the detailed chemical structure for any kind of molecules. For example, XPS cannot discriminate between C-H and C-C bonds clearly,<sup>1-2)</sup> and TOF-SIMS will decompose such molecules by ion irradiation and show confusing mass numbers for assignments. Therefore, a development of alternative analytical method is significantly important for tribological studies.

In this experiment, we tried to detect monolayer-adsorbed molecules on the frictional surfaces to analyze the adsorption state of the ATF additives by near-edge X-ray absorption fine structure (NEXAFS), although

there are only few examples which have reported NEXAFS analysis for the additives.<sup>3-5)</sup> NEXAFS has enough structure dependent sensitivity to detect the adsorbed molecules on the frictional surface and enable us to analyze the detailed information of molecular structures and their electronic states.

Table 1 shows examples of additives for ATF or engine oil. As our first trial in this experiment, we analyzed amine-based additives on the frictional surfaces.

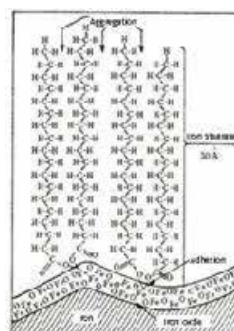


**Fig. 1** An estimated model of adsorbed stearate molecules on the frictional iron surface.<sup>6)</sup>

**Table 1** Representative additives of ATF and engine oil.

Amine based friction modifier	
Molybdenum based friction modifier	
Anti-wear agent and Antioxidant	
Metal-based cleaner	
Ashless dispersant	

## Experimental

Block specimens after friction tests were used for the analysis. The friction tests were carried out by a block-on-ring type apparatus with SUS440C block and AISI4620 ring (fig. 2). Two types of ATF's containing amine-based additives, oleylamine or polyoxyethylene oleylamine, were applied for the friction tests. The original base oil without any additive was also used as a control. Test parameters were as follows; load=289 N, sliding velocity=0.3 m/s, oil temperature=80°C and sliding time=30 minutes.

C K-edge NEXAFS spectra were measured in BL10 at New SUBARU by a total-electron-yield (TEY) method with sample current mode. The angle between the surface and the direction vector of incident X-ray was 90 degrees and the spectra were acquired by monitoring the sample drain current.

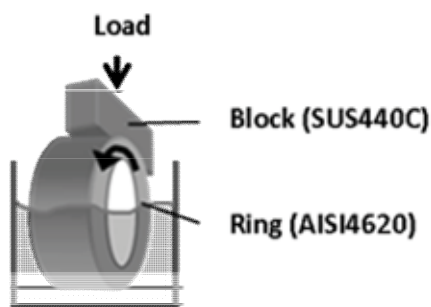


**Fig. 2** A schematic illustration of a block-on-ring type apparatus

## Result

In the case of amine-based ATF additives, actual friction on a surface is necessary to take effect because frictional interaction such as heat or pressure creates the adsorbed layer. The layer remains even after removal of the oil by washing process. We tried to detect C K-edge NEXAFS spectra to obtain the details of the layer because C K-edge information was important to understand the molecular structure, for example  $\pi$  and  $\sigma$  bondings, in general.

Figure 3 shows the C K-edge spectra of specimens after friction test. It is interesting to note that the specimen without additives exhibits clear C K-edge spectrum and we predict that there was an organic thin film formed by the base oil even without any additive. The two specimens with additive containing ATF's show identical spectra, which are different from the spectrum of the base oil. The results indicate that the adsorbed layers created by additives have similar structure even the original additives

had different molecular structure. Currently, the assignment of the spectra is under investigation by ab-initio DFT calculation to understand physical and chemical structure of the adsorbed layer. Such information is important to develop and improve the frictional performance of additives.

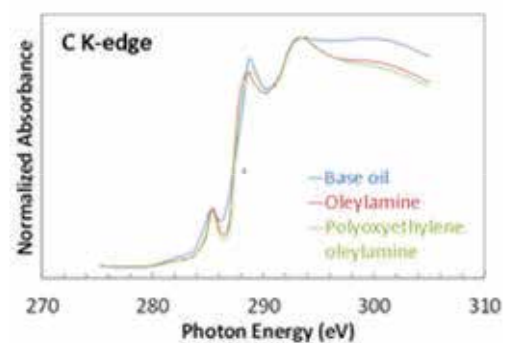


**Fig. 3** C K-edge NEXAFS spectra of the surface of block specimens slid in base oil and ATF's with two types of amine-based additives, oleylamine or polyoxyethylene oleylamine.

## References

- [1] D. Briggs and M. P. Seah, Practical Surface Analysis by Auger and X-ray Photoelectron Spectroscopy 2nd ed. John Wiley & Sons Ltd., New York, 598-635 (1990)
- [2] J. F. Moulder, W. F. Stickle, P. E. Sobol, K. D. Bomben, Hand Book of X-ray Photoelectron Spectroscopy (1995)
- [3] T. Uemura, Y. Muramatsu, K. Nanbu, T. Harada and H. Kinoshita, Advances in X-Ray Chemical Analysis, Japan, 45 (2014)
- [4] T. K. Sham, Chemical Applications of Synchrotron Radiation X-ray applications, World Scientific (2002)
- [5] J. C. Riviere and S. Myhra, Handbook of Surface and Interface Analysis Methods for Problem-Solving 2nd ed. CRC Press (2009)
- [6] T. Sakurai, Physical chemistry of lubrication 126 (1983)

# Miniature Micro-Powder Feeder Driven by Surface Acoustic Wave

Tsunemasa Saiki<sup>a,b</sup>, Akinobu Yamaguchi<sup>b</sup>, Michitaka Suzuki<sup>b</sup>, and Yuichi Utsumi<sup>b</sup>  
<sup>a</sup> Hyogo Prefectural Institute of Technology, <sup>b</sup> University of Hyogo

## Abstract

In this study, we investigated the relationship between powder transport efficiency and shape of an inter-digital transducer (IDT) that generates a surface acoustic wave (SAW). On the basis of the investigation, we fabricated a high-efficiency miniature feeder that possesses a powder storage hopper for practical use. As the result, it was shown that the feeder with an IDT with 2000- $\mu\text{m}$  pitch size has transportation capability of 15 mg/s at 1 W.

## Introduction

In the electronics and drug-discovery industries, physical operations, such as transportation and separation of micro powder, are required. However, it is difficult to efficiently handle such powder because it can behave not only as a solid but also as a liquid or gas. It has been impossible to transport a tiny amount, from several hundred  $\mu\text{g}$  to several mg, of dry powder if a general-purpose conveyor or blower that has been miniaturized is used. An ultrasonic wave device can be used to transport tiny amounts of powder [1]. However, since such devices consist of piezoelectric multi-layers, their manufacturing process is complicated. We therefore focused on a surface acoustic wave (SAW) device with a simple structure and have been studying the basic properties of SAW actuators for transporting powder [2]. In this study, we investigated the relationship between powder transport efficiency and shape of an inter-digital transducer (IDT) that generates a SAW and fabricated a high-efficiency miniature feeder that possesses a powder storage hopper for practical use. Incidentally, we presented this study at an international conference [3].

## IDT suitable for powder transport

From the results from our previous liquid flow experiment involving SAW actuators [4], the pitch size, an IDT shape parameter, greatly affected liquid flow characteristics. We thus investigated the relationship between pitch size and powder transport efficiency of SAW actuators. The experimental setup for investigating the relationship is shown in Fig. 1. A function generator created 1-kHz burst waveforms consisting of 2000 cycles of  $f_D$ -Hz sine waves, and a radio-frequency (RF) amplifier boosted the burst waveform voltage. The  $f_D$  was an experimental frequency value obtained from the return loss characteristic of an

IDT [3]. The IDTs were made of a 1- $\mu\text{m}$  Al layer and fabricated on a piezoelectric substrate (a 128-degree  $y$ -rotated  $x$ -propagating  $\text{LiNbO}_3$  wafer) by using photolithography, etching, and dicing processes. Incidentally, central axis directions of the IDTs were matched with an oriental flat direction of the wafer. Then, when the boosted voltage was applied to the IDT, a SAW was generated and propagated on the piezoelectric substrate. The SAW arrived at the copper powder (total weight: 30 mg and average particle diameter: approximately 100  $\mu\text{m}$ ), and the powder was transported downstream of the SAW. The powder transportation was recorded with a high-definition video camera, and electric power  $P_A$  instead of the burst wave voltage was measured using a power meter. From the recorded videos, we evaluated the powder transport speed  $S$ . The relationship between powder transport speed and electric power applied to the IDT is shown in Fig. 2. The powder transport speed increased almost linearly with the applied electric power. On the other hand, under the same electric power, the transport speed became faster as the pitch size  $p$  increased. The IDT with 2000- $\mu\text{m}$  pitch size had the highest powder transport efficiency in our prepared IDTs (pitch sizes of 200, 400, 800, and 2000  $\mu\text{m}$ ).

## Micro-powder feeder with high efficient IDT

Based on these results, we fabricated a miniature SAW feeder with an IDT with 2000- $\mu\text{m}$  pitch size. The powder transportation behavior on the fabricated SAW feeder is shown in Fig. 3. The IDT's aperture size and number of stripline pairs are 10 mm and 10, respectively. For practical use, the SAW feeder has a powder storage hopper of 0.4  $\text{cm}^3$ . The hopper has an inverted cone shape with an apex angle of 60 degrees and a height of 10 mm and has a hole diameter of 1 mm in its bottom. In the experiment, 500 mg of copper powder was put

in the hopper. The SAW feeder was then operated by applying 930 mW of electric power to the IDT with the same method shown in Fig. 1. The generated SAW transported the powder under the hopper. When there was not enough powder under the hopper, the amount of the powder to replenish was supplied from the hopper by gravity. On the other hand, the powder transporting on a substrate was gradually collected using two guide walls (height: 2 mm, length: 35 mm, and convergence angle: 20 degrees) until the powder arrived at an outlet (an interspace between the guide walls of 2 mm) of the SAW feeder and grains of the powder fell one after the other. The weight of the fallen powder  $m$  was measured using an electronic balance located under the outlet. Incidentally, the hopper and guide walls were made of hard transparent resin (Fullcure720) and fabricated using a 3D printer (Stratasys Inc. Connex500). A temporal change in the weight of the fallen powder (i.e., supplied) from the SAW feeder is shown in Fig. 4. The powder weight supplied from the SAW feeder driven at about 1 W increased gradually with elapsed time  $t$  and reached about 90% of the initial storage weight in the hopper after about 30 s. From the slope of the straight line determined using the least square method, the transportation capability of the SAW feeder was estimated to be about 15 mg/s. This indicates that, by slowing the transport speed, the fabricated SAW miniature feeder can supply powder with high accuracy of several mg or less.

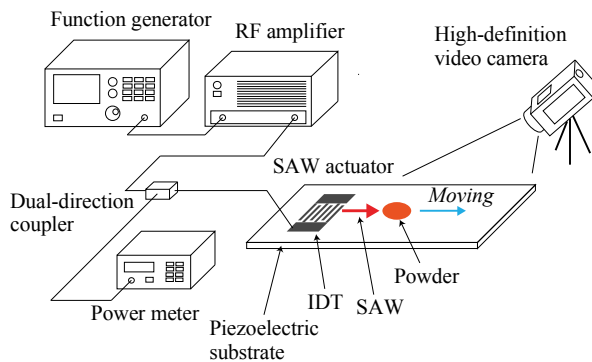


Fig. 1 Experimental setup for observing powder transport behavior by using SAW

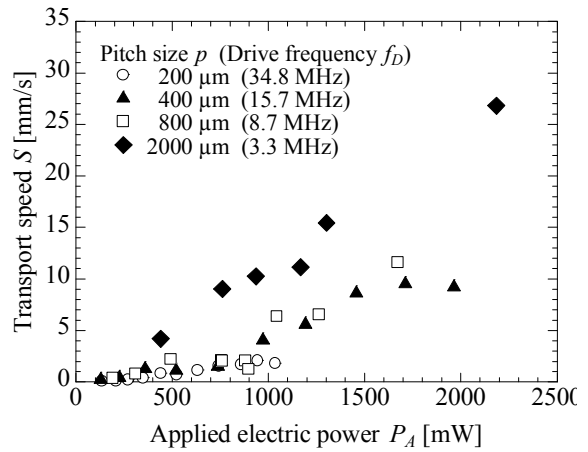


Fig. 2 Relationship between powder transport speed and electric power in each ITD's pitch size

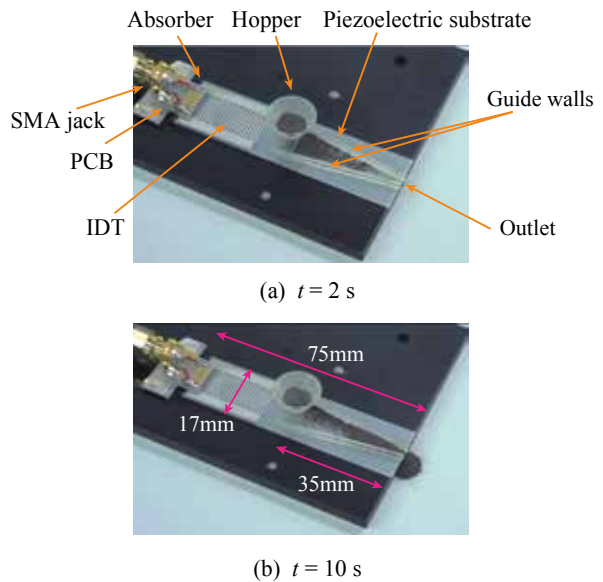


Fig. 3 Photographs of powder transportation behavior on fabricated SAW feeder

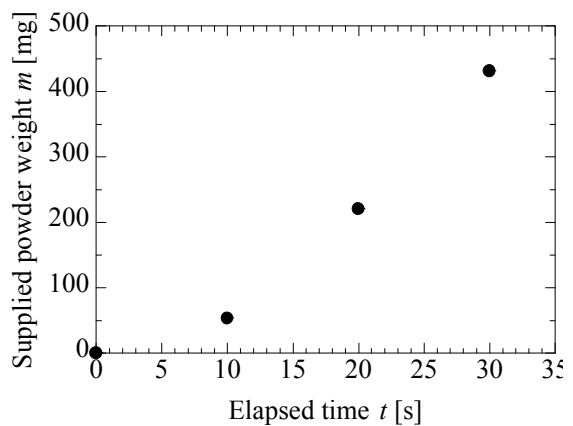


Fig. 4 Temporal change in powder weight supplied from SAW feeder

## References

- [1] M. Mracek, J. Wallaschek, A System for Powder Transport Based on Piezoelectrically Excited Ultrasonic Progressive Waves, *Mertericals Chemistry and Physics*, 90, 378-380 (2005).
- [2] T. Saiki, Y. Arisue, K. Kuramoto, H. Shizuka, M. Takeo, K. Maenaka, Y. Utsumi, Direction Control of Powder Transport on Solid Substrate by Drive Frequency of Surface Acoustic Wave Actuator, *Proc. of 38th International Conference on Micro and Nano Engineering (MNE2012)*, P270-022 (2012).
- [3] T. Saiki, A. Tsubosaka, A. Yamaguchi, M. Takeo, M. Suzuki and Y. Utsumi, Development of Miniature Micro-Powder Feeder Driven by Surface Acoustic Wave for Practical Use, *Proc. of 42nd International Conference on Micro and Nano Engineering (MNE2016)*, Wed-C2-159 (2016).
- [4] T. Saiki, K. Okada, and Y. Utsumi, Highly Efficient Liquid Flow Actuator Operated by Surface Acoustic Waver, *Electronics and Communications in Japan*, 94, 10, 10-16 (2011).

# C-, N-, O-XANES analyses of complex suites of organic compounds produced by laboratory simulations of extraterrestrial environments

Yoko Kebukawa<sup>1</sup>, Shusuke Misawa<sup>1</sup>, Hitomi Abe<sup>1</sup>, Shingo Enomoto<sup>1</sup>, Yasuji Muramatsu<sup>2</sup>, Takahito Ouchi<sup>2</sup>, Sohta Hamanaka<sup>2</sup>, Hitoshi Fukuda<sup>3</sup>, Yoshiyuki Oguri<sup>3</sup>, Satoshi Yoshida<sup>4</sup>, Isao Yoda<sup>3</sup>, and Kensei Kobayashi<sup>1</sup>

<sup>1</sup>Yokohama National University, <sup>2</sup>University of Hyogo, <sup>3</sup>Tokyo Institute of Technology, <sup>4</sup>National Institute for Quantum and Radiological Sciences and Technology

## Abstract

We conducted C, N, O *K*-edge X-ray absorption near edge structure (XANES) analyses for complex suites of organic compounds synthesized by simulating experiments for various extraterrestrial environments at BL10, NewSUBARU. Variations in functional group chemistry were observed depending on the starting materials and experimental conditions.

## Introduction

Primitive meteorites, such as carbonaceous chondrites contain a few wt.% organic matter. The most of organic carbon (>70 wt.%C) exists as in the form of solvent insoluble organic matter (IOM) with complex macromolecular structures. Rest of the organic carbon is in the form of solvent extractable organic compounds that include tens of thousands of different molecular compositions, with possibly millions of diverse structures [1]. Some of them, such as amino acids and nucleobases could have been contributed to the emergence of life in the early earth. The origins and formation processes of these diverse extraterrestrial organic matter were not well known.

In the very low temperature (~10-50 K) molecular cloud, chemical reactions would be driven by cosmic rays and UV and occurred in the ice mantles on the silicate dust grains. Laboratory experiments showed that various organic molecules including amino acids were produced by particle irradiations or UV to ices that consist of simple molecules such as H<sub>2</sub>O, CO and CH<sub>3</sub>OH [e.g. 2]. The Solar System formed from such molecular cloud by gravitational collapse. Small bodies (“planetesimals”) accreted from dust. Planetesimals formed far enough from the Sun contains icy dust. Internal heating of the planetesimals containing icy dust turned ice into aqueous solution. Chemical reactions involving liquid water could produce organic matter [e.g. 3].

Simulated experiments for various extraterrestrial environments produces complex suites of organic compounds. Amino acids are produced by acid hydrolysis of these organic

compounds. We have been investigated these complex organic compounds with C, N, O *K*-edge X-ray absorption near edge structure (XANES) spectroscopy. In order to understand the nature and chemistry of the extraterrestrial organic matter including amino acid precursors.

## Simulated interstellar media

Gas mixtures of CO, NH<sub>3</sub> and H<sub>2</sub>O with and without CH<sub>4</sub> were irradiated with 2 mC of 2.5 MeV protons from a Tandem accelerator at Tokyo Institute of Technology. The products are hereafter abbreviated to as CAW (without CH<sub>4</sub>) and CMAW (with CH<sub>4</sub>). Gas mixtures of CH<sub>3</sub>OH, NH<sub>3</sub>, H<sub>2</sub>O were irradiated with 290 MeV/u C<sup>+</sup> ion at room temperature and 77 K from Heavy Ion Medical Accelerator in Chiba (HIMAC) at National Institute of Radiological Sciences (NIRS). The products are hereafter abbreviated to as MeAW. The experimental products were collected with pure water, if necessary. A few drops of each product was dried on a Al plate for C,N,O-XANES analyses at BL10, NewSUBARU (NS).

C-XANES of CAW showed peaks at 284.0 eV (C1), 285.5 eV (C3), 288.6 eV (C5) and 290.0 eV (C6), while CMAW showed similar features but less 290.0 eV peak (Fig. 1) [4]. Possible assignments of these peaks are aromatic/olefinic C=C for 285.5 eV (C3), carbonyl/carboxyl O-C=O for 288.6 eV (C5), and carbamoyl N-C=O for 290.0 eV [5]. Less carbamoyl in CMAW might indicate that majority of C=O in CMAW is adjacent to methyl/ethyl carbon rather than amines.

C-XANES of MeAW irradiated at room temperature (r.t.) and 77K showed peaks at 283.7 eV (C1), 288.6 eV (C4), 290.0 eV (C5) (Fig. 2) [4]. In addition, MeAW(r.t.) showed

285.2 eV and MeAW(77K) showed 287.2 eV (C3) which is assigned to aliphatic carbon. These results indicated that lower temperature samples tend to have more aliphatic structures and higher temperature samples tend to have more aromatic structures.

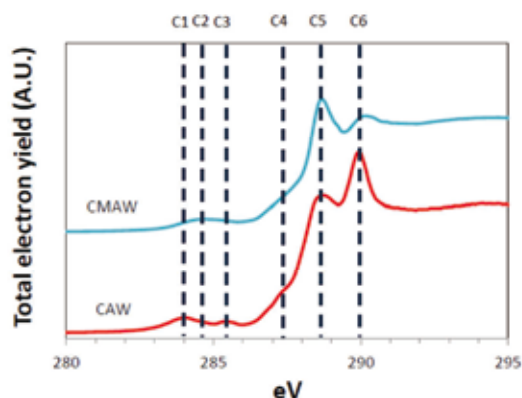


**Fig. 1** C-XANES spectra of CAW (CO, NH<sub>3</sub>, H<sub>2</sub>O) and CMAW (CO, CH<sub>4</sub>, NH<sub>3</sub>, H<sub>2</sub>O) irradiated by proton [4].

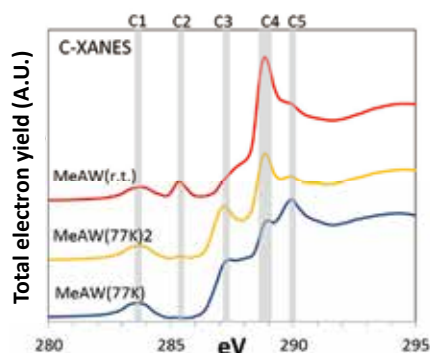


**Fig. 2** C-XANES spectra of MeAW (CH<sub>3</sub>OH, NH<sub>3</sub>, H<sub>2</sub>O) irradiated by C<sup>+</sup> ion at room temperature (r.t.) and 77K [4].

### Simulated Titan atmosphere

Titan is the largest moon of Saturn, which has a dense atmosphere mostly consisted of nitrogen and methane. An active organic chemistry is considered to take place in the atmosphere due to irradiation by solar UV light, Saturnian magnetospheric electrons and cosmic rays as energy sources. Complex organic materials produced in laboratory simulations have often been called “tholins”, which contain hydrocarbon, nitrile and heterocyclic aromatic moieties. Most laboratory works have simulated reactions in the higher atmosphere of Titan caused by solar UV and Saturnian magnetospheric electrons. In the lower atmosphere, cosmic rays could have larger contribution, Taniuchi et al. [6] studied that tholins formed by proton irradiations produced a wide variety of amino acid after acid hydrolysis.

A 700 Torr (93 kPa) of gas mixture of

nitrogen (95%) and methane (5%) was prepared as a simulated Titan tropospheric atmosphere. The pressure corresponds to that of Titan at an altitude of 10 km. The gas mixtures were irradiated with 1 to 5 mC protons from a Tandem accelerator at Tokyo Institute of Technology. After proton irradiation, the products inside Pyrex tube were collected with several kinds of solvents that have different polar character, and were analyzed by C,N,O-XANES using BL10/NS.

C,N-XANES analyses showed that the tholins contained amine groups, cyanide functional groups and aliphatic moieties (Fig. 3) [7]. Molecular structures of tholins shows some variations depend on the solvents used for extraction, indicating that tholins contains various compounds with different polarity.

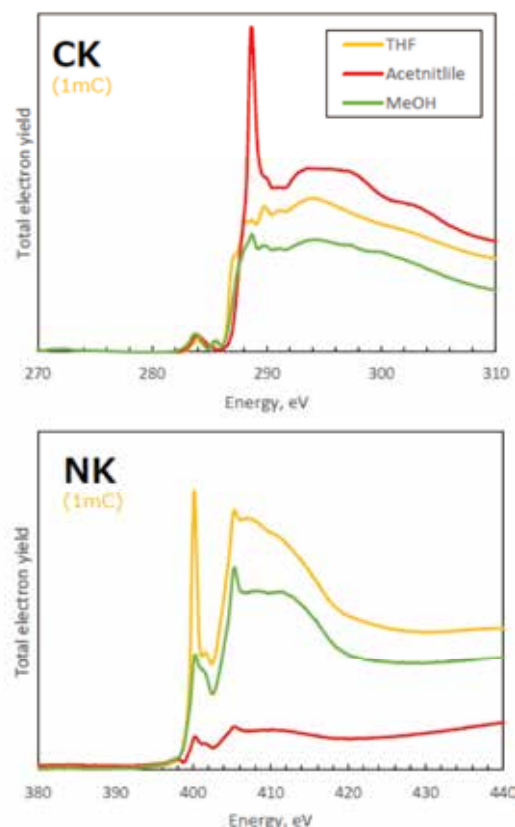


**Fig. 3** C-XANES and N-XANES spectra of Titan tholins irradiated by 1 mC proton, extracted by tetrahydrofuran (THF), acetonitrile, and methanol (MeOH) [7].

### Simulated aqueous alteration in planetesimals

Carbonaceous chondrites that are samples from aqueously altered parent bodies, contain various organic matter, which mostly consists of insoluble organic matter (IOM), and also contain some soluble organic compounds including amino acids. Cody et al. [3] proposed IOM formation via formose reaction starting

with formaldehyde during aqueous activity in the solar system small bodies. Additional hydrothermal experiments showed that ammonia enhanced the yields of IOM like organic matter and simultaneously produced amino acid precursors [8]. The most effective heat source for melting water ice in small bodies is considered to be the decay of  $^{26}\text{Al}$ . However the effects of radiation from  $^{26}\text{Al}$ , e.g. gamma-ray, has not been reported yet. Thus the effects of gamma-ray as an energy source for the formation of organic matter were evaluated.

The starting solutions contained formaldehyde, ammonia, water, with/without  $\text{Ca}(\text{OH})_2$  as a catalyst. Each solution was flame sealed into glass tubes. Gamma-ray irradiation experiments were conducted using  $^{60}\text{Co}$  source at Tokyo Institute of Technology. Heating experiments were conducted at  $150\text{ }^\circ\text{C}$  for 24 hours for comparison.

C-XANES spectra of the gamma-ray irradiation samples and heated samples showed some differences (Fig. 4). The gamma-ray irradiation samples have dominated 285.0 eV (aromatic) and 290.0 eV (carbamoyl) peaks compared to heated samples.

The results show that organic compounds formed by the gamma-ray irradiation to the formaldehyde and ammonia water solutions were different from those formed by heating, thus the reaction mechanisms would be different between gamma-ray irradiation and heating.

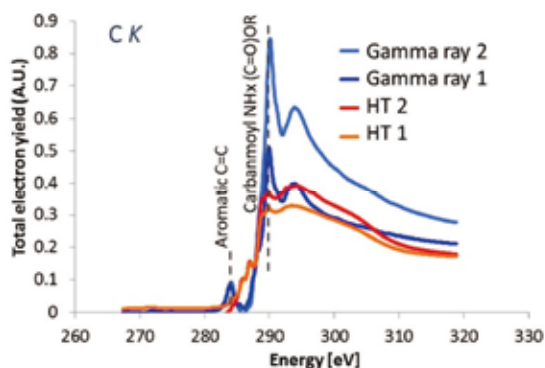


**Fig. 4** C-XANES of the products from formaldehyde and ammonia water solutions by gamma-ray irradiation and hydrothermal (HT) treatments.

## Conclusions

We successfully obtained functional group analysis of laboratory synthesized organic matter simulating various extraterrestrial environments using C,N,O-XANES at BL10/NS. However, peak assignments of C,N,O-XANES remain ambiguity. We further need analyses of standard compounds for solid peak assignments.

## References

- [1] P. Schmitt-Kopplin, Z. Gabelica, R. D. Gougeon, A. Fekete, B. Kanawati, M. Harir, I. Gebefuegi, G. Eckel, N. Hertkorn: PNAS, 107, 2763 (2010).
- [2] J. M. Greenberg, A. Li, C. X. Mendozagomez, W. A. Schutte, P. A. Gerakines, M. Degroot: Astrophysical Journal, 455, L177 (1995).
- [3] G. D. Cody, E. Heying, C. M. O. Alexander, L. R. Nittler, A. L. D. Kilcoyne, S. A. Sandford, R. M. Stroud: PNAS, 108, 19171 (2011).
- [4] S. Enomoto: Master thesis, Yokohama National University (2017).
- [5] G. D. Cody, H. Ade, C. M. O. Alexander, T. Araki, A. Butterworth, H. Fleckenstein, G. Flynn, M. K. Gilles, C. Jacobsen, A. L. D. Kilcoyne, K. Messenger, S. A. Sandford, T. Tyliszczak, A. J. Westphal, S. Wirick, H. Yabuta: Meteoritics & Planetary Science, 43, 353 (2008)
- [6] T. Taniuchi, Y. Takano, K. Kobayashi: Analytical Sciences, 29, 777-785 (2013).
- [7] H. Abe: Master thesis, Yokohama National University (2017).
- [8] Y. Kebukawa, Q. H. S. Chan, S. Tachibana, K. Kobayashi, M. E. Zolensky: Science Advances, 3, e1602093 (2017)



### Part 3. List of Publications



H. Hashimoto in a master's course of a graduate school won the Best Academic Poster Award in Photomask Japan 2016.



## List of publications

### (1) Papers

1. **"Positron annihilation Doppler broadening measurement for bulk amorphous alloy by using high energy positron generated from LCS gamma-ray at NewSUBARU"**  
F. Hori, Y. Ueno, K. Ishii, T. Ishiyama, A. Iwase, S. Miyamoto, M. Terasawa  
Journal of Physics: Conference Series **674** (2016) 012025.
2. **"Development of Compton X-ray spectrometer for high energy resolution single-shot high-flux hard X-ray spectroscopy"**  
Sadaoki Kojima, Takahito Ikenouchi, Yasunobu Arikawa, Shohei Sakata, Zhe Zhang, Yuki Abe, Mitsuo Nakai, Hiroaki Nishimura, Hirouyuki Shiraga, Tetsuo Ozaki, Shuji Miyamoto, Masashi Yamaguchi, Akinori Takemoto, Shinsuke Fujioka, and Hiroshi Azechi  
Review of Scientific Instruments, **87**, 043502 (2016).
3. **"Spatial anisotropy of neutrons emitted from the  $^{56}\text{Fe}(\gamma, n)^{55}\text{Fe}$  reaction with a linearly polarized  $\gamma$ -ray beam"**  
T. Hayakawa, T. Shizuma, S. Miyamoto, S. Amano, A. Takemoto, M. Yamaguchi, K. Horikawa, H. Akimune, S. Chiba, K. Ogata and M. Fujiwar  
Physical Review C, **93**, pp. 004313-1-4 (2016).
4. **"Proposal for selective isotope transmutation of long-lived fission products using quasi-monochromatic  $\gamma$ -ray beams"**  
Takehito Hayakawa, Shuji Miyamoto, Ryoichi Hajima, Toshiyuki Shizuma, Sho Amano, Satoshi Hashimoto, Tsuyoshi Misawa  
Journal of Nuclear Science and Technology, **53**, issue 12, pp.2064-2071 (2016).
5. **"Harmonics radiation of graphene surface plasmon polaritons in terahertz regime"**  
D. Li, Y. Wang, M. Nakajima, M. Hashida, Y. Wei, S. Miyamoto  
Physics Letters A **380**, pp.2181–2184 (2016).
6. **"Laser Compton Scattering Gamma-Ray Experiments for Supernova Neutrino Process"**  
Takehito Hayakawa, Shuji Miyamoto, Takayasu Mochizuki, Ken Horikawa, Sho Amano, Dazhi Li, Kazuo Imasaki, Yasukazu Izawa, Kazuyuki Ogata and Satoshi Chiba  
Plasma and Fusion Research, **11**, 3406066 (2016).
7. **"Production of Medical  $^{99\text{m}}\text{Tc}$  Isotope Via Photonuclear Reaction"**  
M. Fujiwara, \*, K. Nakai, N. Takahashi, T. Hayakawa, T. Shizuma, S. Miyamoto, G. T. Fan, A. Takemoto, M. Yamaguchi, and M. Nishimura  
Physics of Particles and Nuclei, 2017, Vol. **48**, No. 1, pp. 124–133. © Pleiades Publishing, Ltd., (2017).  
ISSN 1063-7796
8. **"Investigation of pitting corrosion of diamond-like carbon films using synchrotron-based spectromicroscopy"**  
Sarayut Tunmee, Pat Photongkam, Chanan Euaruksakul, Hiroki Takamatsu, XiaoLong Zhou, Pornwasa Wongpanya, Keiji Komatsu, Kazuhiro Kanda, Haruhiko Ito, and Hidetoshi Saitoh  
Journal of Applied Physics **120**, 195303 (2016).
9. **"Double crystal monochromator controlled by integrated computing on BL07A in NewSUBARU, Japan"**  
Masato Okui, Naoki Yato, Akinobu Watanabe, Baiming Lin, Norio Murayama, Sei Fukushima, Kazuhiro Kanda  
AIP Conference Proceedings **1741**, 030033(2016).
10. **"Fabrication of hydrogenated amorphous silicon carbide films by decomposition of hexamethyldisilane with microwave discharge flow of Ar"**

Haruhiko Ito, Motoki Kumakura, Tsuneo Suzuki, Masahito Niibe, Kazuhiro Kanda, Hidetoshi Saitoh  
Japanese Journal of Applied Physics **55**, 06HC01 (2016).

11. **"Structure and physical properties of stable isotopic amorphous carbon films"**  
Yutaro Suzuki, Yasuyoshi Kurokawa, Tsuneo Suzuki, Kazuhiro Kanda, Masahito Niibe, Masayuki Nakano,  
Naoto Ohtake, Hiroki Akasaka  
Diamond and Related Materials, **63**, 115-119 (2016).
12. **"Low-Temperature Activation in Boron Ion-Implanted Silicon by Soft X-Ray Irradiation"**  
Akira Heya, Naoto Matsuo, Kazuhiro Kanda  
IEICE TRANS. ELECTRON., **E99-C**, (2016).
13. **"結晶配向性と励起エネルギーを変化させたグラファイトにおける C-K 発光スペクトルの入/出射  
角度依存性"**  
竹平徳崇, 新部正人, 荒木佑馬, 徳島高  
X線分析の進歩, **48**, 129-136 (2017).
14. **"Large take-off angle dependence of C-K emission spectra observed in highly oriented pyrolytic graphite"**  
Masahito Niibe, Takashi Tokushima, Noritaka Takehira, and Yuma Araki  
J. Electron Spectrosc. Relat. Phonom., DOI: 10.1016/j.elspec.2017.02.001, (2017).
15. **"AlGaN surfaces etched by CF<sub>4</sub> plasma with and without the assistance of near-ultraviolet irradiation"**  
Retsuo Kawakami, Masahito Niibe, Yoshitaka Nakano, Takashi Mukai  
Vacuum, **136**, 28-35 (2017).
16. **"Low energy soft X-ray emission spectrometer at BL-09A in NewSUBARU"**  
Masahito Niibe  
SPRING-8/SACLA Research Frontiers 2015, 149-150 (2016).
17. **"Low Energy Soft X-ray Emission Spectrometer at BL-09A in NewSUBARU"**  
Masahito Niibe and Takashi Tokushima  
Proc. SRI2015, AIP Conf. Proc., **1741**, 030042 (2016).
18. **"Development of the Surface-sensitive Soft X-ray Absorption Fine Structure Measurement Technique  
for Bulk Insulator"**  
Takumi Yonehara, Junji Iihara, Shigeki Uemura, Koji Yamaguchi, and Masahito Niibe  
Proc. SRI2015, AIP Conf. Proc., **1741**, 050025 (2016).
19. **"Fabrication and characterization of fine-grained 316L steel with 2.0 mass% Ti"**  
M. Terasawa, H. Kurishita, T. Sakamoto, M. Niibe, H. Takahashi, S. Nishikawa, A. Yamamoto, M. Yamashita, T.  
Mitamura, T. Yamasaki, M. Kawai  
J. Nuclear Sci. Technol., **53**, 1951-1959 (2016), DOI:10.1080/00223131.2016.1175390
20. **"Damage Characteristics of n-GaN Crystal Etched with N<sub>2</sub> Plasma by Soft X-ray Absorption  
Spectroscopy"**  
Masahito Niibe, Takuya Kotaka, Retsuo Kawakami, Yoshitaka Nakano, Takashi Mukai  
e-J. Surf. Sci. Nanotech, **14**, 9-13 (2016).
21. **"Surface Analysis of AlGaN Treated with CF<sub>4</sub> and Ar Plasma Etching"**  
Shodai Hirai, Masahito Niibe, Retsuo Kawakami, Tatsuo Shirahama, Yoshitaka Nakano, Takashi Mukai  
e-J. Surf. Sci. Nanotech, **13**, 481-487 (2015).
22. **"High-average-power water window soft X-rays from an Ar laser plasma"**  
S.Amano

Appl. Phys. Express, Vol.9, 076201 (2016)

23. **"Micromachining using soft X-rays from laser-produced Xe plasma"**  
S.Amano, T.Inoue, and S.Miyamoto  
Electro. Commum. in Japan, Vol.99, Issue 2, 3-9 (2016)
24. **"Depth analysis of molecular orientation induced by nanoimprint graphoepitaxy"**  
Makoto Okada, Ryosuke Fujii, Yuichi Haruyama, Hiroshi Ono, Nobuhiro Kawatsuki, and Shinji Matsui  
Japanese Journal of Applied Physics, Vol. 56, 040302 1-4 (2017).
25. **"Influence of film thickness on the reorientation structure of photoalignable liquid crystalline polymer films"**  
Y. Taniguchi, M. Kondo, Y. Haruyama, S. Matsui, and N. Kawatsuki  
Polymer 90, pp. 290-294 (2016).
26. **"Light stability tests of CH<sub>3</sub>NH<sub>3</sub>PbI<sub>3</sub> perovskite solar cells using porous carbon counter electrodes"**  
Seigo Ito, Gai Mizuta, Shusaku Kanaya, Hiroyuki Kanda, Tomoya Nishina, Seiji Nakashima, Hironori Fujisawa, Masaru Shimizu, Yuichi Haruyama and Hitoshi Nishino  
Phys.Chem.Chem.Phys. 18, 27102-27108 (2016).
27. **"ニュースバル放射光施設を活用したフォトマスク検査顕微鏡の開発"**  
原田哲男  
姫路工業倶楽部部報工学レポート vol. 28, 2017/1/1.
28. **"A Study on Enhancing EUV Resist Sensitivity"**  
A. Sekiguchi, T. Harada, and T. Watanabe  
Proc. SPIE 10143 (2017) 1014322.
29. **"EUVレジスト開発と歴史"**  
渡邊健夫  
リソグラフィ技術その40年、S&T出版、2016.12.9.
30. **"Current Status and Prospect of EUVL Lithography for IoT"**  
Takeo Watanabe  
Proceedings of the 20th SANKEN International Symposium (2016) 10.
31. **"Development of EUV Lithographic Technology at University of Hyogo"**  
Takeo Watanabe, and Tetsuo Harada  
Proceedings of the 14th International Conference on radiation Curing, RadTech Asia (2016) 43.
32. **"Development of Actual EUV Mask Observation Method for Micro Coherent EUV Scatterometry Microscope"**  
T. Harada, H. Hashimoto, and T. Watanabe  
Proc. SPIE 9985 (2016) 99851T.
33. **"Observation Results of Actual Phase Defects Using Micro Coherent EUV Scatterometry Microscope"**  
H. Hashimoto, T. Harada, and T. Watanabe  
Proc. SPIE 9985 (2016) 99850K.
34. **"Development of the Transmittance Measurement for EUV Resist by Direct-Resist Coating on a Photodiode"**  
Daiki Mamezaki, Masanori Watanabe, Tetsuo Harada, and Takeo Watanabe,  
J. Photopolym. Sci. Technol., 29 (2016) pp. 749 - 752.
35. **"EUVL Research Activity at Center for EUV Lithography"**  
Takeo Watanabe, and Tetsuo Harada  
J. Photopolym. Sci. Technol., 29 (2016) pp. 737 - 744.

36. **"Extreme-ultraviolet collector mirror measurement using large reflectometer at NewSUBARU synchrotron facility"**  
Haruki Iguchi, Hiraku Hashimoto, Masaki Kuki, Tetsuo Harada, Hiroo Kinoshita, Takeo Watanabe, Yuriy Y. Platonov, Michael D. Kriese, and Jim R. Rodriguez  
Jpn. J. Appl. Phys. **55**, 06GC01 (2016)
37. **"EUV resist outgassing analysis for the new platform resists at EIDEC"**  
Eishi Shiobara, Yukiko Kikuchi, Shinji Mikami, Takeshi Sasami, Takashi Kamizono, Shinya Minegishi, Takakazu Kimoto, Toru Fujimori, Takeo Watanabe, Tetsuo Harada, Hiroo Kinoshita, Satoshi Tanaka  
Proc. SPIE **9776**, 97762H (2016).
38. **"Phase Imaging Results of Phase Defect Using Micro Coherent EUV Scatterometry Microscope"**  
Tetsuo Harada, Hiraku Hashimoto, Tsuyoshi Amano, Hiroo Kinoshita, and Takeo Watanabe  
J. Micro-Nanolith. Mem. **15**, 021007 (2016).
39. **"Actual defect observation results of an extreme ultraviolet blank mask by coherent diffraction imaging"**  
Tetsuo Harada, Hiraku Hashimoto, Tsuyoshi Amano, Hiroo Kinoshita, and Takeo Watanabe  
Appl. Phys. Express **9**, 035202 (2016).
40. **"On-chip synthesis of ruthenium complex by microwave-induced reaction in a microchannel coupled with post-wall waveguide"**  
Yuichi Utsumi, Akinobu Yamaguchi, Takeko Matsumura-Inoue, Mitsuyoshi Kishihara  
Sensors and Actuators B: Chemical, **242**, 384-388 (2017)
41. **"Highly sensitive detection and stochastic analysis of magnetization fluctuation induced in a nano-scale magnetic wire"**  
A. Yamaguchi, K. Motoi and H. Miyajima,  
Journal of Magnetism and Magnetic Materials, **401**, 9-15 (2016)
42. **"Real-space observation of magnetic vortex core gyration in a magnetic disc both with and without a pair tag"**  
Akinobu Yamaguchi, Hiroshi Hata, Minoru Goto, Motoi Kodama, Yuichi Kasatani, Koji Sekiguchi, Yukio Nozaki, Takuo Ohkochi, Masato Kotsugi, and Toyohiko Kinoshita  
Japanese Journal of Applied Physics, **55**, 023002 (2016)
43. **"Anisotropic pyrochemical microetching of poly(tetrafluoroethylene) initiated by synchrotron radiation-induced scission of molecule bonds"**  
Akinobu Yamaguchi, Hideki Kido, Yoshiaki Ukita, Mitsuyoshi Kishihara, and Yuichi Utsumi  
Applied Physics Letters, **108**, 051610 (2016)
44. **"Dielectrophoresis-enabled surface enhanced Raman scattering on gold-decorated polystyrene microparticle in micro-optofluidic devices for high-sensitive detection"**  
Akinobu Yamaguchi, Takao Fukuoka, Ryo Takahashi, Ryohei Hara, Yuichi Utsumi  
Sensors and Actuators B **230**, 94-100 (2016)
45. **"Synthesis of metallic nanoparticles through X-ray radiolysis using synchrotron radiation"**  
Akinobu Yamaguchi, Ikuo Okada, Takao Fukuoka, Ikuya Sakurai, and Yuichi Utsumi  
Japanese Journal of Applied Physics **55**, 055502-1-5 (2016)
46. **"Direct digital manufacturing of a mini-centrifuge-driven centrifugal microfluidic device and demonstration of a smartphone-based colorimetric enzyme-linked immunosorbent assay"**  
Yoshiaki Ukita, Yuichi Utsumi, Yuzuru Takamura  
Analytical Methods, **8**, 256-262 (2016)
47. **"Trial Fabrication of PTFE-Filled Waveguide Bandpass Filter at Short Millimeter Wave Frequency by SR Etching (放射光エッチングによる短ミリ波帯テフロン導波管バンドパスフィルタの試作)"**  
M. Kishihara, M. Murakami, A. Yamaguchi, Y. Utsumi and I. Ohta  
電子情報通信学会和文論文誌 C, **J99-C No.7**, 361-364 (2016)

48. **"Dielectrophoresis-enabled surface enhanced Raman scattering of glycine modified on Au-nanoparticle-decorated polystyrene beads in micro-optofluidic devices"**  
Akinobu Yamaguchi, Takao Fukuoka, Kazuhisa Kuroda, Ryohei Hara, Yuichi Utsumi  
Colloids and Surfaces A: Physicochemical and Engineering Aspects, **507**, 118-123 (2016)
49. **"Rapid X-ray Fabrication of Microstructured Polytetrafluoroethylene Substrates by Anisotropic, Pyrochemical Microetching"**  
Akinobu Yamaguchi, Hideki Kido, Yuichi Utsumi  
Journal of Photopolymer Science and Technology, **29**, 3, 403-407 (2016)
50. **"One-Step Synthesis of Copper and Cupric Oxide Particles from the Liquid Phase by X-Ray Radiolysis Using Synchrotron Radiation"**  
Akinobu Yamaguchi, Ikuo Okada, Takao Fukuoka, Mari Ishihara, Ikuya Sakurai, Yuichi Utsumi  
Journal of Nanomaterials, 2016, Article ID 8584304 (2016)
51. **"Interdigital transducer generated surface acoustic waves suitable for powder transport"**  
Tsunemasa Saiki, Akio Tsubosaka, Akinobu Yamaguchi, Michitaka Suzuki, Yuichi Utsumi  
Advanced Powder Technology, **28**, 491-498 (2017)
52. **"Synthesis of Cupric Particles Induced by X-ray Radiolysis"**  
Akinobu Yamaguchi, Ikuo Okada, Takao Fukuoka, Yuichi Utsumi  
IEEJ Transactions on Electronics, Information and Systems, **137**, 3, 400-405 (2016)
53. **"Alternative Raman Spectroscopy of Glycine binding on Au-Nanoparticle-Decorated Polystyrene Beads due to Aggregation induced by Dielectrophoresis in Micro-Optofluidic Devices"**  
A. Yamaguchi, T. Fukuoka and Y. Utsumi  
Micro TAS 2016, M168h
54. **"Anisotropic Pyrochemical Fabrication of Polytetrafluoroethylene and Metallic Nanoparticles Initiated by Synchrotron Radiation for Microfluidic Devices"**  
A. Yamaguchi, H. Kido, Y. Ukita, M. Kishihara, T. Fukuoka and Y. Utsumi  
Micro TAS 2016, W132g
55. **"Fabrication of higher order three-dimensional layer stack nanostructure for molecular detection and electrode"**  
A. Yamaguchi, T. Fukuoka, M. Ishihara and Y. Utsumi  
Proc. SPIE **9929**, 992906 (2016)
56. **"Synthesis of nanoparticles through X-ray radiolysis using synchrotron radiation"**  
A. Yamaguchi, I. Okada, T. Fukuoka, M. Ishihara, I. Sakurai and Y. Utsumi  
Proc. SPIE **9929**, 992919 (2016)
57. **"X線光化学反応による金属ナノ・マイクロ粒子生成 (Fabrication of Metallic Nano/Microscale particles by Photochemical reaction initiated by X-ray Radiolysis in copper (II) sulfate solution)"**  
山口明啓, 岡田育夫, 福岡隆夫, 内海裕一  
MES 2016, 2D2-4
58. **"強誘電体/磁性体接合における磁気異方性の制御と磁区構造"**  
山口明啓, 才木常正, 内海裕一, 大河内拓雄, 保井晃, 木下豊彦, 山田啓介  
【A】基礎・材料・共通部門 マグネティクス研究会, 2016-9-20, MAG-16-134, 4 pages, IEEJ-MAG
59. **"圧電体基板上に創製した微小磁性体の磁気特性"**  
山口明啓, 才木常正, 内海裕一, 大河内拓雄, 保井晃, 木下豊彦, 山田啓介  
【A】基礎・材料・共通部門 マグネティクス研究会, 2016-12-8, MAG-16-228, 4 pages, IEEJ-MAG
60. **"Heat Transfer Performance of Sodium Encapsulating Engine Valves"**  
T. Kobayashi, I. Hashimoto, R. Hashimoto, H. Kanematsu, Y. Utsumi and M. Yamamoto  
Advanced Experimental Mechanics, **1**, 69-7 (2016)

61. **"Deformation Analysis of Soft Actuator having a Bellows Structure Operated by Inner Pressure"**  
T. Kobayashi, M. Fujiwara, Y. Utsumi, H. Kanematsu, M. Yamamoto and H. Taniguchi  
Advanced Experimental Mechanics, **1**, 185-189 (2016)
62. **"Measurement of Critical Cracking Strain of Organic Thin Films Prepared by Wet Coating Process"**  
T. Kobayashi, M. Munkhtsog, Y. Utsumi, H. Kanematsu, and T. Masuda  
Proc. 14th European Vacuum Conference (EVC-14), Portorose, Slovenia, 2016
63. **"Small immunoassay systems for medical diagnosis and environmental analysis"**  
T. Kobayashi, Y. Yoshimasa, Y. Utsumi  
Proc. The Irigo Conference 2016

(2) **International meetings**

1. **"Terahertz Radiation From Graphene Surface Plasmon Polaritons"**  
Dazhi Li, Yuanyuan Wang, Makoto Nakajima, Masaki Hashida, Yanyu Wei, Shuji Miyamoto, Masahiko Tani  
41st International Conference on Infrared, Millimeter, and Terahertz waves (IRMMW-THz), 25-30 Sept., Copenhagen, Denmark (2016).
2. **"Laser Compton Scattering Gamma-Ray Beam Source for Nuclear Physics and Material Research"**  
Shuji Miyamoto (Invited)  
15th International Conference on X-Ray Lasers (ICXRL2016), Nara Kasugano International Forum, May 22 - 27 (2016).
3. **"Photon scattering measurement on Cr-52 with Linearly Polarized Photon Beam at NewSUBARU"**  
T. Shizuma, T. Hayakawa, F. Minato, I. Daito, H. Ohgaki, S. Miyamoto  
International Nuclear Physics Conference, Adelaide, Australis, 11-16 Sept., (2016).
4. **"Measurement of neutron energy spectra for  $E_\gamma=23.1$  and 26.6 MeV mono-energetic photon induced reaction on natC using laser electron photon beam at NewSUBARU"**  
Toshiro Itoga, Hiroshi Nakashima, Toshiya Sanami, Yoshihito Namito, Yoichi Kirihara, Shuji Miyamoto, Akinori Takemoto, Masashi Yamaguchi and Yoshihiro Asano  
13th International Conference on Radiation Shielding, Paris, France, Oct. 3-6 (2016).
5. **"Measurement of neutron spectra for photonuclear reaction with linearly polarized photons"**  
Yoichi Kirihara, Toshiro Itoga, Hiroshi Nakashima, Toshiya Sanami, Yoshihito Namito, Shuji Miyamoto, Akinori Takemoto, Masashi Yamaguchi and Yoshihiro Asano  
13th International Conference on Radiation Shielding, Paris, France, Oct. 3-6 (2016).
6. **"Electronics for HARPO: Design, Development and Validation of Electronics for a High Performance Polarised-Gamma-Ray Detector"**  
Yannick Geerebaert, D. Bernard, P. Bruel, M. Frodin, B. Giebels, P. Gros, D. Horan, M. Louzir, P. Poilleux, I. Semeniouk, S. Wang, D. Attié, D. Calvet, P. Colas, A. Delbart, P. Sizun, D. Götz AIM, S. Amano, S. Hashimoto, T. Kotaka, Y. Minamiyama, S. Miyamoto, A. Takemoto, M. Yamaguchi, S. Daté, H. Ohkuma  
20th Real Time Conference, Padova, Italy, 5-10 June (2016).
7. **"Laser Compton Scattering Gamma-ray Beam Generation and Applications"**  
Shuji Miyamoto (Invited)  
Carpathian Summer School of Physics 2016, "Exotic Nuclei & Nuclear / Particle Astrophysics (VI). Physics with small accelerators", Sinaia, Romania, June 26-July 9 (2016).
8. **"First measurement of polarization asymmetry of a gamma-ray beam between 1.74 to 74 MeV with the HARPO TPC"**  
Philippe Gros, Sho Amano, David Attié, Denis Bernard, Philippe Bruel, Denis Calvet, Paul Colas, Schin Daté, Alain Delbart, Mickael Frodin, Yannick Geerebaert, Berrie Giebels, Diego Götz, S. Hashimoto, Deirdr Horan, T. Kotaka, Marc Louzir, Y. Minamiyama, Shuji Miyamoto, H. Ohkuma, Patrick Poilleux, Igor Semeniouk, Patrick Sizun, A. Takemoto, M. Yamaguchi, Shaobo Wang

SPIE Astronomical telescopes and instrumentation conference 2016 (2016).  
Instrumentation and Methods for Astrophysics (astro-ph.IM); Instrumentation and Detectors  
(physics.ins-det)

9. **"NewSUBARU Gamma Beam Source - Status and Activities"**  
Shuji Miyamoto (Invited)  
International Conference on Nuclear Photonics, Monterey, California, Oct. 16-21 (2016).
10. **"PDCA Cycle Model of Drawing Process for Class Placement of Liberal Arts – The trial work of the IR section at the University of Hyogo"**  
Y. Shoji and Y. Kokubo  
5th International Conference on Data Science and Institutional Research, Kumamoto Japan, July 10-14 (2016).
11. **"Evaluation of amorphous carbon film by X-ray absorption spectroscopy"**  
Kazuhiro Kanda (Invited)  
26th annual meeting of the Materials Research Society of Japan (MRS-J) Yokohama, Japan Dec. 19-22, (2016).
12. **"Evaluation of amorphous carbon film by X-ray absorption spectroscopy"**  
Shotaro Tanaka, Makoto Okada, Takayuki Hasegawa, Masahito Niibe, and Kazuhiro Kanda  
26th annual meeting of the Materials Research Society of Japan (MRS-J) Yokohama, Japan Dec. 19-22, (2016).
13. **"Effect of the soft X-ray irradiation on the surface of fluorinated DLC films"**  
Hiroki Takamatsu, Makoto Okada, Masahito Niibe, and Kazuhiro Kanda  
26th annual meeting of the Materials Research Society of Japan (MRS-J) Yokohama, Japan Dec. 19-22, (2016).
14. **"Structural analysis of diamond-like carbon and related materials using NEXAFS and ellipsometry"**  
Hidetoshi Saitoh, Satoru Arakawa, Sarayut Tunmee, Kazuhiro Kanda, Pat Photongkam, Nichada Jeeranaikun, Ratchadaporn Supruangnet and Hideki Nakajima  
1st Thailand Synchrotron Conference and Exhibition (TSCE2016) SLRI, Thailand, Feb. 26-28 (2016).
15. **"Construction and Performance of the Compact Soft X-ray Emission Spectrometer at BL-09A in NewBUBARU SR Facility"** (invited)  
Masahito Niibe, Noritaka Takehira, and Tahashi Tokushima  
5th Annual Congress of AnalytiX-2017, 22-24 Mar. 2017, Fukuoka, Japan.
16. **"Structural changes on neutron-irradiated highly oriented pyrolytic graphite under static high pressure and temperature"**  
T. Hisakuni, S. Suzuki, S. Honda, M. Niibe, M. Terasawa, Y. Higo, K. Niwase, H. Izumi, E. Taguchi, T. Iwata  
Symp. on Surf. Sci. & Nanotechnol. (SSSN-Kansai), 24-25 Jan. 2017, Kyoto, Japan.
17. **"Irradiation effect in multi-walled carbon nanotubes by highly charged ions"**

- M. Kato, Y. Fujiwara, S. Honda, M. Terasawa, M. Niibe, M. Sakurai, N. Nishida, T. Tokui, K. Suzuki, K. Betsumiya, K. Niwase, K.-Y. Lee  
 Symp. on Surf. Sci. & Nanotechnol. (SSSN-Kansai), 24-25 Jan. 2017, Kyoto, Japan.
18. **"Electrical damage in n-GaN films treated by CF4 plasma"**  
 Yoshitaka Nakano, Masahito Niibe and Retsuo Kawakami  
 Proceedings of International Symposium of Dry Process 2016, pp.73--74, Sapporo, Nov. 2016.
  19. **"A large take-off angle dependence of C-K emission spectra observed in highly oriented pyrolytic graphite"**  
 Masahito Niibe, Takashi Tokushima, Niritaka Takehira, Yuma Araki  
 39th inter'l Conf. on Vacuum Ultraviolet and X-ray Physics (VUVX2016), P\_103, 3-8 July 2016, Zurich, Switzerland.
  20. **"Soft X-ray Absorption Spectroscopy of Orientation, Oxygen Content, Chemical States of Ion-irradiated Vertically Aligned Multiwalled Carbon Nanotubes"**  
 S. Honda, F. Ideno, Y. Muramatsu, M. Niibe, M. Terasawa, E.M. Gullikson and K.-Y. Lee  
 39th inter'l Conf. on Vacuum Ultraviolet and X-ray Physics (VUVX2016), P\_168, 3-8 July 2016, Zurich, Switzerland.
  21. **"Effect of Ultraviolet Light-Assisted CF4 Plasma Irradiation on AlGaIn Thin Film Surface"**  
 Retsuo Kawakami, Masahito Niibe, Yoshitaka Nakano and Takashi Mukai  
 Proceedings of the 43rd International Symposium on Compound Semiconductors (ISCS2016), pp.MoP-ISCS-096\_1--MoP-ISCS-096\_2, Toyama, Jun. 2016.
  22. **"Electrical Damage Investigation of n-GaN Films Treated by CF4 Plasma"**  
 Yoshitaka Nakano, Masahito Niibe and Retsuo Kawakami  
 Proceedings of the 43rd International Symposium on Compound Semiconductors (ISCS2016), pp.MoP-ISCS-LN-4\_1--MoP-ISCS-LN-4\_2, Toyama, Jun. 2016.
  23. **"Laser Plasma X-ray Source Based on Cryogenic Targets"**  
 S. Amano  
 The 15<sup>th</sup> International Conference on X-Ray Lasers (ICXRL2016), Nara, May 22-27, 2016.
  24. **"Laser Plasma VUV~X-ray Source Using Solid Rare Gas Targets"**  
 S. Amano  
 The 39<sup>th</sup> International Conference on Vacuum Ultraviolet and X-ray Physics (VUVX2016), Zurich, Swiss, July 3-8, 2016.
  25. **"Molecular orientation evaluation of negative-tone and positive-tone photo-cross-linkable liquid crystalline polymer pattern fabricated by nanoimprint-graphoepitaxy"**  
 Makoto Okada, Yusuke Taniguchi, Yuichi Haruyama, Hiroshi Ono, Nobuhiro Kawatsuki, and Shinji Matsui  
 The 60th International Conference on Electron, Ion and Photon Beam Technology and Nanofabrication 2016, Pittsburgh, USA, 2016/6/1.
  26. **"Thin PDMS antisticking layer formed by using PDMS-disilanol for nanoimprinting"**

Makoto Okada and Shinji Matsui  
The 60th International Conference on Electron, Ion and Photon Beam Technology and Nanofabrication  
2016, Pittsburgh, USA, 2016/6/1.

27. **"Evaluation of molecular orientation induced by simplified double nanoimprint-graphoepitaxy"**  
Makoto Okada, Ryosuke Fujii, Yuichi Haruyama, Hiroshi Ono, Nobuhiro Kawatsuki, and Shinji Matsui  
The 42nd International Conference on Micro and Nano Engineering 2016, Vienna, Austria, 2016/9/21
28. **"Depth analysis of molecular orientation induced by nanoimprint-graphoepitaxy"**  
Makoto Okada, Ryosuke Fujii, Yuichi Haruyama, Hiroshi Ono, Nobuhiro Kawatsuki, and Shinji Matsui  
The 42nd International Conference on Micro and Nano Engineering 2016, Vienna, Austria, 2016/9/21.
29. **"Simplified double nanoimprint-graphoepitaxy using L&S and flat pattern molds"**  
Makoto Okada, Ryosuke Fujii, Yuichi Haruyama, Hiroshi Ono, Nobuhiro Kawatsuki, and Shinji Matsui  
The 15th International Conference on Nanoimprint and Nanoprint Technology 2016, Braga, Portugal,  
2016/9/27, invited poster.
30. **"Examination of depth profile of molecular orientation in L&S pattern fabricated by nanoimprint-graphoepitaxy"**  
Makoto Okada, Ryosuke Fujii, Yuichi Haruyama, Hiroshi Ono, Nobuhiro Kawatsuki, and Shinji Matsui  
The 15th International Conference on Nanoimprint and Nanoprint Technology 2016, Braga, Portugal,  
2016/9/27.
31. **"High-aspect-ratio structure fabrication by room-temperature nanoimprinting"**  
Makoto Okada and Shinji Matsui  
The 29th International Microprocesses and Nanotechnology Conference 2016, Kyoto, Japan, 2016/11/11.
32. **"Evaluation of Thermal Nanoimprint Resin with PDMS Additive for Improving Release Property"**  
Shogo Fukui, Makoto Okada, and Yuichi Haruyama  
The 29th International Microprocesses and Nanotechnology Conference 2016, Kyoto, Japan, 2016/11/10.
33. **"Molecular orientation in photoreactive liquid crystalline polymer films observed by NEXAFS"**  
Y. Haruyama, Y. Taniguchi, M. Kondo, N. Kawatsuki, M. Okada, and S. Matsui  
The 39th International conference on Vacuum Ultraviolet and X-ray Physics, Zurich, Switzerland,  
2016/7/5.
34. **"Evaluation of damage in an organic thin film with cluster ion sputtering"**  
S. Fujita, Y. Nohara, M. Ohno, and Y. Haruyama  
The 39th International conference on Vacuum Ultraviolet and X-ray Physics, Zurich, Switzerland,  
2016/7/5.
35. **"Observation Results of Actual Phase Defects Using Micro Coherent EUV Scatterometry Microscope"**  
Hiraku Hashimoto, Tetsuo Harada, Takeo Watanabe  
Photomask Japan 2016, Yokohama, Japan, 2016/4/7.
36. **"Measurement Result of an EUV Collector Mirror Using a Large Reflectometer at NewSUBARU"**

Haruki Iguchi, Tetsuo Harada, Takeo Watanabe  
Photomask Japan 2016, Yokohama, Japan, 2016/4/7.

37. **"Defect Imaging Result with Quantitative Intensity and Phase Contrast Using Micro Coherent EUV Scatterometry Microscope"**  
Tetsuo Harada, Hiraku Hashimoto, Takeo Watanabe, Hiroo Kinoshita  
Photomask Japan 2016, Yokohama, Japan, 2016/4/8.
38. **"EUVL Research Activity at Center for EUV Lithography"**  
Takeo Watanabe, Tetsuo Harada  
ICPST33, Chiba, Japan, 2016/6/24.
39. **"Development of the transmittance measurement for EUV resist by direct-resist coating on a photodiode"**  
Daiki Mamezaki, Masanori Watanabe, Tetsuo Harada and Takeo Watanabe  
ICPST33, Chiba, Japan, 2016/6/24.
40. **"Observation results of actual phase defects using micro-coherent EUV scatterometry microscope"**  
Hiraku Hashimoto, Tetsuo Harada, Hiroo Kinoshita, Takeo Watanabe  
Photomask Technology 2016, San Jose, USA, 2016/9/12.
41. **"Development of actual EUV mask observation method for micro-coherent EUV scatterometry microscope"**  
Tetsuo Harada, Hiraku Hashimoto, Hiroo Kinoshita, Takeo Watanabe  
Photomask Technology 2016, San Jose, USA, 2016/9/12.
42. **"EUV Resist Transmittance Measurement Using Photodiode Direct-Resist Coating Method"**  
Daiki Mamezaki, Masanori Watanabe, Tetsuo Harada, Takeo Watanabe  
EUV Lithography Symposium 2016, Hiroshima, Japan, 2016/10/24.
43. **"Development of Large EUV reflectometer in NewSUBARU Synchrotron Facility"**  
Tetsuo Harada, Haruki Iguchi, Takeo Watanabe  
EUV Lithography Symposium 2016, Hiroshima, Japan, 2016/10/24.
44. **"Actual Defect Imaging Result with Quantitative Intensity and Phase Contrast Using Micro Coherent EUV Scatterometry Microscope"**  
Tetsuo Harada, Hiraku Hashimoto, Takeo Watanabe  
EUV Lithography Symposium 2016, Hiroshima, Japan, 2016/10/24.
45. **"Development of the negative-tone molecular resists for EB/EUVL having high EUV absorption capacity"**  
Tomoaki Takigawa, Yuta Togashi, Takumi Toida, Takashi Sato, Masatoshi Echigo, Hiroto Kudo, Tetsuo Harada, Takeo Watanabe  
EUV Lithography Symposium 2016, Hiroshima, Japan, 2016/10/24.
46. **"Defect and absorber phase imaging of EUV mask using synchrotron and high-harmonic-generation EUV source"**  
Tetsuo Harada, Takeo Watanabe  
OSA International Workshop on Compact EUV & X-ray Light Sources, Hiroshima, Japan, 2016/10/28.
47. **"Improvement of Mask-Defect-Detection Performance of Coherent EUV Scatterometry**

**Microscope with High-Harmonic-Generation EUV Source"**

Daiki Mamezaki, Tetsuo Harada, Yutaka Nagata, Takeo Watanabe  
Micro Nano Conference, Kyoto, Japan, 2016/11/11.

48. **"A study on enhancing EUV resist sensitivity"**  
Atsushi Sekiguchi, Tetsuo Harada, Takeo Watanabe  
SPIE advanced Lithography 2017, San Jose USA, 2017/2/28.
49. **"Rapid X-ray fabrication of microstructured polytetrafluoroethylene substrates by anisotropic, pyrochemical microetching"**  
Akinobu Yamaguchi, Hideki Kido, Yuichi Utsumi  
The 33rd International Conference of Photopolymer Science and Technology, June 22-24 (2016), Makuhari, Chiba, Japan (招待講演)
50. **"Fabrication of higher order three-dimensional layer stack nanostructure for molecular detection and electrode"**  
Akinobu Yamaguchi, Takao Fukuoka, Mari Ishihara, Yuichi Utsumi  
SPIE Optics + Photonics 2016, August 30 - September 1 (2016), San Diego, USA
51. **"Synthesis of nanoparticles through X-ray radiolysis using synchrotron radiation"**  
Akinobu Yamaguchi, Ikuo Okada, Takao Fukuoka, Mari Ishihara, Ikuya Sakurai, Yuichi Utsumi  
SPIE Optics + Photonics 2016, August 30 - September 1 (2016), San Diego, USA
52. **"Development of Miniature Micro-Powder Feeder Driven by Surface Acoustic Wave for Practical Use"**  
Tsunemasa Saiki, Akio Tsubosaka, Akinobu Yamaguchi, Masahiro Takeo, Michitaka Suzuki, Yuichi Utsumi  
The 42nd International Conference on Micro and Nano Engineering (MNE2016), September 19-23 (2016), Vienna, Austria
53. **"Alternative Raman Spectroscopy of Glycine Binding on Au-Nanoparticle-Decorated Polystyrene Beads due to Aggregation induced by Dielectrophoresis in Micro-Optofluidic devices"**  
Akinobu Yamaguchi, Takao Fukuoka, Yuichi Utsumi  
The 20th international conference on miniaturized systems for chemistry and life science (TAS2016), October 10-15 (2016), Dublin, Ireland
54. **"Anisotropic Pyrochemical Fabrication of Polytetrafluoroethylene and Metallic Nanoparticles Initiated by Synchrotron Radiation For Microfluidic Devices"**  
Akinobu Yamaguchi, Hideki Kido, Yoshiaki Ukita, Mitsuyoshi Kishihara, Takao Fukuoka, Yuichi Utsumi  
The 20th international conference on miniaturized systems for chemistry and life science (TAS2016), October 10-15 (2016), Dublin, Ireland
55. **"Observation of magnetic domain structure initiated by competition among the magnetoelastic anisotropy and shape anisotropy using XMCD-PEEM"**  
A. Yamaguchi, T. Ohkochi, A. Yasui, T. Kinoshita, and K. Yamada  
61st Annual Conference on Magnetism and Magnetic Materials, October 31- November 4 (2016), New

Orleans, LA, USA

56. **"Measurement of Critical Cracking Strain of Organic Thin Films Prepared by Wet Coating Process"**

T. Kobayashi, M. Munkhtsog, Y. Utsumi, H. Kanematsu, and T. Masuda

14th European Vacuum Conference (EVC-14), June 6-10 (2016), Portorose, Slovenia

57. **"Small immunoassay systems for medical diagnosis and environmental analysis"**

T. Kobayashi, Y. Yoshimasa, Y. Utsumi

The Irigo Conference 2016, November 1-2 (2016), Tokyo, Japan

### (3) Academic degrees

#### 1. Master of Engineering

Yuma Araki (University of Hyogo)

酸素プラズマ照射による TiO<sub>2</sub> 薄膜の光触媒活性の改善

"Improvement of Photocatalytic Activity of TiO<sub>2</sub> Thin Films by Oxygen Plasma Irradiation"

Noritaka Takehira (University of Hyogo)

ニューズバル軟X線発光分光器を用いたグラファイト材料の分析

"Analysis of Graphite Materials using Soft X-ray Emission Spectrometer in NewSUBARU"

Hiroki Takamatsu (University of Hyogo)

フッ素化DLC薄膜の軟X線照射による改質過程の解明と膜特性変化

"Modification Process and Variation of Film properties of Fluorinated DLC thin films by irradiation of soft X-rays"

Shotaro Tanaka (University of Hyogo)

DLC膜の特性の解明と宇宙利用の検討

"Investigation on Properties of DLC Films and Application into Astronautics field"

Haruki Iguchi (University of Hyogo)

EUV光源集光ミラー用大型反射率計の開発

"Development of a large EUV reflectometer for an EUV collector mirror"

Hiraku Hashimoto (University of Hyogo)

集光型EUV回折顕微鏡による実欠陥観察法の開発

"Actual defect observation using an EUV focused diffraction microscope"

Yuki Fukuda (University of Hyogo)

EUV干渉露光用回折格子の開発および露光装置の高度化

"Development of EUV interference lithography system and its diffraction grating"

Masaya Takeuchi (University of Hyogo)

汎用ディープX線リソグラフィービームライン(BL11)を用いた各種微細加工の検討

"Investigation of microfabrications using deep X-ray lithography system beamline (BL11) for general-purpose"

#### 2. Master of Science

Akinori Takemoto (University of Hyogo)

直線偏光ガンマ線による光核反応に関する研究

"Studies of Photo Nuclear Reaction by Linearly Polarized Gamma-ray Beam"

Masashi Yamaguchi (University of Hyogo)

円偏光ガンマ線による磁気コンプトン散乱に関する研究

"Studies of Magnetic Compton Scattering by Circular Polarized Gamma-ray Beam"

# **LASTI Annual Report Vol.18 (2016)**

---

September 2017, Published by  
Laboratory of Advanced Science and Technology for Industry  
University of Hyogo  
3-1-2 Kouto, Kamigori-Cho, Ako-gun, Hyogo 678-1205, JAPAN  
Phone: +81-791-58-0249 / FAX: +81-791-58-0242

## **Editorial board**

Kazuhiro KANDA (Editor in Chief)

NIIBE Masahito

SHOJI Yoshihiko

HARUYAMA Yuichi

YAMAGUCHI Akinobu

HARADA Tetsuo

---

